Theoretical Modeling the pH-Sensitive Spontaneous Decay of Surface-Functionalized Carbon Dots in Solution

Faculty of Physics and Technology

Department of Nanophysics

University of Bergen, Norway

Denise Dilshener

A thesis submitted for the degree of

Master of Science

supervised by

Dr. Johannes Fiedler, Dr. Drew F. Parsons, Dr. Bodil Holst

Bergen, 02.05.2024

Theoretical Modeling the pH-Sensitive Spontaneous Decay of Surface-Functionalized Carbon Dots in Solution

Denise Dilshener

Abstract

Since many biological and chemical processes strongly depend on pH, its precise detection is essential for a wide range of applications. Due to their distinct luminescence characteristics, carbon quantum dots, or CDs, have become attractive options for pH detection. In this thesis, fluorescence lifetime measurements of surface-functionalized CDs are investigated concerning their capability for pH monitoring. A detailed analysis is conducted of the theoretical understanding of the excitation lifetimes of these functional groups in response to variations of the surrounding medium's pH. The effects of protonation and deprotonation of the functional groups is the focus of these investigations. The pH-dependence of excitation lifetimes of functional groups, such as m-phenylenediamine, phloroglucinol, and disperse blue 1 attached to CDs, is modeled by utilising concepts from time-dependent density functional theory (TD-DFT) and macroscopic Quantum Electrodynamics. A mathematical relation between pH, pKa, and excitation lifetimes has been derived and applied to organic dye molecules functionalising a carbon dot. The obtained results manifest the intuition that the pKa determines the sensitive pH range and the pH sensitivity is proportional to the ratio of the fluorescence lifetimes of the protonated and deprotonated states. This model sheds light on the fundamental processes underpinning CDs' pH-dependent fluorescence and offers important insights into how they behave in different pH ranges. The theoretical framework developed within this thesis provides a comprehensive method for estimating and comprehending optical behaviour of pH sensitive materials.

Contents

Chapter 1

Introduction

In many scientific and industrial domains, pH is a crucial component. pH is a numeric scale used to specify the acidity or basicity of an aqueous solution, with values below seven indicating acidity, above seven indicating alkalinity, and seven representing neutral. Even a small pH variation can strongly affect the system's properties and dynamics. For example in aquaculture, more especially in fish farming, water quality monitoring becomes essential. It's important to make sure live fish aren't exposed to potentially hazardous environmental conditions like oil spills or algal blooms when moving them around in wellboats [1]. To prevent the wellboat from pumping polluted or inferior water, close monitoring of the water's conditions is necessary [2].

In addition, ocean acidification, lowering pH levels, modifies the carbonate chemistry of marine habitats dramatically [3]. The marine microbiome, which is essential to ocean ecosystems, is greatly affected by this process. To comprehend and counteract these changes, it is crucial to use cutting-edge technologies to investigate how pH variations affect the microbiome.

The necessity for sophisticated pH sensor technologies is highlighted by the understanding and measurement of pH in a variety of applications [4]. Conventional pH electrodes have disadvantages: (i) since their properties alter over time, they must be calibrated often. (ii) Additionally, they must have their electrolyte levels regularly replenished to offset consumption. (iii) Furthermore, these electrodes frequently exhibit subpar performance in highly salinized conditions, which can be a major disadvantage in fields like marine research or those that work with brackish or saltwater. As a result, there is a need for improved and trustworthy pH measurement solutions that
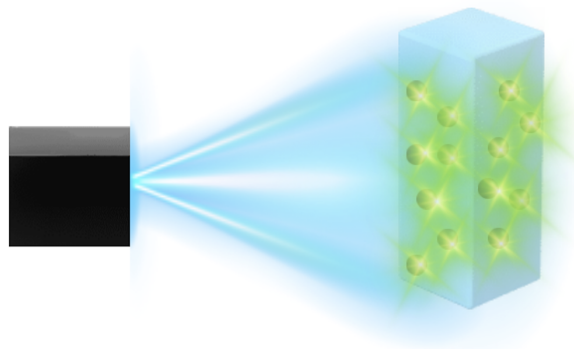
Figure 1.1: The overall system in the above image shows a laserbeam as incoming light (blue) hitting carbon dots in a solution. The carbon dots are emitting now light (here: green) of a lower wavelength

can get beyond these obstacles [4, 5].

To overcome these drawbacks, novel pH metrology techniques such as optodes, spectrophotometric systems and ion-sensitive field-effect transistors (ISFETs) have been developed [6]. However, these technologies also have disadvantages such as increased expenses and power requirements, sensitivity to light and pressure, and the requirement for specialised materials to guarantee long-term stability. Furthermore, one outstanding problem with these advanced methods is the precise regulation of temperature and ionic strength during seawater analysis, which has a substantial impact on sensor performance [6], as it uses fluorescence intensity as measuring property.

Due to their high long-term stability, low cost, and low power consumption, optical chemical sensors have drawn more attention. The optical properties of the pH-sensing material are affected by changes in the pH of the surrounding liquid due to the interaction between the hydrogen ions (H+) concentration in the solution and the material itself, which, for instance, can be detected by fluorescence spectroscopy. Challenges, that need to be solved for such sensors are fluctuations of the probe light intensity, background luminescence noise, leaching of the indicator from the immobilising liquid, and photobleaching from sunshine or probe light [7]. To compensate for fluctuations and noises of the probe light, a new measuring method has gained attention that measures the a material's fluorescence lifetime instead of intensity. Fluorescence lifetime refers to processes in which a molecule's electron is excited to a higher energy state by an external source of incoming light. Upon returning to the molecule's ground state via internal processes, the excess energy is released in the form of a photon, resulting in the emission of fluorescing light, as illustrated in Figure 1.1. Here

we can see incoming blue light from a laser to a sample with carbon dots dissolved in a solution, that are emitting green fluorescent light. The time duration to reach the ground state is known as fluorescence lifetime [8]. This characteristic is inherent in the material and is not impacted by the problems with fluorescence intensity measurements, which makes it a strong basis for sensors that have calibration stability over an extended period of time [9].

Experimental studies have demonstrated that the dye molecule acridine exhibits a notable shift in fluorescence lifetime in response to pH variations [7]. The change in nanoseconds per pH unit is 2.0ns/pH. Such findings underscore the potential of leveraging fluorescence lifetime for pH sensing [7]. However, the application of this technique in marine environments is limited due to the inhibitory effect of chloride ions on the fluorescence of acridine, highlighting the need for alternative materials or approaches in such settings. Therefore a new type of material as gained significant interest as a potentially more suitable material: Carbon dots (CDs), are small sized, "spherical" particles that consist of an organic precursor attached to a carbon structure surface. These small, sometimes luminous materials are affordable and easily available, making them ideal for use in various fields such as biomedical [10], catalytic [11] and electronic applications [12]. Their biocompatibility and low toxicity further enhance their appeal. For some types of CDs a quick and sensitive fluorescence response could be observed. In addition, CDs can be easily dispersed in water. These features make CDs an attractive option for the creation of cutting-edge optical sensors. Especially, their sensitivity to environmental changes like pH, which seems to affect their optical characteristics and fluorescence behavior and might be attributed to their small size and large functionalized surface area [13] make them interesting for further investigation. Surface functionalization [14] or quantum confinement processes [14] are thought to cause the fluorescence of carbon dots (CDs). In general, surface functionalisation is the process of adding certain chemical groups to the surface of CDs in order to modify their light emission and increase fluorescence through chemical interactions. Quantum confinement effects occur due to the small size of the CDs, which limits the electron mobility, changes their energy levels and consequently the emitted wavelength.

This thesis is part of a project between the SFI Smart Ocean center for research-

based innovation and the University of Bergen. SFI Smart Ocean is a centre for research-based innovation, working to develop underwater wireless communication along the coast of Norway, combining science and industry, hosted by the Department of Physics and Technology at the University of Bergen. One of the projects of SFI Smart Ocean is to provide a fluorescence lifetime sensitive pH sensor. W. Szapoczka, a PhD student at SFI Smart Ocean, is working on developing a compact, stable, and affordable optical pH sensor for use in seawater by synthesizing an indicator with pH-dependent fluorescence properties and optimizing its response with different spectral filtering and membrane choices. Building on her observations, my work introduces a theoretical framework aimed at elucidating the pH-dependent fluorescence lifetime of various dye molecules that functionalize the surface of carbon dots before the synthesis. A theoretical model has been developed to investigate the fluorescence lifetime behaviour of the surface functional groups attached to a carbon dot and surrounded by a liquid. To achieve this, quantumchemical calculations have been combined with macroscopic Quantum Electrodynamics (mQED) to investigate the decay dynamics of the molecules upon pH variation. This approach has been applied to the same dye molecules as investigated in the work of W. Szapoczka *et al.*, namely m-phenylenediamine (mPD), phloroglucinol, and the disperse-blue1 dye [4, 15].

1.1 Existing Work

To develop a theoretical model for computing the fluorescence lifetime of molecules, a thorough evaluation of previous studies has been carried out. The methodology in this work is influenced by three key studies on molecular excited state and fluorescence lifetime calculations. The chosen methodologies for the model in this work can be justified by the workflow of the three studies. In this work, we not only investigate the excitation lifetime but also develope a theory to investigate the pH dependency of carbon dots dissolved in solution as a whole.

Z.C. Wong *et al.*[16] investigated the photophysical properties, including fluorescence lifetimes, of syn-bimane fluorophores using time-dependent density functional theory (TD-DFT) with a set of six different hybrid-exchange correlation functionals, including B3LYP and PBE0. They started by optimising the geometry of the ground

state with density functional theory (DFT). Next, electronic transition energies in various solvent conditions with TD-DFT where obtained. Vibrationally resolved absorption and emission peaks where then calculated to obtain the mean value of the inverse cube of the fluorescence wave number. The fluorescence lifetime is then obtained via the radiative transition rates by calculating the Einstein-coefficient of the electronic transition at the excited state equilibrium geometry.

J. Preiss *et al.* [17] predicted fluorescence lifetimes of different molecules incorporating solvent effects. They developed a theoretical model that combines the nuclear-ensemble approach within the conductor-like screening model (COSMO), taking into account vibrational and solvent effects. The fluorescence spectra have been calculated form the geometries obtained by the nuclear ensemble method using TD-DFT and then broadened to include vibrational effects. The radiative component of the fluorescence lifetime was calculated using the emission spectra by integrating over the spectrum to determine the average lifetime of the excited state before it returns to the ground state. The Strickler-Berg equation was used as a framework to relate the emission and absorption properties of the fluorescence lifetime. The radiative lifetime calculations where combined with experimentally measured fluorescence quantum yields to estimate the total fluorescence lifetimes.

Using Quantumchemical calculations, R.C.E. Sia *et al.* [18] investigated the fluorescence /radiative emission lifetime of BODIPY dyes. The ground state was computed with DFT and with TD-DFT the excited states where obtained. Solvent effects where incorporated using the Polarizable Continuum Model (PCM). The radiative lifetime was obtained using Einsteins' A-coefficient derived from the transition energies and the electronic transition dipole moments obtained with TD-DFT and the radiative lifetime is the inverse of the coefficient, considering both the direct transition and the effects of vibronic coupling, which modify the transition energies and probabilities due to molecular vibrations. The vibronic effects where accounted for using the Franck-Condon and Herzberg-Teller approaches to simulate the absorption and emission spectra and then calculate their impact on the radiative rates.

The suggested workflow of our model is organised as follows, taking inspiration from these studies: After molecular geometry optimisation using DFT calculations, transition energies and dipole moments will be evaluated using TD-DFT. The radiative

lifetime is then obtained via the inverse of Einsteins' A-coefficient, as can be seen in Section 2.2. To include solvent effects as well as the effect of the carbon dot on the surface functional group, the Einstein coefficient was extended / corrected by including scattering effects of the solvent and the carbon dot, see Section 2.5 and 2.7.3. The pH sensitivity of the carbon dot as a whole has been derived via Henderson-Hasselbalchs equilibrium equation of protonated and deprotonated forms of the molecules in Section 2.7.2.

1.2   The Overall Project
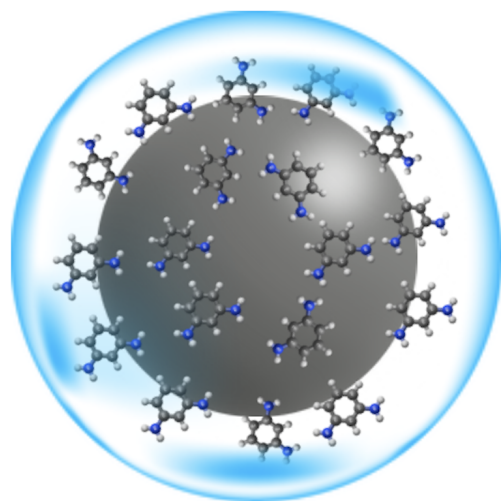
Figure 1.2: A Two-Layer Carbon Dot System: This illustration features a carbon dot, where the grey sphere symbolizes the carbon core, with m-phenylenediamine dye molecules attached to its surface. The carbon dot is encapsulated within a liquid environment, isolating the surface molecules in a simulated vacuum.

Creating a theoretical model that can predict the pH-sensitive fluorescence lifetime of carbon dots in solution is the main goal of this thesis. One of the most important parameters in photoluminescence is the fluorescence lifetime, which is the average amount of time a molecule spends in its excited state before emitting a photon to return to the ground state, see Section 2.1. Understanding it and projecting its lifetime are crucial for applications in materials research, sensing, and imaging [4].

To achieve this, the focus is set on a specific system: carbon dots with surface-functionalized dye molecular groups. These carbon dots can be visualized as being encapsulated within a "bubble" of solution [19] creating a thin vacuum layer between the surface functional groups and the solution membrane, as can be seen in Figure 1.2.

The complete experimental setup, represented in Figure 1.1, can be understood as follows: The incoming laser light excites the dye-centre of the functional groups, causing the dye molecules to enter a higher state and emit a photon as they relax back into the ground state. This photon emission is observed as fluorescence, emitting light of a lower wavelength than the absorbed light. The surrounding solution's pH affects the structure of the dye molecules, leading to a change internal relaxation dynamics, see Section 2.2. This effect is directly observable through the fluorescence lifetime.

For this model, we use Density Functional Theory (DFT) and Time-Dependent DFT (TDDFT) as tool to predict the transition energies between excited states of a molecule in vacuum. These computational techniques are the main instruments for simulating the behaviour of the dye molecules in the absence of surrounding medium.
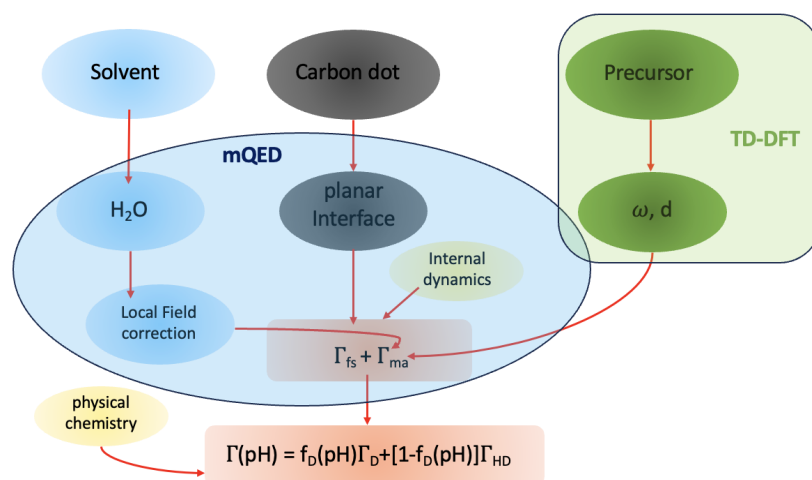
Figure 1.3: A schematic representation of the overall workflow to develop the theoretical model for simulating pH sensitive fluorescence lifetime of dye molecules. We have three variables to consider: the Carbon dot itself, its precursor and the surrounding solvent. The solvent as well as the carbon dot can be modeled using tools from macroscopic Quantum Electrodynamic (mQED), whereas the properties of the precursor molecules are investigated by quantumchemical calculations with time dependent density functional theory (TD-DFT). The final result is obtained by including pH dependence via physical chemistry.

Figure 1.3 presents an overview of the modelling procedure. Three different variables have to be modeled in order to derive a pH sensitive fluorescence description of carbon dots in a solution, starting by applying methods from macroscopic Quantum Electrodynamics (mQED) to the solvent (blue) as well as the carbon dot (grey). The precursor (green) is modeled using time dependent density functional theory (TD-

DFT) and in the end all three variables are combined together to the final equation (orange), after including pH-dependent properties from physical chemistry. By coupling the molecular system to the quantised electromagnetic fields, the relaxation dynamics can be derived, leading the Einstein coefficient, Γ_{fs}, by considering the quantum vacuum. Whereas, in the presence of absorbing materials, the local optical mode density enters this equation describing the excitation dynamics of the molecule when it is coupled to the environment. This method allows us to separate the functional group from the remaining carbon dot and the solvent, leading the medium-assisted transition rates, Γ_{ma}, as a correction to the Einstein coefficient. In addition, the emitted light has to propagate through the solvent. To take its transmission at the interface between the solvent and the carbon dot into account, we use the well-established local-field corrections. The precursors free-space transition rate is obtained with DFT and TD-DFT by calculating the transition frequencies ω_{nm} and the transition dipole moments $\mathbf{d}_{nm}$ of the molecules in different protonation states in free-space. Finally, in Section 2.7.2, the pH sensitivity is included via principals form physical chemistry, the Henderson-Hasselbalchs relationship between pH and a molecules protonation state

Chapter 2

Theoretical Foundations

The theoretical knowledge needed to navigate the computational approaches described in Chapter 3 is laid out in this chapter. We start with a simple description and calculation of the fluorescence lifetime in Section 2.1. Afterwards, the internal dynamics of an atom are derived in Section 2.2 to obtain an expression for transition rate in free-space, Γ_{fs}. In this context, "internal dynamics" refers to the complex motions and interactions of electrons inside an atom that have a major impact on the energy states of the atom and, as a result, its fluorescence. This chapter not only covers the system's vacuum environment but also includes scattering effects in presence of a medium, which are essentially the interactions and changes caused by the surrounding solution surrounding the carbon dot. These effects are calculated independently using the approximations described in Section 2.5, where a local-field correction is introduced. Additionally, a number of variables that affect the system are examined, such as the pH of the surrounding solution and the inherent characteristics of the Carbon Dot in Section 2.7.3. After that, we explore the theoretical foundations covered in Sections 2.8.1, Section 2.8.2, and Section 2.9 that are essential to comprehending the computational modelling process. This comprehensive method provides a deep understanding of the conceptual and practical elements necessary for the modeling process.

2.1 Fluorescence

We examine the theoretical foundations required to broaden our comprehension of the fluorescence process in this chapter. Under UV light, fluorescence—a process in which

objects absorb light at one wavelength and emit it at another—often takes the form of bright, glowing colours. This phenomenon is caused by absorbed photons exciting the substance's electrons, which then release energy as visible light when they return to their ground state. The goal of this thesis is to simulate the fluorescence lifetime of carbon dots with different surface molecules, and understanding this mechanism is essential to achieving that goal. The development of a novel pH sensor, which holds promise for the improvement of sensing technology, could be improved with my model.

2.1.1 Luminescence

When light energizes the electrons of an atom or molecule, they emit a radiant glow as they return to their lower energy states. This emission of light is known as the luminescence effect. The luminescence process can be divided into two subcategories: fluorescence and phosphorescence, depending on the origin of the involved electron spin states.

Fluorescence is observed when an electron in an atom transition from an excited singlet state, where it is energetically unstable, back to its ground state, which is energetically more favorable. This process involves the emission of a photon, as the electron releases the excess energy accumulated during its excitation [20]. The phosphorescence mechanism can be observed when light gets emitted
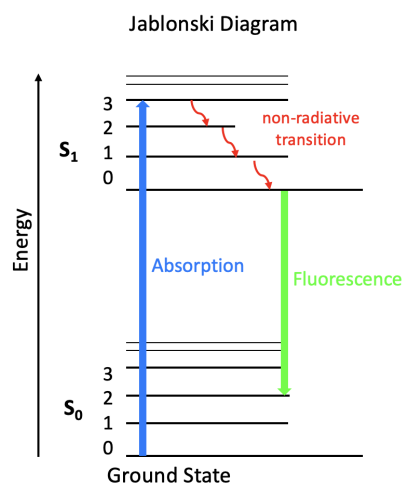
Figure 2.1: A Jablonski diagram representing the non radiative vs the fluorescence decay.

from a triplet excited state of electrons with same spin orientation. As the spin has the same orientation, transitions into the ground state are forbidden, following the Pauli exclusion principle. Transitions back to the ground state are not likely [20]. The whole process can be shown in a so called Jablonski diagram, see for instance figure

2.1. The Jablonski diagram is a graphical representation used in spectroscopy to illustrate the electronic energy levels of molecules and the transitions between them. It shows a molecule's absorption and excitation to higher electronic states and subsequently emit energy as they return to lower states. This aids in visualizing phenomena such as fluorescence and phosphorescence.

2.1.2 Fluorescence

The fluorescence process follows the permissive principles of quantum mechanics, making it considerably more probable than phosphorescence. This transition unfolds swiftly as an electron emits a photon, occurring at a rate typically around 10^8 emissions per second and with a fluorescence lifetime of approximately 10 nanoseconds ($\times 10^{-8}$ seconds)[20].

The photon emits during the emission phase, but its energy is lower than that of the light that was absorbed. The Stokes shift, which is caused by this process, enables the light to shift towards a longer wavelength and is frequently apparent as a unique colour during emission. Because of internal conversion mechanisms that release some energy as heat prior to the photon's emission, the energy difference between an electron's excited state and ground state is smaller than the energy of the absorbed photon. This results in the Stokes shift, [20], as indicated in figure 2.2.

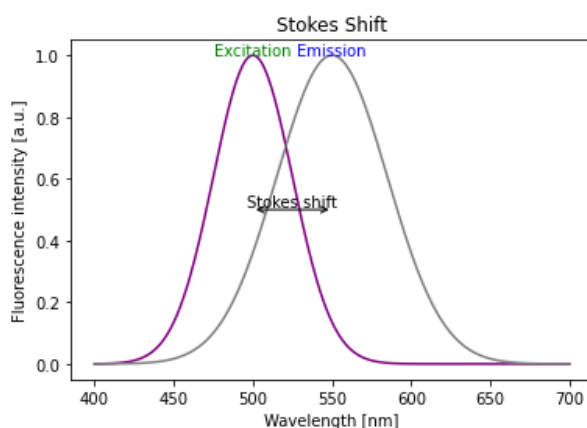**Figure 2.2:** An emission/ absorption spectra including the Stokes shift during a fluorescence process.

A fluorescence emission spectrum, as shown in 2.2, represents a plot of the fluorescence intensity vs. the wavelength. The fluorescence intensity, reflecting the number

of emitted photons and their energy, contributes to the overall brightness and vividness of the observed fluorescence. This characteristic is crucial in sensitivity detection, as it serves as a quantitative measure of the amount of fluorophore (fluorescent compounds that emit light upon excitation during the fluorescence process) present in a sample [20, 4].

Fluorescence Lifetime and Quantum Yields

The most important characteristics of fluorophores, which are fluorescent compounds that emit light upon excitation during the fluorescence process, are their quantum yield and fluorescence lifetime. The quantum yield quantifies the efficiency of the fluorescence process by describing the ratio of emitted photons to the number absorbed. In essence, it serves as a measure of how effectively a fluorophore converts absorbed energy into emitted light. A higher quantum yield corresponds to a brighter emission, making it a crucial parameter for assessing the efficiency of fluorescence in practical applications [20]. This characterisic can be used in solar-cell applications.

Additionally, the fluorescence lifetime of a fluorophore is a key parameter that determines the average duration a molecule remains in its excited state before returning to the ground state [20]. This timespan is a fundamental aspect of the fluorescence process and contributes to the overall temporal characteristics of fluorescence signals. Understanding the fluorescence lifetime is essential for applications, where precise timing and temporal resolution are critical, such as in fluorescence microscopy and time-resolved spectroscopy. Together, the quantum yield and fluorescence lifetime provide comprehensive insights into the performance and behavior of fluorophores, making them essential considerations in the design and optimization of fluorescence-based assays and imaging techniques [4].

2.2   Internal dynamics of an atom

We start deriving the general expression for the transition rate in free-space, Γ_{fs}. An insight of an atom's internal dynamics is necessary in order to properly understand the fluorescence process in greater detail. These dynamics, which include the electronic and vibrational motions of the atom, are essential for comprehending and predicting

a wide range of physical and chemical properties. These properties include the characteristics of materials, nuclear dynamics, energy transfer processes, and the understandings gained from molecular dynamics simulations. This thorough comprehension provides insight on the complex behaviours of atoms and molecules, especially with regard to their interactions with light and energy, which is essential to the study of fluorescence.

As the goal of the thesis is to simulate and predict the fluorescence lifetime of Carbon Dots, it is crucial to evaluate the internal dynamics of atoms in their ground as well as in their excited state. Casimir-Polder forces, which arise from quantum fluctuations of the electromagnetic field in the vacuum, interact with excited states of atoms, [21]. These interactions change an atom's energy levels, which in turn affects how it acts in proximity to surfaces or other particles, even at a distance. An atom primarily experiences a non-resonant ground state potential after releasing a photon and going back to its ground state. Solving the coupled dynamics between the atom and the electromagnetic field is necessary for the analysis of these occurrences. This is accomplished by figuring out how the dipole and field operators behave over time inside the Heisenberg image, which shows how the atom is affected by Casimir-Polder interactions. This method shows the complex relationship of quantum mechanical forces and highlights the important significance of Casimir-Polder interactions, especially when affecting the properties of atoms and molecules at surfaces or in nanostructured materials. The internal state dynamics of a particle in the presence of dielectric bodies must be collected in order to determine the influence of the surrounding carbon and aqueous medium on the transition rate. The system [22] is thus divided into three components: the molecule-field coupling $\hat{H}_{\mathrm{MF}}$, the electromagnetic fields $\hat{H}_{\mathrm{F}}$, and the molecular system $\hat{H}_{\mathrm{M}}$.

$$\hat{H} = \hat{H}_{\mathrm{M}} + \hat{H}_{\mathrm{F}} + \hat{H}_{\mathrm{MF}}. \tag{2.1}$$

This equation shows the model's limit of validity, which is that it can only be applied to separable systems—in our case, that is, systems in which the dye centre, which is in charge of pH sensitivity, is isolated from the host material. One way to quantify this separability is to find the overlap between the corresponding wave functions.

The internal dynamics can be described by the time-dependent atomic density matrix in the Schrödinger picture, expanded by the completeness relation in terms of

internal-energy eigenstates

$$\hat{\sigma} = \sum_{m,n} \sigma_{mn} |m\rangle \langle n|. \tag{2.2}$$

The time-dependent density matrix elements,

$$\sigma_{mn}(t) = \sigma_{mn} = \langle m| \hat{\sigma} |n\rangle, \tag{2.3}$$

represent the probabilities of an atom being in the representative initial state $|n\rangle$, the other matrix elements characterise the coherence of the internal atomic quantum state. $|n\rangle$ is indicating a higher state. To study the internal dynamics within the Heisenberg frame, the time-dependent atomic flip operator is introduced

$$|m\rangle \langle n| = \hat{A}_{mn} = \hat{A}_{mn}(t), \tag{2.4}$$

describing the transition from n to m, Thus, its expectation value reads

$$\langle \hat{A}_{mn}(t) \rangle = tr[\hat{\sigma} \hat{A}_{mn}] = \sum_{k,l} \hat{\sigma}_{kl}(t) \langle l| \hat{A}_{mn} |k\rangle = \sigma_{nm}(t), \tag{2.5}$$

where we used the orthogonality $\langle l| \hat{A}_{mn} |k\rangle = A_{lk}\delta_{lm}\delta_{nk}$, leading to the commutation relation

$$[\hat{A}_{mn}, \hat{A}_{kl}] = |m\rangle \langle n| |k\rangle \langle l| - |k\rangle \langle l| |m\rangle \langle n| = \delta_{nk}\hat{A}_{ml} - \delta_{lm}\hat{A}_{kn}. \tag{2.6}$$

With the flip operator [2.4], the molecular Hamiltonian can be written in eigenbases

$$\hat{H}_M = \sum_n E_n \hat{A}_{nn}. \tag{2.7}$$

Consequently, the molecule-field coupling in dipole approximation reads

$$\hat{H}_{MF} = -\hat{\mathbf{d}} \cdot \hat{\mathbf{E}}(\mathbf{r}_A) = \sum_{m,n} \hat{A}_{mn}\mathbf{d}_{mn} \cdot \hat{\mathbf{E}}(\mathbf{r}_A), \tag{2.8}$$

with the electric field

$$\hat{\mathbf{E}}(\mathbf{r}) = \int_0^\infty \hat{\mathbf{E}}(\mathbf{r},\omega)\, d\omega + \text{H.c.} = \int_0^\infty d\omega \sum_{\lambda=e,m} \int d^3r' \mathbf{G}_\lambda(\mathbf{r},\mathbf{r}',\omega)\hat{f}_\lambda(\mathbf{r}',\omega) + \text{H.c..} \tag{2.9}$$

Using the fundamental solution to Helmholtz equation, [21],

$$\left[\nabla \times \nabla \times -\frac{\omega^2}{c^2}\varepsilon(\mathbf{r},\omega)\right] \mathbf{G}(\mathbf{r},\mathbf{r}',\omega) = i\mu_0\omega\delta(\mathbf{r}-\mathbf{r}'), \tag{2.10}$$

it is possible to separate the Green's function into an electric and magnetic part, $\mathbf{G}_e$ and $\mathbf{G}_m$

$$\mathbf{G}_e(\mathbf{r}, \mathbf{r}', \omega) = i\frac{\omega^2}{c^2}\sqrt{\frac{\hbar}{\pi\varepsilon_0}\operatorname{Im}\varepsilon(\mathbf{r}', \omega)}\mathbf{G}(\mathbf{r}, \mathbf{r}', \omega) \tag{2.11}$$

$$\mathbf{G}_m(\mathbf{r}, \mathbf{r}', \omega) = i\frac{\omega}{c}\sqrt{\frac{\hbar}{\pi\mu_0}\frac{\operatorname{Im}\mu(\mathbf{r}', \omega)}{|\mu(\mathbf{r}', \omega)|^2}}[\nabla \times \mathbf{G}(\mathbf{r}, \mathbf{r}', \omega)]^T. \tag{2.12}$$

A complete derivation is shown in Section 2.5. The electromagnetic field is described by the field Hamiltonian [23]

$$\hat{H}_{\mathrm{F}} = \sum_{\lambda=\mathrm{e,m}} \int \mathrm{d}^3r \int_0^\infty \mathrm{d}\omega\, \hat{f}_\lambda^\dagger(\mathbf{r}, \omega) \cdot \hat{f}_\lambda(\mathbf{r}, \omega), \tag{2.13}$$

with the field's ladder operators $\hat{f}_\lambda$ and $\hat{f}_\lambda^\dagger$. These operators help generating the Heisenberg equation for fundamental fields, using the commutation relations

$$\begin{aligned}\dot{\hat{f}}_\lambda(\mathbf{r}, \omega) &= \frac{1}{i\hbar}[\hat{f}_\lambda(\mathbf{r}, \omega), \hat{H}_F] + [\hat{f}_\lambda(\mathbf{r}, \omega), \hat{H}_{AF}] \\ &= -i\omega\hat{f}_\lambda(\mathbf{r}, \omega) + \frac{i}{\hbar}\sum_{m,n}\mathbf{G}_\lambda(\mathbf{r}_A, \mathbf{r}, \omega)^T \mathbf{d}_{mn}\hat{A}_{mn},\end{aligned} \tag{2.14}$$

where the solution of the inhomogenous differential equation is

$$\begin{aligned}\hat{f}_\lambda(\mathbf{r}, \omega, t) &= \exp[-i\omega(t-t')]\hat{f}_\lambda(\mathbf{r}, \omega) \\ &\quad + \frac{i}{\hbar}\sum_{m,n}\int_0^t dt'\exp[-i\omega(t-t')]\mathbf{G}_\lambda^{T*}[\mathbf{r}_A(t'), \mathbf{r}, \omega]\mathbf{d}_{mn}\hat{A}_{mn}(t').\end{aligned} \tag{2.15}$$

The time dependent electric field operator can be derived by inserting Equation (2.15) in the expression (2.9)

$$\begin{aligned}\hat{\mathbf{E}}(\mathbf{r}, \omega, t) &= \exp\left(-i\omega(t-t_0)\right)\hat{\mathbf{E}}(\mathbf{r}) \\ &\quad + \frac{i\mu}{\pi}\sum_{m,n}\omega^2\int_0^t dt'\exp\left(-i\omega(t-t')\right) \\ &\quad \times \operatorname{Im}\mathbf{G}[\mathbf{r}_A(t'), \mathbf{r}, \omega]\mathbf{d}_{mn}\hat{A}_{mn}(t').\end{aligned} \tag{2.16}$$

The first term describes the free field in absence of an atom, the second term is the source term created by an atom. We have successfully expanded the formula for the electric field to include both cases: with and without time-dependent atom coupling. It is important to mention that the source field depends on the position and state of the atom at all times. An explicit evaluation requires the neglection of the CP forces,

therefore the relation $r_A(t) = r_A(t') \equiv r_A$ is used to neglect atomic motions.

We continue evaluating the expression for the source field term of the electric field expression by assuming weak field coupling and using the Markhov approximation. This means that a system does not have a memory and all effects from previous influences on the field are neglected.

The spectral distribution of the source field, represented by $\omega^2 Im \mathbf{G}(r_A, r_A, \omega)$, is expected not to exhibit sharp peaks around the atom's transition frequency, under the premise that there is a weak coupling between the atom and the field. Therefore, it can be assumed that the oscillations with a certain frequency $\widetilde{\omega}_{mn} \neq \omega_{mn}$ are dominating the dynamics. To evaluate the frequencies $\widetilde{\omega}_{mn}$, we neglect the slow non-oscillatory dynamics during a certain time interval $t_0 \leq t' \leq t$, yielding

$$\int_0^t dt' \exp\left(-i\omega(t - t')\right) \hat{A}_{mn}(t') \simeq \hat{A}_{mn}(t) \int_0^t dt' \exp\left(-i(\omega - \widetilde{\omega}_{mn})\right)(t - t'). \quad (2.17)$$

A precise calculation of this integral, as detailed in Ref. [21], results in a reformulated expression for the electric field

$$\hat{\mathbf{E}}(r, \omega, t) = \exp\left(-i\omega(t - t_0)\right) \hat{\mathbf{E}}(r, \omega)$$
$$+ i\mu_0 \sum_{m,n} \left[\delta(\omega - \widetilde{\omega}_{nm}) - \frac{i}{\pi} \frac{P}{\omega - \widetilde{\omega}_{nm}}\right] \omega^2 \text{Im}\,\mathbf{G}(r, r_A, \omega) \cdot \mathbf{d}_{mn} \hat{A}_{mn}(t),$$

$$(2.18)$$

where the symbol P represents the Cauchy principal value, a method for evaluating integrals that would otherwise be undefined due to a singularity at the point of integration. The field now solely relies on the flip operators' values at time t, effectively erasing any memory of the atom's internal dynamic states from previous moments. This leads to the practical application of the Markov approximation.

The next step is to solve the Heisenberg equation of motion for the atom. This is achieved through the rearrangement of the equation of motion

$$\dot{\hat{\mathbf{A}}}_{mn}(t) = i\omega_{mn}\hat{\mathbf{A}}_{mn}(t) \quad (2.19)$$
$$+ \frac{i}{\hbar}\sum_k \int_0^\infty d\omega \left[\hat{\mathbf{A}}_{mk}\mathbf{d}_{nk} - \hat{\mathbf{A}}_{kn}\mathbf{d}_{km} \cdot \hat{\mathbf{E}}(\mathbf{r}_A, \omega)\right.$$
$$\left. + \hat{\mathbf{E}}(\mathbf{r}_A, \omega) \cdot \left(\mathbf{d}_{nk}\hat{\mathbf{A}}_{mk} - \mathbf{d}_{km}\hat{\mathbf{A}}_{kn}\right)\right]. \quad (2.20)$$

Combining Equation (2.2) and Equation (2.19) and using the orthogonality of the eigenstates $\hat{A}_{mn}(t)\hat{A}_{kl}(t) = \delta_{nk}\hat{A}_{ml}(t)$, we can find closed equation of motion for the atomic flip operators

$$
\begin{aligned}
\langle \dot{\hat{\mathbf{A}}}_{mn}(t) \rangle = {}& i\omega_{mn} \langle \hat{A}_{mn}(t) \rangle \\
& + \sum_{k,l} \big[\boldsymbol{d}_{km} \mathbf{C}_{nl} \langle \hat{A}_{kl}(t) \rangle + \boldsymbol{d}_{nk} \mathbf{C}_{ml}^{*} \langle \hat{A}_{lk}(t) \rangle \\
& - \boldsymbol{d}_{nk} \mathbf{C}_{kl} \langle \hat{A}_{ml}(t) \rangle - \boldsymbol{d}_{km} \mathbf{C}_{mkl}^{*} \langle \hat{A}_{ln}(t) \rangle \big],
\end{aligned}
\tag{2.21}
$$

with the coefficients

$$
\begin{aligned}
\mathbf{C}_{mn} = {}& \mathbf{C}_{mn}(\boldsymbol{r}_A) \\
= {}& \frac{\mu_0}{\hbar} \Theta(\tilde{\omega}_{nm}) \tilde{\omega}_{nm}^2 \mathrm{Im}\mathbf{G}(\boldsymbol{r},\boldsymbol{r}_A,\tilde{\omega}_{nm}) \cdot \boldsymbol{d}_{mn} \\
& - \frac{i\mu_0}{\pi\hbar} \mathrm{P} \int_0^\infty \frac{d\omega}{\omega - \tilde{\omega}_{nm}} \omega^2 \mathrm{Im}\mathbf{G}(\boldsymbol{r},\boldsymbol{r}_A,\omega) \cdot \boldsymbol{d}_{mn}.
\end{aligned}
\tag{2.22}
$$

We want to decouple this set of linear differential equations by assuming that the atom is free of any quasi degenerate transitions, meaning transitions where no two states belong to the same manifold. In addition, we assume that the free atom is unpolarised in each of its energy eigenstates, so it is not interacting with any field and has no preferred orientation/ direction or net separation of charges with other atoms $\boldsymbol{d}_{nn} = 0$, and the states of a degenerate manifold are not connected by electric-dipole transitions, so $\boldsymbol{d}_{nn'} = 0$, meaning that transitions between energy eigenstates within degenerate manifolds can not be induced by an electronic dipole interaction. These assumptions help to decouple the fast-oscillating off-diagonal flip operator effectively from the non-oscillationg diagonal ones as well as from each other. Thus, the diagonalised coupling matrix reads for the off-diagonal elements ($m \neq n$)

$$
\langle \dot{\hat{\mathbf{A}}}_{mn}(t) \rangle = \left[i\omega_{mn} - \sum_k (\boldsymbol{d}_{nk} \cdot \mathbf{C}_{kn} + \boldsymbol{d}_{km} \cdot \mathbf{C}_{km}^{*}) \right] \langle \hat{A}_{mn}(t) \rangle,
\tag{2.23}
$$

and the non-oscillating diagonalised elements, by considering the atomic selection rules

$$
\langle \dot{\hat{\mathbf{A}}}_{mn}(t) \rangle = -\sum_k (\boldsymbol{d}_{nk} \cdot \mathbf{C}_{kn} + \boldsymbol{d}_{kn} \cdot \mathbf{C}_{kn}^{*}) \langle \hat{A}_{nn}(t) \rangle + \sum_k (\boldsymbol{d}_{kn} \cdot \mathbf{C}_{nk} + \boldsymbol{d}_{nk} \cdot \mathbf{C}_{nk}^{*}) \langle \hat{A}_{kk}(t) \rangle.
\tag{2.24}
$$

Separating the coupling terms into their real and imaginary parts

$$\sum_k \mathbf{d}_{nk} \cdot \mathbf{C}_{kn} = \frac{1}{2} \sum_{k<n} \Gamma_{nk} + i \sum_k \delta\omega_{nk} = \frac{1}{2}\Gamma_n + i\delta\omega_n, \tag{2.25}$$

$$\sum_k \mathbf{d}_{kn} \cdot \mathbf{C}^*_{nk} = \frac{1}{2} \sum_{k<n} \Gamma_{nk} - i \sum_k \delta\omega_{nk} = \frac{1}{2}\Gamma_n - i\delta\omega_n, \tag{2.26}$$

the spectral detuning and transition rates can be found

$$\delta\omega_n = \sum_k \delta\omega_{nk}, \tag{2.27}$$

and

$$\Gamma_n = \sum_{k<n} \Gamma_{nk}, \tag{2.28}$$

respectively, with

$$\delta\omega_{nk} = \delta\omega_{nk}(\mathbf{r}_A) = -\frac{\mu_0}{\pi\hbar}\mathrm{P}\int_0^\infty \frac{d\omega}{\omega - \tilde{\omega}_{nk}}\omega^2 \mathbf{d}_{nk} \cdot \mathrm{Im}\mathbf{G}^{(1)}(\mathbf{r}_A, \mathbf{r}_A, \omega) \cdot \mathbf{d}_{kn}, \tag{2.29}$$

$$\Gamma_{nk} = \Gamma_{nk}(\mathbf{r}_A) = \frac{2\mu_0}{\hbar}\tilde{\omega}^2_{nk}\mathbf{d}_{nk} \cdot \mathrm{Im}\mathbf{G}^{(1)}(\mathbf{r}_A, \mathbf{r}_A, \tilde{\omega}_{nk}) \cdot \mathbf{d}_{kn}. \tag{2.30}$$

The frequency $\tilde{\omega}_{mn}$ is defined as

$$\tilde{\omega}_{mn} = \omega_{mn} + \delta\omega_m - \delta\omega_n, \tag{2.31}$$

meaning the spectral shifts need to be considered by estimating the transition rate. However, in common experimental situations the shift's impact is neglectable, $\tilde{\omega}_{nm} \cong \omega_{nm}$. Thus, and the equations of motions for the flip operators take the form

$$\left\langle \dot{\hat{\mathbf{A}}}_{nn}(t) \right\rangle = -\Gamma_n \left\langle \hat{\mathbf{A}}_{nn}(t) \right\rangle + \sum_{k>n} \Gamma_{kn} \left\langle \hat{\mathbf{A}}_{kk}(t) \right\rangle, \tag{2.32}$$

$$\left\langle \dot{\hat{\mathbf{A}}}_{mn}(t) \right\rangle = [i\tilde{\omega}_{mn} - \frac{1}{2}(\Gamma_m + \Gamma_n)]\left\langle \hat{\mathbf{A}}_{mn}(t) \right\rangle \quad \text{for } m \neq n, \tag{2.33}$$

leading to the time dependence of the atomic density matrix elements

$$\dot{p}_n(t) = -\Gamma_n p_n(t) + \sum_{k>n} \Gamma_{kn} p_k(t), \tag{2.34}$$

$$\sigma_{mn}(t) = \exp\left(-i\tilde{\omega}_{mn} - \frac{1}{2}(\Gamma_m + \Gamma_n)\right)(t - t_0)\sigma_{mn} \quad \text{for } m \neq n. \tag{2.35}$$

The dynamics are also known as a spontaneous decay, describing the emission of real photons. Due to the spontaneous decay p_n, the population of a given states $|n\rangle$, is reduced to lower lying states to gain the population transfer from higher states. Equation (2.28) defines the total decay rate by summing up over all transition rates to lower lying states. From this, we can define the lifetime of an excited state by taking the inverse of the total decay rate, $\tau_n = \frac{1}{\Gamma_n}$. By dividing the Green's function into its bulk and scattering part

$$\mathbf{G}(r, r', \omega) = \mathbf{G}^{(0)}(r, r', \omega) + \mathbf{G}^{(S)}(r, r', \omega), \tag{2.36}$$

the natural linewidth is obtainable by inserting the bulk Green's function $\mathbf{G}^0(r, r', \omega)$ into Equation (2.29), leading to the well known Einstein coefficient, Ref. [21]

$$\Gamma_n = \frac{1}{3\pi\varepsilon_0\hbar c^3} \sum_{k<n} \omega_{nk}^3 |\mathbf{d}_{nk}|^2. \tag{2.37}$$

As above-mentioned, the lifetime of a transition process from the highest to the lowest energy state can be expressed as the inverse of the transition rate, leading to

$$\tau_n = \frac{1}{\Gamma_n} = \frac{3\pi\varepsilon_0\hbar c^3}{\sum_{k<n} \omega_{nk}^3 |\mathbf{d}_{nk}|^2}. \tag{2.38}$$

Using this expression the fluorescence lifetime of any atom/ molecule can be calculated in vacuum by inserting the transition frequency as well as the transition dipole moment.

To this end, the scattering part of the Green's function considers the solvent effects. A local-field correction incorporating the solvent's and the carbon dot's impact will be derived in Chapter 2.5. We aim to delve deeper into the frequency shift described in Equation (2.27). By applying the relationship given in (2.2), we understand that the shift noted in Equation (2.27) results from a transition between states. This is dependent on the atomic frequency, the dipole matrix element and the electromagnetic Green's tensor, including the surrounding's impact.

2.3 The spectrum of the hydrogen atom

This section aims to provide some understanding of how to compute the transition dipole moments of an atom. Since hydrogen is the only atom that can be solved ana-

lytically, it is used to demonstrate how to derive dipole moments. Analytical computations for the hydrogen atom can yield the transition dipole moments. The general formula for the hydrogens dipole operator has been derived and implemented in python afterwards. This method shows how transition dipole moments can be theoretically calculated by hand with respect to the selection rules. The hydrogen atoms has been chosen as it can be found an analytically solution for it. Using the general formula for the dipoloperator [24]

$$\mathbf{d}_{nlmn'l'm'} = -e^2 \int \Psi^*_{nlm} \mathbf{r} \Psi'_{n'l'm'} r^2 \sin \vartheta dr d\vartheta d\varphi, \tag{2.39}$$

with e as the elementary charge. We will study its general properties by considering the hydrogen atom, whose wavefunction separates into a radial and an angular part

$$\Psi_{nlm}(\mathbf{r}, \vartheta, \varphi) = R_{nl}(\mathbf{r}) Y^m_l(\vartheta, \varphi). \tag{2.40}$$

Thus the integral (2.39) separates and we will evaluate each part separately.

The Angular Part

The normalized angular part, the so called spherical harmonics [24] is given as

$$Y^m_l(\vartheta, \varphi) = \varepsilon \sqrt{\frac{(2l+1)(l-|m|)!}{4\pi(l+|m|)!}} e^{im\varphi} P^m_l(\cos \vartheta). \tag{2.41}$$

with

$$\varepsilon = \begin{cases} (-1)^m & m \geq 0 \\ 1 & m < 0 \end{cases} \tag{2.42}$$

P^m_l is the associated Legendre function [24], defined by

$$P^m_l(x) = \left(1 - x^2\right)^{\frac{|m|}{2}} \left(\frac{d}{dx}\right)^{|m|} P_l(x). \tag{2.43}$$

$P_l(x)$ is the *lth* Legendre polynomial, defined by the Rodriguez formula [24], which can be written as

$$P_l(x) \equiv \frac{1}{2^l l!} \left(\frac{d}{dx}\right)^l (x^2 - 1)^l. \tag{2.44}$$

Using these relations and introducing spherical coordinates, we write the angular part of Equation 2.39 as

$$f = \int_0^{2\pi} d\varphi \int_0^{\pi} d\vartheta \sin\vartheta \, (Y_l^m(\vartheta, \varphi))^\star \begin{pmatrix} \sin\vartheta\cos\varphi \\ \sin\vartheta\sin\varphi \\ \cos\vartheta \end{pmatrix} Y_{l'}^{m'}(\vartheta, \varphi). \tag{2.45}$$

This integral can be separated into its three spatial components, f_x, f_y, f_z

$$f_x = -\frac{\varepsilon\varepsilon'(2l'+1)}{16} \sqrt{\frac{(l'-m')!^2}{(l'+m')!^2}} \begin{cases} \frac{\sqrt{(2l'+3)(l'-m'+2)!}}{\sqrt{(l'+m'+2)!(2l'+2)}} & \text{(i)} \\[2ex] -\frac{\sqrt{(2l'-1)}}{\sqrt{(l'+m')!(2l'-1)}} & \text{(ii)} \\[2ex] -\frac{\sqrt{(2l'+3)(l'-m'+2)!}(l'-m'+3)(l'-m'+4)}{\sqrt{(l'+m')!(2l'+3)}} & \text{(iii)} \\[2ex] \frac{\sqrt{(2l'-1)(l'-m'+1)(l'-m'+2)}}{\sqrt{(l'+m'-2)!(2l'-1)}} & \text{(iv)} \end{cases} \tag{2.46}$$

where $(i)m' = m - 1, l' = l - 1; (ii)m' = m - 1, l' = l + 1; (iii)m' = m + 1, l' = l - 1; (iv)m' = m + 1, l' = l + 1$. For the y-component we obtain

$$f_y = -\varepsilon\varepsilon' \begin{cases} \sqrt{\frac{(2l'+3)(l'-m'+2)!(2l'+1)(l'-m')!}{16(l'+m'+2)!(l'+m')!}} \frac{i}{2l'+2} & \text{(i)} \\[2ex] \sqrt{\frac{(2l'-1)(l'-m')!(2l'+1)(l'-m')!}{16(l'+m')!(l'+m')!}} \frac{-i}{2l'-1} & \text{(ii)} \\[2ex] \sqrt{\frac{(2l'+3)(l'-m'+2)!(2l'+1)(l'-m')!}{16(l'+m')!(l'+m')!}} \frac{-i(l'-m'+3)(l'-m'+4)}{2l'+3} & \text{(iii)} \\[2ex] \sqrt{\frac{(2l'-1)(l'-m')!(2l'+1)(l'-m')!}{16(l'+m'-2)!(l'+m')!}} \frac{i(l'-m'+1)(l'-m'+2)}{2l'-1} & \text{(iv)} \end{cases} \tag{2.47}$$

where $(i)m = m' + 1, l = l' + 1; (ii)m = m' + 1, l = l' - 1; (iii)m = m' - 1, l = l' + 1; (iv)m = m' - 1, l = l' - 1$.

The z component result for the case $m = m', l = l' + 1$ is

$$f_z = \varepsilon\varepsilon' \sqrt{\frac{(2l'+3)(l'+1-m')!(2l'+1)(l'-m')!}{16\pi^2(l'+1+m')!(l'+m')!}} \pi \sqrt{\frac{(l'+2)^2 - m'^2}{4(l'+2)^2}} \tag{2.48}$$

And for $m = m', l = l' - 1$:

$$f_z = \varepsilon\varepsilon' \sqrt{\frac{(2l'-1)(l'-1-m')!(2l'+1)(l'-m')!}{16\pi^2(l'-1+m')!(l'+m')!}} \pi \sqrt{\frac{(l'-1+m')^2}{4l'^2}} \tag{2.49}$$

The selection rules for the dipole operator in hydrogen show that transitions between energy levels are only allowed if the change in the angular momentum quantum number by one $\Delta l = l - l' = \pm 1$ and the change in the magnetic quantum number $\Delta m = m - m' = 0, \pm 1$. These rules are critical for understanding the spectroscopic properties of hydrogen, as they govern the allowed transitions that can be induced by electromagnetic radiation.

The Radial Part

The radial part $R_{nl}(r)$ reads

$$\begin{aligned} R_{nl}(r) &= \sqrt{\left(\frac{2}{na_0}\right)^3 \frac{(n-l-1)!}{2n(n+l)!}} e^{-r/(na_0)} \left(\frac{2r}{na_0}\right)^l L_{n-l-1}^{2l+1}\left(\frac{2r}{na_0}\right) \\ &= f_{nl} e^{-r/(na_0)} \left(\frac{2r}{na_0}\right)^l L_{n-l-1}^{2l+1}\left(\frac{2r}{na_0}\right), \end{aligned} \tag{2.50}$$

with the prefactor

$$f_{nl} = \sqrt{\left(\frac{2}{na_0}\right)^3 \frac{(n-l-1)!}{2n(n+l)!}}. \tag{2.51}$$

Therefore, the integral over the radial part of the dipole operator can be evaluated as follows

$$R = \int_0^\infty r^3 R_{nl}(r) R_{n'l'}(r) dr \tag{2.52}$$

$$= f_{nl} f_{n'l'} \left(\frac{2}{na_0}\right)^l \left(\frac{2}{n'a_0}\right)^{l'} \left(\frac{na_0}{2}\right)^{4+l+l'} \int_0^\infty dx\, e^{-bx} x^{3+l+l'} L_{n-l-1}^{2l+1}(x) L_{n'-l'-1}^{2l'+1}(\mu x) \tag{2.53}$$

with $b = \frac{n(\frac{1}{n}+\frac{1}{n'})}{2}$ and $\mu = \frac{n}{n'}$. By using the 3-point rules for lowering and highering the upper index the integral (2.52) can be transformed to the form [25], as can be seen in the appendix A.2.

Hence, the radial part can be integrated analytically and yields for the case $l' = l + 1$

$$
\begin{aligned}
R = &\int L_{\mu n'-l-1}^{2l+4}(x) L_{n'-l-2}^{2l+4}(\mu x) - 3 \int L_{\mu n'-l-2}^{2l+4}(x) L_{n'-l-2}^{2l+4}(\mu x) \\
&+ 3 \int L_{\mu n'-l-3}^{2l+4}(x) L_{n'-l-2}^{2l+4}(\mu x) - \int L_{\mu n'-l-4}^{2l+4}(x) L_{n'-l-2}^{2l+4}(\mu x) \\
&- \int L_{\mu n'-l-1}^{2l+4}(x) L_{n'-l-3}^{2l+4}(\mu x) + 3 \int L_{\mu n'-l-2}^{2l+4}(x) L_{n'-l-3}^{2l+4}(\mu x) \\
&- 3 \int L_{\mu n'-l-3}^{2l+4}(x) L_{n'-l-3}^{2l+4}(\mu x) + \int L_{\mu n'-l-4}^{2l+4}(x) L_{n'-l-3}^{2l+4}(\mu x)
\end{aligned} \tag{2.54}
$$

and for the case $l' = l - 1$

$$
\begin{aligned}
R = &\int L_{\mu n'-l-1}^{2l+2}(x) L_{n'-l}^{2l+2}(\mu x) - 3 \int L_{\mu n'-l-1}^{2l+2}(x) L_{n'-l-1}^{2l+2}(\mu x) \\
&+ 3 \int L_{\mu n'-l-1}^{2l+2}(x) L_{n'-l-2}^{2l+2}(\mu x) - \int L_{\mu n'-l-1}^{2l+2}(x) L_{n'-l-3}^{2l+2}(\mu x) \\
&- \int L_{\mu n'-l-2}^{2l+2}(x) L_{n'-l}^{2l+2}(\mu x) + 3 \int L_{\mu n'-l-2}^{2l+2}(x) L_{n'-l-1}^{2l+2}(\mu x) \\
&- 3 \int L_{\mu n'-l-2}^{2l+2}(x) L_{n'-l-2}^{2l+2}(\mu x) + \int L_{\mu n'-l-2}^{2l+2}(x) L_{n'-l-3}^{2l+2}(\mu x).
\end{aligned} \tag{2.55}
$$

Combined Dipole Operator

The complete expression for the dipole operator of the hydrogen atom can be finally evaluated by multiplying the expression for the radial part and the angular part

$$
\mathbf{d} = (f_x \hat{\mathbf{e}}_x + f_y \hat{\mathbf{e}}_y + f_z \hat{\mathbf{e}}_z) \cdot R, \tag{2.56}
$$

with respect to the allowed combinations of quantum numbers n, n', l, l', m, m'. The calculation has been implemented in python, the code can be found in appendix A.3.

2.4   The Emission Spectrum of Hydrogen

After the angular and radial component formulas are obtained in section 2.3, they are multiplied together to find the hydrogen dipole moments for different transitions, Equation (2.56). The resulting transition rates Γ_{nm} and transition frequencies ω_{nm} for
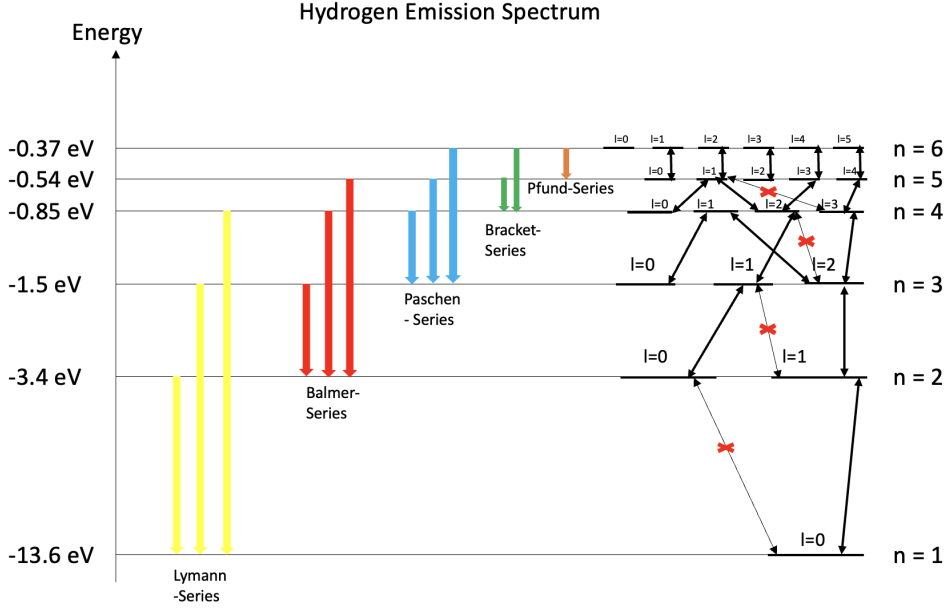
Figure 2.3: The emission spectrum of hydrogen, the arrows indicate the Lymann-series (yellow), Balmer-series (red), Paschen-series (blue), Bracket-series (green) and Pfund-series (orange). Transitions that are not allowed are indicated by the grey-white arrows that are crossed.

the first five transitions are listed in Table 2.1, and the resulting emergent emission spectrum is shown in Figure 2.3. One can see that the estimated excitation lifetimes are very short, meaning an excitation will almost instantaneously relax into the ground state, which is in agreement with the sharp spectroscopic lines of the hydrogen spectrum, [26].

As an example to show how the lifetime can be calculated via the single transition rates, we have a look at the Lymann-Series, using Equation (2.28) and (2.38). The Lymann series describes direct transitions into the ground state, thus $n = 1$ and $m = 2, 3, 4 \ldots$, as indicated by the first transition (yellow arrow from $n = 4$ to $n = 1$) in Figure 2.4.

As the decay from the fourth state into the ground state can occur via different processes, the resulting total transition rate can be obtained according to Fig. 2.4 by

$$\Gamma_{tot,41} = \Gamma_{41} + \Gamma_{43}\Gamma_{31} + \Gamma_{42}\Gamma_{21} + \Gamma_{43}\Gamma_{32}\Gamma_{21}, \tag{2.57}$$

leading to a total transition rate of $\Gamma_{tot,41} = 1.655 \times 10^{63} s^{-1}$ and the resulting excitation lifetime is $\tau_{tot,41} = 1/\Gamma_{tot,41} = 6.042 \times 10^{-64} s$. In contrast, the excitation lifetime for

Series	n	m	Transition frequency ω_{nm} in (Hz)	Transition rate Γ_{nm} in (s^{-1})
Lyman	1	2	1.5503×10^{16}	9.2308×10^{22}
	1	3	1.8374×10^{16}	2.9207×10^{22}
	1	4	1.9379×10^{16}	1.2558×10^{22}
Balmer	2	3	2.8709×10^{15}	6.1251×10^{20}
	2	4	3.8758×10^{15}	3.5613×10^{20}
	2	5	4.3408×10^{15}	2.0415×10^{20}
Paschen	3	4	1.0048×10^{15}	2.9271×10^{19}
	3	5	1.4699×10^{15}	2.2879×10^{19}
	3	6	1.7226×10^{15}	1.5636×10^{19}
Brackett	4	5	4.6509×10^{14}	3.2585×10^{18}
	4	6	7.1773×10^{14}	3.0397×10^{18}
Pfund	5	6	2.5264×10^{14}	5.8337×10^{17}

Table 2.1: Transition frequencies and lifetimes for the hydrogen atom in vacuum, calculated with the derived formula for the dipole operator of hydrogen. In the final state, denoted as m, the orbital quantum number l takes the value $l = 1$, and the magnetic quantum number m is $m = 1$. Conversely, in the initial state, denoted as n, $l = 0$ and $m = 0$.

the direct transition Γ_{41} is $\tau_{41} = 1/\Gamma_{41} = 7.96 \times 10^{-23} s$.

It can be observed from Table 2.1 that the transition rates and frequencies for each series of the emission spectrum are in the same order of magnitude, and both decrease with the number of the excited state. Notably, the excitation lifetime calculated for the total decay process ($\tau_{tot,41} = 2.63 \times 10^{-28} s$) is significantly different from the excitation lifetime obtained from the direct decay from $4 \to 1$ ($\tau_{41} = 7.96 \times 10^{-23} s$). This difference underscores that decay via several excited states is shorter than direct decay, indicating that the number of decay channels influences the lifetime of the excitation duration.

As previously explained in Section 2.2, and indicated in Equation 2.29, spectral shifts need to be accounted for to estimate accurate transition rates. This highlights the importance of including total decay over several excited states in the analytical calculations of the process.
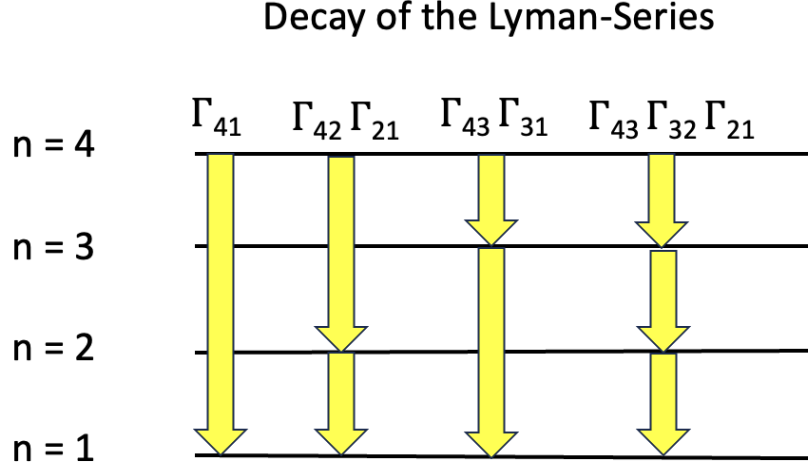
Decay of the Lyman-Series

Figure 2.4: The total decay rate of the Lyman series Γ_{41} via all possible combinations of single decays shown with yellow arrows pointing along the different states.

2.5 Calculating scattering effects in presence of a field

In this section we'll discuss the tools to calculate scattering effects on the precursor molecules occurring due to the presence of the carbon core, the molecules are bonded to. The behaviour of the electromagnetic field in presence of an external field can be described by the vector Helmholtz Equation (2.10), where $\varepsilon(\mathbf{r}, \omega)$ is the electric permittivity and $\mathbf{j}(\mathbf{r}, \omega)$ is the current density. This inhomogenity can formally be solved via a convolution

$$\mathbf{E}(\mathbf{r}, \omega) = i\mu_0\omega \int d^3r' \mathbf{G}(\mathbf{r}, \mathbf{r}', \omega) \cdot \mathbf{j}(\mathbf{r}', \omega). \tag{2.58}$$

of the inhomogenity with the fundamental solution $\mathbf{G}(\mathbf{r}, \mathbf{r}')$, obeying

$$\nabla \times \nabla \times \mathbf{G}(\mathbf{r}, \mathbf{r}', \omega) - \frac{\omega^2}{c^2}\varepsilon(\mathbf{r}, \omega)\mathbf{G}(\mathbf{r}, \mathbf{r}', \omega) = \delta(\mathbf{r} - \mathbf{r}'). \tag{2.59}$$

Analytic solutions for the Green's functions are known for certain geometries [21]. For systems beyond these cases, approximation methods exist, such as the Born-series expansion, which will be introduced in the following. As previously stated in Equation (2.36), we can decompose the function into an analytically known part (representing the vacuum, bulk, or layered material) and an unknown part (representing the scattering Green's function), denoted as $\mathbf{G}^{(0)}(\mathbf{r}, \mathbf{r}', \omega)$ and $\mathbf{G}^{(S)}(\mathbf{r}_A, \mathbf{r}_A, \omega)$, respectively. The analytically known part satisfies

$$\nabla \times \nabla \times \mathbf{G}^{(0)}(\mathbf{r}, \mathbf{r}', \omega) - \frac{\omega^2}{c^2}\varepsilon(\mathbf{r}, \omega)\mathbf{G}^{(0)}(\mathbf{r}, \mathbf{r}', \omega) = \delta(\mathbf{r} - \mathbf{r}'). \tag{2.60}$$

To obtain a solution for the scattering Green's function, we take the difference between Equations (2.59) and (2.60) to solve the inhomogeneous Helmholtz equation

$$\nabla \times \nabla \times \mathbf{G}^{(S)}(\boldsymbol{r}, \boldsymbol{r}', \omega) - \frac{\omega^2}{c^2} \varepsilon(\boldsymbol{r}, \omega) \mathbf{G}^{(S)}(\boldsymbol{r}, \boldsymbol{r}', \omega)$$
$$= \frac{\omega^2}{c^2} \delta\varepsilon(\boldsymbol{r}, \omega) \left[\mathbf{G}^{(0)}(\boldsymbol{r}, \boldsymbol{r}', \omega) + \mathbf{G}^{(S)}(\boldsymbol{r}, \boldsymbol{r}', \omega) \right]. \qquad (2.61)$$

The perturbation of the permittivity is written as $\delta\varepsilon(\mathbf{r}, \omega) \equiv \varepsilon(\mathbf{r}, \omega) - \varepsilon_0(\mathbf{r}, \omega)$, where ε is representing the mediums permittivity and ε_0 the vacuum permittivity. A general and formal solution to the scattering part can be found with

$$\mathbf{G}^{(S)}(\mathbf{r}, \mathbf{r}', \omega) = \int d^3r \, \mathbf{G}^{(0)}(\mathbf{r}, \mathbf{s}, \omega) \frac{\omega^2}{c^2} \delta\varepsilon(\mathbf{s}, \omega) [\mathbf{G}^{(0)}(\mathbf{s}, \mathbf{r}', \omega) + \mathbf{G}^{(S)}(\mathbf{s}, \mathbf{r}', \omega)]. \qquad (2.62)$$

2.6 Carbon Nanodots

Carbon dots (CDs) are versatile materials with a wide range of sources, a small particle size, and cost-effectiveness, [27]. They possess a high fluorescence yield, making them attractive for industrial applications like pH sensors, [28]. Another type of fluorescent nanomaterials, known as carbon quantum dots (CQDs), is also gaining prominence for various purposes, including sensing and therapy, [29]. In contrast to traditional quantum dots, CQDs offer advantages like safe composition, adjustable fluorescence, and stability. While their affordability and ease of production are strengths, addressing challenges such as purification and low quantum yields is necessary for their success in fields like bioimaging and nanomedicine, [29].

2.6.1 What are Carbon Nanodots

Carbon Quantumdots are small ($< 10nm$) sized, spherical particles that can consist of an organic precursor attached to a carbon structure surface. The structure can be classified as a core-shell structure: We have a core with sp^2 and sp^3 hybridized carbon atoms as well as a shell consistent of functional groups that are attached to the core [30].

The main constituent element of CDs is carbon. We can classify CDs into several "sub
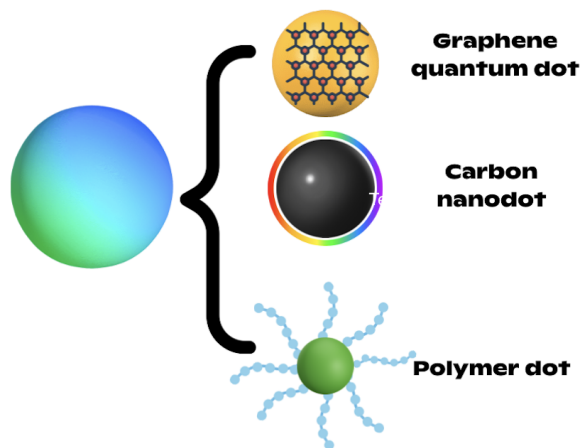
Figure 2.5: Different types of carbon dots: graphene quantum dots, carbon nanodots, carbonized polymer dots. Adapted from [31].

groups", depending on their surface states and core structure, such as graphene quantum dots, carbon nano dots and carbonized polymer dots, represented in Figure 2.5.

Due to the hybridization and synergy effects between the core and the surface chemical groups, different luminescence characteristics can be observed in CDs, such as the fluorescence emission mechanism. These factors include:

- **Quantum conjugation effects:** The extent of π-conjugation within carbon dots can affect their electronic structure, leading to changes in their absorption and emission properties. Enhanced conjugation can result in a narrowing of the band gap, thus affecting the fluorescence emission.

- **Surface states:** The specific atoms or functional groups present on the surface of carbon dots can introduce localized energy states, which play a critical role in determining the fluorescence characteristics. Surface states can trap excitation energy, leading to varied emission wavelengths.

- **Cross-link enhanced emission effects:** The formation of cross-links within or between carbon dots can lead to enhanced fluorescence emission. This is attributed to the restriction of non-radiative relaxation processes, facilitating more efficient radiative decay.

- **Molecular states:** The presence of specific molecular states within carbon dots, arising from heteroatoms or defects, can influence their fluorescence emission.

These states can act as emission centers, contributing to the diversity of emission wavelengths observed.

- **Environmental effects:** The local environment around carbon dots, including solvent polarity, pH, and ionic strength, can significantly influence their fluorescence emission. Environmental factors can affect the electronic states of carbon dots, leading to shifts in fluorescence wavelength and intensity.

2.6.2   Luminescence Mechanism in Carbon Dots

To gain a deeper understanding of the luminescence mechanism of Carbon Dots it is essential to have a look at their structure property relations. CDs show to have a very high fluorescence yield. A CDs fluorescence characteristics is caused due to the sp^2/sp^3 hybridization of the carbon core as well as synergy effects between the core and the surface functional groups [30]. Fluorescence behavior can be categorized into two distinct types: one where the fluorescence emission varies with the excitation wavelength, and another where the emission remains consistent regardless of the excitation wavelength. Factors influencing those phenomena are the size and surface defects of the CDs as well as different carbon structures.

Quantum Conjugation Effects

Carbon Quantum Dots are $sp^2 - sp^3$ hybridized. The hybridization of carbon atoms within carbon dots influences their entire structure, properties, and behavior. These attributes render carbon dots adaptable and precious for a range of applications, such as bioimaging, sensing, and optoelectronics. The integration of sp^2 and sp^3 hybridized carbon atoms in carbon dots enhances their distinct optical and electronic traits, underscoring their significance in both research and technological advancements [32, 30]. In sp^2 hybridization, one s orbital and two p orbitals from the same atom combine to form three new hybrid orbitals, as demonstrated in Figure 2.6. These hybrid orbitals are in the same plane and are directed towards the corners of an equilateral triangle, with bond angles of approximately 120 degrees. This type of hybridization is often seen in carbon atoms that are part of double bonds or are involved in trigonal planar structures, like graphene.
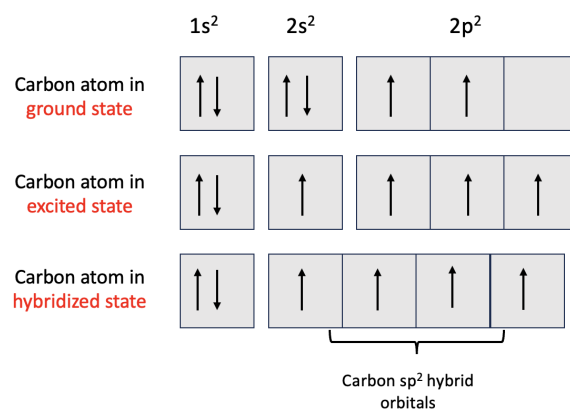
$1s^2$ $2s^2$ $2p^2$

Carbon atom in
ground state

Carbon atom in
excited state

Carbon atom in
hybridized state

Carbon sp^2 hybrid
orbitals

Figure 2.6: Example of electron distribution in a carbon atom during its ground, excited and hybridized state. Adapted from [33].

In sp^3 hybridization, one s orbital and three p orbitals from the same atom combine to form four new hybrid orbitals. These hybrid orbitals are directed towards the corners of a tetrahedron, maximizing the angles between them at approximately 109.5 degrees. This type of hybridization is commonly observed in carbon atoms that form single bonds in molecules like methane or in tetrahedral structures. The functional groups attached to the carbon surface can show such behaviour, depending on their molecular strucutre. The quantum conjugation effect occurs when small sp^2 domain sizes lead to discrete electron energy levels near the Fermi level, altering from quasi-continuous levels. As sp^2 domain size grows, the band gap decreases, causing a redshift in the photoluminescence emission spectra. This effect significantly impacts the fluorescence properties of quantum dot materials [32].

Surface Funtional Groups

An area of research worthy of exploration involves the attachment of surface functional groups to carbon dots. These surface functional groups exert a notable influence on the geometric and electronic structure of carbon dots, consequently affecting their fluorescence characteristics. Remarkably, various functional groups can yield distinct surface emission states, offering a means to finely tailor the emission spectrum of carbon dots [34]. For instance, it has been demonstrated that electron-donating amino groups not only induce a redshift but also maintain a substantial oscillating strength in fundamental radiative transitions [34]. Additionally, the introduction of amino

groups onto the surface of carbon dots leads to a diminishing LUMO (lowest unoccupied molecular orbital)-HOMO (highest occupied molecular orbital) energy band gap [35]. When examining the impact of diverse surface functional groups on the photoluminescent properties of carbon dots, it becomes evident that alterations in surface chemistry exert a profound influence, not only on their size and solubility but also on their optical characteristics [36].

Environmental Effects

The investigation of environmental factors, such as pH, pressure, and temperature, emerges as a critical avenue of study, as these variables are known to exert unique and substantive effects on the properties of carbon dots.

As an illustrative example, a study has demonstrated that stable red-emissive carbon dots in a solution exhibit heightened fluorescence in response to external pressure. This phenomenon arises from the increased proximity of the molecules, effectively impeding interparticle oscillations. Consequently, a pronounced intra-molecular charge transfer mechanism is triggered, ultimately amplifying the emission intensity [37].

Furthermore, researchers have explored the pressure-induced color change in carbon dots employing piezochromatic carbon dots with two-photon fluorescence capabilities. The investigation has unveiled that, under high pressure conditions, the initially sp^2-hybridized domains undergo a transformation into sp^3-hybridized domains [38]. Two-photon fluorescence is a nonlinear optical phenomenon in which a fluorophore (like carbon dots) absorbs two photons of lower energy simultaneously, causing it to emit a photon of higher energy (shorter wavelength). This process occurs only at high photon densities, typically generated by intense laser beams [39]. Another important emission-tuning environmental factor is the pH value, which is the main research interest of this thesis and discussed intensely in the next sub-chapter.

2.7   Understanding pH

As, in this thesis, the change of the fluorescence lifetime of CDs in a solution is modeled, the pH value is an important factor to be discussed. The surrounding solution can have a different pH value that can impact the structure and therefore the fluores-

cence lifetime of the CDs. The pH value, representing the "potential" or "power" of hydrogen, serves as a scale to express the acidity or basicity of a solution in aqueous environments. The concentration of hydrogen ions (H^+) is pivotal in determining the acidity (high H^+ activity) or basicity/alkalinity (low activity) of a substance.

The reactivity of a solution increases with its acidity or basicity, influencing biological reactions and guiding chemical reactions. Following Johannes N. Brønsted's definition, a base possesses a non-committal pair of electrons, capable of accepting a proton (H^+), while an acid donates a proton. Acidic substrates release H^+ ions [40].

2.7.1 pH Calculation

The properties of acids and bases are governed by ions. To establish the equation for calculating the pH value, we examine the relationship between hydroxide ions (OH^-) and oxonium ions (H^+) in solutions. Using the dissociation of water as an example, where two water molecules yield one hydroxide ion and one oxonium ion in equilibrium [40]

$$2H_2O \rightleftharpoons H_3O^+ + OH^-. \tag{2.63}$$

For any reaction at equilibrium, an equilibrium constant (K_{eq}) exists

$$K_{eq} = \frac{[H_3O^+][OH^-]}{[H_2O]} = 1.8 \times 10^{-16}, \tag{2.64}$$

where [...] denotes the concentration. This constant involves the ion product of water (K_w)

$$K_w = [H_3O^+][OH^-] = 10^{-14}. \tag{2.65}$$

As the dissociation of water produces equal concentrations (in squared brackets []) of hydroxide and oxonium ions

$$[H_3O^+] = 10^{-7}. \tag{2.66}$$

$$[OH^-] = 10^{-7}. \tag{2.67}$$

Figure 2.7 illustrates the inverse relationship between pH and pOH values, both totaling to 10^{-14} due to the ion product of water [40]. A concentration of 10^{-7} denotes a neutral solution (pure water). Higher concentrations (e.g., 10^{-3}) define acidity, while lower concentrations (e.g., 10^{-10}) define basicity. The pH value is conveniently defined

as

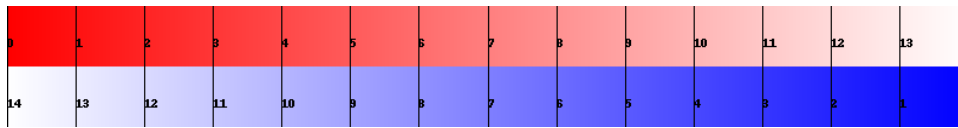$$pH = -\log_{10}[H_3O^+] = -\log_{10}[H^+]. \tag{2.68}$$

Figure 2.7: The inverse dependence of pH and pOH values, both adding up to a concentration of $10^{-14} M$ due to the ion product of water (see Equation (2.65)). The gradient from red to withe refers to the pH value, whereas the gradient from blue to white represents the pOH value.

2.7.2 Henderson-Hasselbalch Equation

In this discussion, we consider the pH-dependent behavior of dye molecules within carbon dots (CDs), which hinges on the equilibrium between their protonated (HD) and deprotonated (D) forms. This equilibrium can be represented as

$$HD \rightleftharpoons H^+ + D, \tag{2.69}$$

where the acid dissociation constant, K_a, is traditionally expressed in logarithmic form as $pK_a = -\log_{10} K_a$. The Henderson–Hasselbalch equation connects this equilibrium with the pH

$$pH = pK_a + \log_{10} \frac{[D]}{[HD]}. \tag{2.70}$$

The Henderson-Hasselbalch equation is particularly useful for examining buffer systems, which are designed to maintain a stable pH under various conditions. These systems typically involve a high concentration of a weak acid and its conjugate base. In the context of dye molecules in CDs, the dissociation of weak acids in buffer solutions can be described by a similar equilibrium constant:

$$K_a = \frac{[H^+][D]}{[HD]}. \tag{2.71}$$

The associated pK_a value is calculated using the negative logarithm.

Applying the Henderson-Hasselbalch equation to this system, we can derive the relationship between the pH and the proportions of the protonated and deprotonated forms of the dye molecules [40].

2.7.3   The pH value as emission tuning factor of Carbon Dots

Carbon dots exhibit remarkable sensitivity to variations in pH levels, primarily attributed to ionization or deprotonation processes affecting their molecular and electronic structures. Consequently, alterations in their surrounding environment can result in observable changes in emission characteristics, manifesting as shifts in wavelength or variations in light intensity. These pH-induced modifications can also impact the spatial arrangement of fluorophores, which function as donor-acceptor pairs [41]. The fluctuations in pH can trigger several key phenomena within carbon dots, including shifts in energy levels, the protonation and deprotonation of surface functional groups, aggregation tendencies, proton transfer events, and the operation of protective shell mechanisms. These intricate responses collectively contribute to the pH-dependent behavior of carbon dots and their utility in a wide range of applications [41, 4].

Protonation and deprotonation

The primary cause of the pH sensitivity shown in the carbon dots' (CDs) fluorescence response is the balance between the dye molecules' embedded protonated (HD) and deprotonated (D) forms. Depending on the specific system being studied, D may be neutral or charged during this pH-dependent partitioning. In particular, when phloroglucinol is deprotonated, its acidic hydroxyl groups have a charge of -1, and when it is protonated, it has a charge of neutrality. Similar to this, mPD has a charge of 1 when protonated and is neutral when deprotonated with basic amine groups. This pattern is likewise followed by the dye dispersion blue1, which has a charge of 1 when protonated and is neutral when deprotonated.

The volume fraction of deprotonated molecules $[f_D(\mathrm{pH})]$ to the total number of dye molecules active on the surface of a CD, and the fraction of active protonated molecules $[f_{HD}(\mathrm{pH} = 1 - f_D]$, are important parameters in determining the fluorescence behavior. The fluorescence transition rate is essentially a linear combination of the transition rates of these protonated and deprotonated molecules.

$$\Gamma(\mathrm{pH}) = f_D(\mathrm{pH})\,\Gamma_D + [1 - f_D(\mathrm{pH})]\,\Gamma_{HD}\,. \tag{2.72}$$
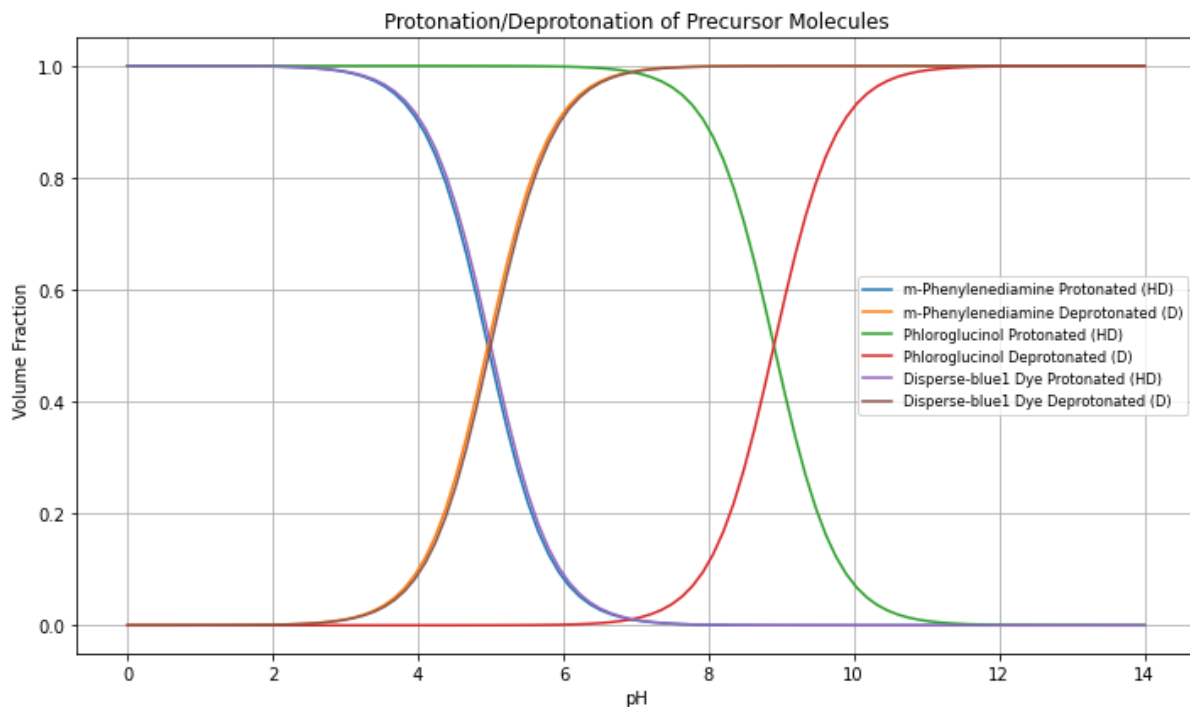
Figure 2.8: The protonation/ deprotonation process of the precursor molecules m-phenylenediamine ($pK_a = 4.98$), phloroglucinol ($pK_a = 8$) and disperse-blue1 dye ($pK_a = 5$) at a concentration of 1 mol/Liter in a pH range from 1 to 14.

Moreover, the pH of the surrounding medium and the pK_a values of the functional groups control the proton exchange dynamics in such a chemical system. Deprotonation results in a steady electron count that now encounters less nuclear charge binding, which increases polarizability. The hybrid quantum-classical model explains this by proposing that anions are more polarizable than cations, and particularly more polarizable than their neutral counterparts. Using Equation (2.70) we can write the dye fractions as

$$f_{\mathrm{D}} = \frac{1}{1 + 10^{pK_a - \mathrm{pH}}}, \tag{2.73}$$

$$f_{\mathrm{HD}} = \frac{1}{1 + 10^{\mathrm{pH} - pK_a}}, \tag{2.74}$$

giving the pH-dependent transition rate of the carbon dot

$$\Gamma(\mathrm{pH}) = \frac{\Gamma_{\mathrm{HD}} + \Gamma_{\mathrm{D}} \, 10^{\mathrm{pH} - pK_a}}{1 + 10^{\mathrm{pH} - pK_a}}, \tag{2.75}$$

which can be linearised with a Taylor series expansion if pK_a lies close to the pH (pH $\approx$

pK_a) region of interest, as

$$\tau(\text{pH}) = \frac{2}{\Gamma_{HD} + \Gamma_D} + \frac{\ln 10 \, (\Gamma_{HD} - \Gamma_D)}{(\Gamma_{HD} + \Gamma_D)^2} \, (\text{pH} - \text{p}K_a) \, . \tag{2.76}$$

Thus, the sensitivity to pH changes, shown by how much the fluorescence lifetime changes with pH $\frac{d\tau}{d\text{pH}}$, can be increased if we make the difference between the transition rates of the protonated and deprotonated species larger ($\Gamma_{HD} - \Gamma_D$). At the same time, we should try to keep these transition rates low when added together ($\Gamma_{HD} + \Gamma_D$). This means we can achieve greater pH-sensitivity to pH if the overall fluorescence lifetime is longer, as long as there's a clear difference in the lifetimes of each kind of molecule that can fluoresce.

An exemplary case is the synthesis of S-C-dots, which are crafted to exhibit pH-sensitive behavior, as opposed to conventional carbon dots. The photoluminescence (PL) intensity of S-C-dots progressively increases across a pH range from 2 to 12, with a pronounced linear relationship evident from pH 3 to 9. This signifies a reversible pH-responsive PL intensity. The increase in PL intensity as the pH moves from acidic (3) towards alkaline (9) conditions is due to the augmented presence of carboxyl groups on the S-C-dot surface, which serve as effective fluorophores. Upon reaching a pH above 9, the concentration of these carboxyl groups nears saturation, leading to a tapering in the rate of PL intensity growth as the pH approaches 12, Ref. [42]. The pH dependency of carbon dots' fluorescence is influenced by proton transfer reactions involving surface functional groups. At lower pH, these groups gain protons, altering the carbon dots' electronic structure and potentially shifting fluorescence emission to longer wavelengths or increasing intensity. Conversely, at higher pH, proton loss can lead to shifts in emission towards shorter wavelengths or reduced intensity, making carbon dots responsive pH indicators [4].

Impact of Carbon dot and Solvent

The dye center of the functional group is best envisioned as a small particle restricted to an area close to the carbon dot surface. To estimate the environmental impact on the excitation dynamics of the functional group, a three-layer system may be employed. The core of the internal dynamics calculation, see Sec. 2.2, is the separation of the particle and the environment. By considering large carbon dots, we assume the pH
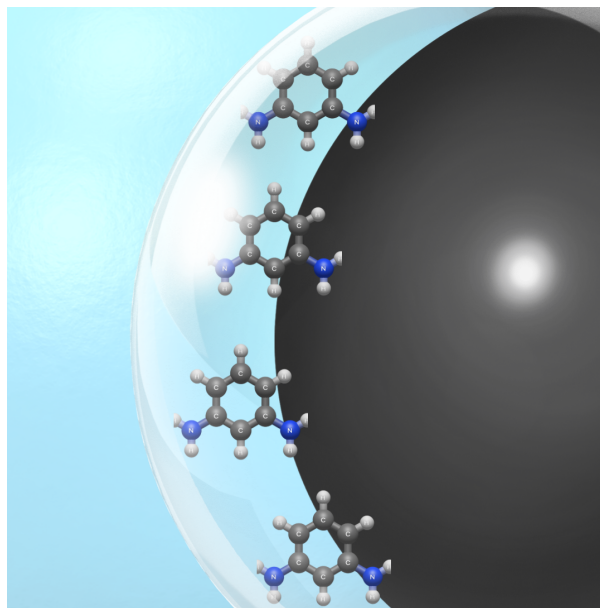
Figure 2.9: Three-layer Carbon Dot System: This Figure shows a carbon dot with m-phenylenediamine dye molecules attached to its surface. The black sphere represents the carbon core, which can be determined using ε_C. The surface molecules are isolated in a simulated vacuum as the carbon dot is enclosed in a liquid environment with a dielectric constant of $varepsilon_W$. Density Functional Theory (DFT) is used to analyse the system analytically in order to take into consideration the surface molecules in a vacuum. We further modify this model to incorporate scattering effects from the surrounding liquid as well as the carbon core.

sensitivity to be determined by the functional groups. Thus, the dye center is represented by the molecular Hamiltonian H_M and the core of the carbon dot together with the surrounding solvent by the field, H_F. Due to Pauli blocking (Ref. [19]), there will be a vacuum layer between the carbon dot's core and the solvent, in which the functional group will be located. Hence, we approximate the surrounding's impact with a three layer system composed of carbon-vacuum-water to determine the state mixing caused by the carbon dot, as illustrated in Figure 2.9.

The electronic transition energies of the isolated surface functional groups can be predicted by using Density Functional Theory (DFT), see Section 2.8.1. We are able to evaluate the effect these interfaces have on the electrical transitions using to this methodology. For larger carbon dots, the deflection of an electromagnetic wave, such as a laser, can be predicted by using the Fresnel reflection at a flat interface between

water and carbon, which yields the scattering Green function [23],

$$\mathbf{G}_{\mathrm{pl}}^{(1)}(\mathbf{r}, \mathbf{r}', \omega) = \frac{i}{8\pi^2} \int \frac{d^2 k^{\|}}{k_1^{\perp}} e^{i\mathbf{k}^{\|} \cdot (\mathbf{r} - \mathbf{r}') + ik_1^{\perp}(z + z')}$$

$$\times \left[r_s \mathbf{e}_{s+}^1 \mathbf{e}_{s-}^1 + r_p \mathbf{e}_{p+}^1 \mathbf{e}_{p-}^1 \right], \tag{2.77}$$

with the Fresnel reflection coefficients r_s and r_p

$$r_s = \frac{k_1^{\perp} - k_2^{\perp}}{k_1^{\perp} + k_2^{\perp}}, \quad r_p = \frac{\varepsilon_2 k_1^{\perp} - \varepsilon_1 k_2^{\perp}}{\varepsilon_2 k_1^{\perp} + \varepsilon_1 k_2^{\perp}}, \tag{2.78}$$

with the wave vector parallel to the plane $\mathbf{k}^{\|} \perp \mathbf{e}_z$ and its component towards z direction $k_j^{\perp} = \sqrt{\varepsilon_j \omega^2 / c^2 - k^{\|2}}$. In a limit where wave properties of light are disregarded (non-retarded limit), the Equation for flat surface scattering can be simplified by considering only its imaginary component and establishing new reflection coefficients that ignore wave properties, based on the electrical characteristics of water and carbon.

$$\mathrm{Im}\, \mathbf{G}_{\mathrm{pl}}^{(1)}(\mathbf{r}, \mathbf{r}, \omega) = \frac{c^2}{32\pi\omega^2 z^3} \mathrm{Im}\, [R(\omega)] \begin{pmatrix} 1 & 0 & 0 \\ 0 & 1 & 0 \\ 0 & 0 & 2 \end{pmatrix}, \tag{2.79}$$

with the multi-scattering reflection coefficient

$$R(\omega) = \frac{r_{\mathrm{W}}(\omega) r_{\mathrm{C}}(\omega) e^{-i\omega l/c}}{1 - r_{\mathrm{W}}(\omega) r_{\mathrm{C}}(\omega) e^{-i\omega l/c}}, \tag{2.80}$$

the thickness of the surrounding vacuum layer l, the non-retarded reflection coefficient

$$r_i(\omega) = \frac{\varepsilon_i(\omega) - 1}{\varepsilon_i(\omega) + 1}, \tag{2.81}$$

for the vacuum-water and vacuum-carbon interface with the dielectric function for water and carbon, ε_{W} and ε_{C}, respectively.

Incorporating the effect of an adjacent liquid, Onsager's real cavity model is applied for local field correction [43, 19]. This model posits that a particle within a medium with a specific permittivity at frequency ω is encased in a spherical void and modifies the reflection coefficient further [19]

$$R^{\star}(\omega) = R(\omega) \left(\frac{3\varepsilon_{\mathrm{W}}(\omega)}{1 + 2\varepsilon_{\mathrm{W}}(\omega)} \right)^2. \tag{2.82}$$

To deduce the transmission rate changes for molecules that either accept or release protons near the carbon dot, one combines the vacuum transmission rate (2.37) with

the medium-altered transmission rates (2.29), by summing the free space rate and the medium-assisted rate, leading to

$$\Gamma_{HD/D} = \Gamma_{fs}^{HD/D} + \Gamma_{ma}^{HD/D} , \tag{2.83}$$

with

$$\Gamma_{fs}^{HD/D} = \frac{\omega_{HD/D}^3 |\boldsymbol{d}_{HD/D}|^2}{3\hbar\pi\varepsilon_0 c^3} , \tag{2.84}$$

$$\Gamma_{ma}^{HD/D} = \frac{1}{2\pi\hbar\varepsilon_0 l_{HD/D}^3} \mathrm{Im}\left[\left(\frac{3\varepsilon_W(\omega_{HD/D})}{1 + 2\varepsilon_W(\omega_{HD/D})}\right)^2\right.$$

$$\times \frac{r_W(\omega_{HD/D})r_C(\omega_{HD/D})e^{-i\omega_{HD/D}l_{HD/D}/c}}{1 - r_W(\omega_{HD/D})r_C(\omega_{HD/D})e^{-i\omega_{HD/D}l_{HD/D}/c}}\Big]$$

$$\times \left([d_{HD/D}^x]^2 + [d_{HD/D}^y]^2 + 2[d_{HD/D}^z]^2\right) , \tag{2.85}$$

where we located the centre of the transition in the centre of the dye molecule $z = l_{HD/D}/2$.

2.8 Quantumchemical calculations

This chapter delves deeper into the topic of quantum chemical calculations, building on a theoretical and foundational understanding of the physical properties of carbon dots, such as their sensitivity to pH and a detailed investigation of the fluorescence lifetime mechanism we intend to replicate. These calculations, which are essential for figuring out all the frequencies of excited states and transition dipole moments in various dye molecules, will be performed using the NWChem programme. This section provides the basic theory for a more computational approach by connecting theoretical concepts to practical modelling and analysis applications.

2.8.1 Density Functional Theory (DFT)

Density functional theory (DFT) is used to calculate the electronic structure of atoms, molecules and materials. By defining the system in terms of the ground state electron density instead of the wave function, density functional theory provides an effective method for calculating the electronic density and energy of a system. First, we want

to take a deeper look at more conventional wave-function based techniques, like the Hartree-Fock (HF) method, [44]. The HF (Hartree-Fock) method approximates the N-body wavefunction using a single Slater determinant composed of N spin-orbitals. The Slater determinant is a mathematical construct designed to ensure the antisymmetry of the wavefunction, necessary for fermionic particles like electrons. It adheres to the Pauli exclusion principle by automatically changing sign upon the exchange of any two electrons. This property reflects the fundamental behavior of electrons where no two electrons in an atom can have the same set of quantum numbers. It derives a set of equations for atomic orbitals using the variational principle, leading to the Hartree-Fock wavefunctions and energies. However, the HF method does not account for electron correlation-the interactions among electron movements that the mean-field approximation overlooks. This oversight affects the accuracy of predictions regarding the electronic structure and properties of molecules, as electron correlation plays a crucial role in the chemical behavior of complex systems. It is now primarily used as a starting point for more advanced post-HF approaches, like coupled cluster or configuration interaction methods (Ref. [44]), which recover the missing correlation and approximate the exact wavefunction. "Coupled" refers to the way these methods account for the interaction between different electron configurations, while "configuration interaction" means systematically combining various electronic configurations (different ways electrons can be distributed among the molecular orbitals) to achieve a more accurate approximation of the molecule's wavefunction, thereby capturing the effects of electron correlation [44]. DFT aims to tackle both the inaccuracies of HF and the computational complexity of post-HF methods by substituting the many-body electronic wavefunction with the electronic density as the fundamental quantity.

The mathematical fundament of DFT lies in the Hohenberg-Kohn theorems, which provide the basis for connecting the electron density to the ground state properties of a system.

- **Hohenberg-Kohn's First Theorem** states that the ground state electron-density uniquely determines the external potential within which the electrons are confined.

- **Hohenberg-Kohn's Second Theorem** states that the total energy of a system can

be expressed as a functional of the electron density. The functional takes the form $E[n]$, where E is the total energy and $n(\mathbf{r})$ is the electron density.

- To practically solve the DFT equations, the Kohn-Sham scheme introduces a set of auxiliary non-interacting electrons that reproduce the same electron density as the true interacting system. **Kohn-Sham equations** are a set of self-consistent equations that determine the wavefunctions and energies of these auxiliary electrons.

- The final ingredient in DFT is **the exchange-correlation functional**, which accounts for the effects of electron-electron interactions beyond the classical electron-electron repulsion. This functional is typically approximated using various schemes, such as local density approximation (LDA) or generalized gradient approximation (GGA), which will be explained later on.

To derive the Hohenberg-Kohn Theorems, we first have a look at the stationary Schrödinger equation.

The stationary Schrödinger equation describes the behaviour of electrons in a system with a given potential. It is solved by a collection of wave functions ψ_n and their corresponding energies E_n, forming an infinite set, to describe a molecular system

$$\hat{H}\psi_n = E_n\psi_n, \tag{2.86}$$

with the Hamiltonian

$$\hat{H} = \hat{T}_c + \hat{T}_e + \hat{V}_{ee} + \hat{V}_{cc} + \hat{V}_{ec}, \tag{2.87}$$

where $\hat{T}_c$ describes the kinetic energy of the cores and $\hat{T}_e$ of the electrons. The interaction potential separates into the interaction between electrons $\hat{V}_{ee}$, the cores $\hat{V}_{cc}$ and between cores and electrons $\hat{V}_{ec}$. A challenge with this equation is, that a $3n$-dimensional space is used to describe the wavefunctions. Hence, as the size of the system increases, the complexity of the problem escalates, leading to a proportional growth in computational time.

Instead of dealing with the individual wave functions, DFT focuses on the electron density $n(\mathbf{r})$, which provides the probability density for finding an electron at a particular position $\mathbf{r}$. With this approach, it is possible to reduce the problem to a 3 dimensional one, so the complexity decreases.

We start with minimizing a system's energy to find the ground-state energy

$$\hat{H}\psi_0 = E_0\psi_0, \tag{2.88}$$

by minimizing the expectation value

$$E_0 = \min_n \langle \psi_n | \hat{H} | \psi_n \rangle. \tag{2.89}$$

In DFT, we minimize the expectation value in sense of an integral over all space using V_{CC} since ion charts are positive and interact favorably with $n(\mathbf{r})$ and since $n(\mathbf{r})$ is continuous through space we have to integrate over all space

$$E = \min_n \left\{ \int V_{CC}(\mathbf{r})n(\mathbf{r}) \, d^3r + F[n(\mathbf{r})] \right\}. \tag{2.90}$$

The combination of the kinetic and potential energies required to characterise the system is contained in some universal functional $F[n(\mathbf{r})]$ of the density, as demonstrated by Hohenberg and Kohn. The function that has the lowest energy-output is the one that uses the exact density of the system [45]. The expression for this functional is unknown and therefore the challenge remains to minimize the energy of the system. Therefore Hohenberg and Kohn started separating the energy functional into a known part and an unknown exchange-correlation part (XC), including all correlations and exchange interactions between electrons and the nuclei as well as all quantum mechanical properties

$$E[\{\psi_i\}] = E_{known}[\{\psi_i\}] + E_{XC}[\{\psi_i\}]. \tag{2.91}$$

We move from the many-body Schrödinger equation to a many single-electron Kohn-Sham equations

$$\hat{H}\psi(\mathbf{r_1}, ..., \mathbf{r_N}) = E\psi(\mathbf{r_1}, ..., \mathbf{r_N}) \Rightarrow \hat{H}_{KS}\varphi(\mathbf{r_1})\varphi(\mathbf{r_2})...\varphi(\mathbf{r_N}) = E\varphi(\mathbf{r_1})\varphi(\mathbf{r_2})...\varphi(\mathbf{r_N}). \tag{2.92}$$

To improve the accuracy of DFT, the Kohn-Sham equations are introduced as they allow to calculate the ground state properties of a system in a computational feasible manner, simplifying the many-electron problem by mapping it onto a set of non-interacting electrons [46]. The theory's derivation will be covered in detail in the appendix, beginning with the Hohenberg-Kohn theorems' proof.

Kohn-Sham equations

The Kohn-Sham equations are going to help us to replace the complex interacting many-body system with a different auxiliary system that is easier to solve. We switch to many-single electron equations from the many-body Schrödinger equation. The approach assumes that the ground-state energy of the originally interacting system determined by the electron density $n_0(\mathbf{r})$ corresponds to the new chosen system. All the complex interacting many-body terms are described using the exchange correlation functional $E_{XC}[\{\psi_i\}]$ of the density

$$E[\{\psi_i\}] = E_{known}[\{\psi_i\}] + E_{XC}[\{\psi_i\}]. \tag{2.93}$$

As mentioned above, the system is described by many single electrons

$$\hat{H}_{KS}\phi(\mathbf{r}) = E\phi(\mathbf{r}). \tag{2.94}$$

We can decouple the dynamics of ions and electrons using the Born-Oppenheimer's approximation, which assumes that ions are fixed in space, because they are heavier than electrons and therefore move slower, creating an external potential V_{ex} that is influencing the electrons. The system may now be explained as follows, where the locations of the electrons and ions are defined by $\{r_i\}, \{R_i\}$

$$\begin{aligned}
\hat{H}_{\mathrm{BO}}(\{r_i\}, \{R_j\}) &= \hat{T}_{ee} + \hat{V}_{ee} + \hat{V}_{ei} + \hat{V}_{ii} \\
&= \sum_{i=1}^{n} \frac{\nabla_i^2}{2m_e} + \sum_{i<j} \frac{e^2}{|r_i - r_j|} + \sum_{i=1}^{n} V_{\mathrm{ext}}(r_i, \{R_j\}).
\end{aligned} \tag{2.95}$$

The kinetic energy of the ions T_{ii} and the ion-ion potential V_{ii} separate du to Born-Oppenheimers approximation. Both kinetic and potential energy of the electron-electron interaction are independent of the type of the system, thus, we only need to have a closer look to the external potential $V_{ext}(r_i, \{R_i\})$. This term is inherently a function

of three dimensions, contrasting with the wave function, which depends on 3n variables. So, we have already achieved a reduction of the problem to only 3 dimensions. Considering the Hohenberg-Kohn theorems, we leverage the ground-state electron-density $n_0(\boldsymbol{r})$ to construct a Hamiltonian. This Hamiltonian enables us to derive the wave function in a $3n$-dimensional space and determine the energy of our system. With this fundamental knowledge in hand, we can then access and examine the different properties of the system or material under investigation. From Hohenburg-Kohns second theorem, we know that there is a ground-state energy that minimizes the energy of the overall functional being the true ground-state electron-density. The challenge remains to find a solution to this functional. Kohn-Sham uses the approach to expand the energy functional in the form

$$E[n] = T_{sp}[n] + U_H[n] + V_{ext}[n] + V_{XC}[n], \tag{2.96}$$

where $T_{sp}[n]$ is the kinetic energy, $U_H[n]$ the electron-electron interaction, also known as Hartree term, the ion-electon interaction is described with $V_{ext}[n]$ and the exchange correlation energy with $V_{XC}[n]$. Details can be found in chapter 7 in [47].

Exchange and Correlation functional

The contributions of exchange and correlation to the total energy are captured by the exchange and correlation functional, which is a complete function of the electron density. Two main exchange-correlation functionals are commonly used in modern DFT calculations.

The initial functional is the Local Density Approximation (LDA). As an integral across space of a function dependent only on the local density at that specific place, this exchange-correlation functional is effectively a zeroth-order momentum. LDA addresses exchange and correlation through two distinct terms: the exchange term and the correlation term. For the exchange term, which constitutes an exact equation for a homogeneous non-interacting electron gas, an analytical solution is available. In the case of homogeneous systems, the exchange energy can be expressed as

$$E_{XC}^{Hom}(n(\boldsymbol{r})) = -\frac{3q^2}{4}\left(\frac{3}{\pi}\right)^{\frac{1}{3}} n(\boldsymbol{r})^{\frac{4}{3}}, \tag{2.97}$$

which translates into the LDA exchange energy

$$E_{XC}^{LDA}[n(\boldsymbol{r})] = -\frac{3q^2}{4}\left(\frac{3}{\pi}\right)^{\frac{1}{3}}\int d^3r n(\boldsymbol{r})^{\frac{4}{3}}. \tag{2.98}$$

The assumption is that the exchange part of the exchange-correlation potential is an integral over the entire space of the local density at that specific point. This is valid for a uniform gas with no gradients, suggesting that gradients and density fluctuations are ignored, especially in systems where spatial fluctuations in the electron density are important. This exchange-correlation approach works well as long as the density does not change greatly in space. Even for the homogeneous gas, Monte Carlo simulations may produce numerical values for this correlation that can be used in DFT calculations, even though there is no analytical solution for the correlational part. Random sampling is used in these simulations to simulate complex system behaviour. LDA has limitations in terms of energies, even though it can properly predict geometries. This is because discrepancies can arise when exchange-correlation effects are not fully captured, particularly in systems with large correlation effects. Efforts are made to enhance functionality by introducing dependence on the local density gradient, leading to the Generalized Gradient Approximation (GGA).

GGA incorporates both the density and its gradient in its considerations. Together with a term that takes into account the density gradient, the exchange and correlation functional is expressed as an integral over space of a function that is dependent on the local density. Beyond the local density, this gradient term provides additional information by capturing spatial fluctuations in the electron density. This can be written as

$$E_{XC}^{GGA}[n(\boldsymbol{r})] = \int d^3r E_{XC}^{GGA}[n(\boldsymbol{r}), \nabla n(\boldsymbol{r})]. \tag{2.99}$$

Gradient corrections, denoted as $\nabla n(\boldsymbol{r})$, account for variations in density, making these functionals more accurate than LDA, particularly in scenarios involving larger variations in electron density, such as defects [45]. Various parameterizations exist, with the PBE (Perdew, Burke, Ernzerhof) [48] being the most popular, alongside others like BLYP (Becke's exchange + Lee Yang and Parr) or B3LYP [49] (a hybrid of 30 percent exact exchange and GGA). While using B3LYP in DFT calculations improves accuracy, it is important to note the higher computational cost associated with incorporating the exact exchange of HF theory. In this thesis, we use the B3LYP functional during the
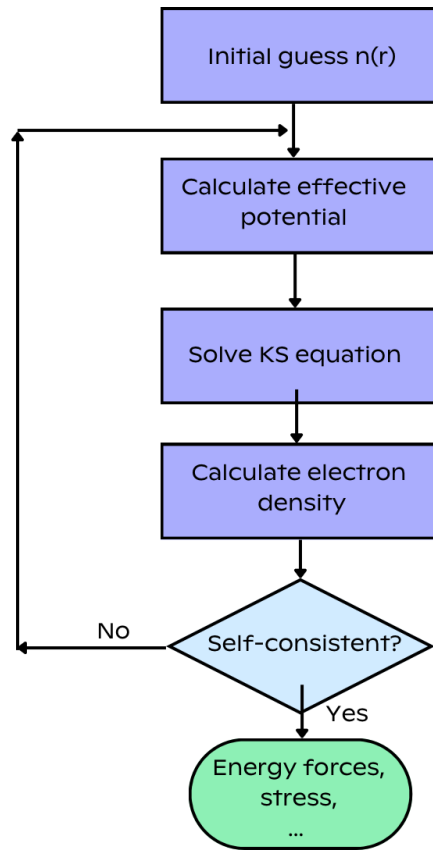
Figure 2.10: A visual depiction of the iterative process involved in solving the Kohn–Sham equations is presented schematically. Typically, this process requires the simultaneous iteration of two loops—one for each spin. The potential for each spin is determined as a functional outcome of the combined density of both spins. Adapted from [47].

DFT calculations

$$E_{XC} = E_{XC}^{LDA} + a_0(E_x^{HF} - E_x^{DFA}) + a_x E_x^{Becke} + a_c E_c,\qquad(2.100)$$

where E_x^{DFA} denotes and LDA or GGA functional, and the coefficient a_0, a_x, a_c are empirically adjusted to fit atomic and molecular data.

Summary

Figure 2.10 summarizes the DFT simulation.

We first make an initial guess on the electron density and then calculate the effective potential using Equation (2.96)

$$V_{eff}(\mathbf{r}) = U_H[n(\mathbf{r})] + V_{ext}(\mathbf{r}) + V_{XC}[n(\mathbf{r})].\qquad(2.101)$$

Upon incorporation into the Kohn-Sham equation (see Equation (2.95)) and subsequent solution, the resulting electron density is obtained. This density serves as the foundation for determining various properties, including electron energies, forces, and stresses. If the derived electron density does not align with the initial guess, the iterative process continues until convergence is achieved.

2.8.2 Time-dependent density functional theory (TD-DFT)

The ground state, or lowest energy state, of a molecule is the main task that is modelled using DFT. DFT is essentially an effective technique for ground-state modelling, but for a more thorough understanding of a molecule's behavior—especially when taking excited states into account—a variety of approaches may be used.

It is crucial to model both the excited and ground states of a molecule's energy in order to simulate the fluorescence process. We are examining the time evolution of a photon as it relaxes from the excited state back to the ground state using fluorescence lifetime. As a result, we must also apply time-dependent DFT (TDDFT), in addition to DFT. Under certain condition it is possible to establish a one to one correspondence between time-dependent densities $n(\boldsymbol{r}, t)$ and time-independent one-body potentials $V_{ext}(\boldsymbol{r}, t)$ for a given initial state. Instead of the Hohenburg-Kohn theorem we can use its time dependent analog, the Runge-Gross theorem.

Runge-Gross theorem

The goal of the Runge-Gross theorem is to demonstrate the basic principle that variations in a quantum system's external potential have a distinct and particular impact on the electron density's temporal evolution and, in turn, on observable variables such as the time-dependent current density. The core of the TDDFT theoretical framework is this theorem. We examine a system of N non-relativistic electrons that interact with one another through the Coloumb repulsion within a time-varying external potential. Two potentials $V(x)$ and $V'(x)$ affect two densities from a shared initial state $\psi_0 = \psi(t = 0)$, $n(x)$ and $n'(x)$ can vary. The potentials always differ by more than a purely time-dependent function

$$\nabla V_{ext}(x) = V(x) - V'(x) \neq c(t). \tag{2.102}$$

The difference in the potential allows a one-to one mapping between the densities and the potentials and a density functional theory can be constructed.

Kohn-Sham equations for TDDFT

The Hohenberg-Kohn theorems' methodology and that of Kohn-Sham equations are similar in the setting of TDDFT. A hypothetical assembly of non-interacting electrons that satisfies the time-dependent Kohn-Sham equations is used to describe the system

$$i\frac{\partial \phi_j(\boldsymbol{r},t)}{\partial t} = \left(-\frac{\nabla^2}{2} + V_s[n](\boldsymbol{r},t) \right) \phi_j(\boldsymbol{r},t), \tag{2.103}$$

with density

$$n(\boldsymbol{r}) = \sum_{j=1}^{N} |\phi_j(\boldsymbol{r})|^2. \tag{2.104}$$

Equation (2.101) illustrates our newly developed exchange-correlation potential, which follows the traditional Hartree potential structure. This formulation is modified for a time-varying density

$$V_s(\boldsymbol{r}) = V_{ext}(\boldsymbol{r}) + U_H(\boldsymbol{r}) + V_{XC}(\boldsymbol{r}). \tag{2.105}$$

So, the exact exchange correlation potential can be written as

$$V_{XC}[n; \psi(0), \phi(0)](\boldsymbol{r},t) = V_s[n; \phi(0)](\boldsymbol{r},t) - U_H[n](\boldsymbol{r},t) - V_{ext}[n; \psi(0)](\boldsymbol{r},t). \tag{2.106}$$

The entire temporal development of the density, $n(\boldsymbol{r})$, the initial interacting wavefunction, $\Psi(0)$, and the initial Kohn-Sham wavefunction, $\Phi(0)$, is closely linked to the exchange-correlation potential.This functional is strongly entangled; it is more complex than in the ground-state case. The adiabatic approximation, which assumes that the exchange-correlation potential depends simultaneously on the current density immediately, is a key assumption that is frequently used in TDDFT in practice. This simplification makes the time-dependent Kohn-Sham equations easier to solve. Detailed computations and other references to this approximation are available in reference [45], chapter 22.

2.8.3   Choice of Basis set and Functional for Quantumchemical calculations

For both DFT and TDDFT calculations, the semi-empirical Hybrid functional B3LYP has been chosen. B3LYP is known for its good balance between accuracy and computational cost for a wide range of applications and molecule types and it can be applied to a vast array of molecular systems. There is a vast literature of benchmark studies (e.g. [50]) and applications of B3LYP making it easier to justify its use and compare results.

Our three precursor molecules range from relatively simple to more complex organic structures, therefore B3LYP is well-suited for dealing with such a range [51]. All three molecules are organic and B3LYP has been extensively benchmarked for organic molecules and is known to provide reliable geometries and energies for such systems [51, 50, 52]. In general, B3LYP is a popular choice for the study of electronic properties, and excited states in TD-DFT as it is known that it gives a good account of the electronic distribution. The choice of B3LYP is guided by its proven efficacy for organic compounds the type of calculations being performed and the nature of the molecules.

For all calculations, the def2-TZVP basis set [53] has been used. It is a basis set developed as a second generation of default basis set for the TURBOMOLE program (therefore def2) and TZV denotes valence triple zeta and P denotes polarized P type basis sets are recommended for the DFT calculations (ref). The TZVP means that it provides a high level of accuracy in describing electron distribution by including three sets of basis functions for each valence shell and the polarization function is essential for an accurate description of molecular geometry, electronic states and properties. def2-TZVP is an efficient basis set that can be used for a wide variety of molecules and it has a good balance between computational cost and accuracy [53]

For our molecules the basis set is a good choice because for geometry optimization, def2-TZVP can include electron delocalisation through the polarization functions which is important as the molecules we observe all have a system of delocalized π-electrons / aromatic rings and functional groups attached to the aromatic ring which can influence how electrons are distributed around the aromatic ring and also influence if the molecule is electron donating or electron accepting (deprotonated/protonated). In terms of TD-DFT for calculating transition energies and dipole moments for

the dye molecules def2-TZVP can accuratley describe the electronic states involved in transitions due to the triple-zeta component which has a high orbital detail. The P function can model asymmetric electron distributions and polarization effects accurately [53]. The choice of functional and basis set was made due to its balance between computational cost and accuracy.

2.8.4 NWChem

The software platform used in this thesis to perform Density Functional Theory (DFT) computations is NWChem [54]. NWChem is well-known for its adaptable computational chemistry capabilities and is compatible with a wide range of computing systems. Both excited and ground states can be studied using NWChem due to its seamless transition from quantum to classical approaches. Additionally, it provides versatility by supporting both plane waves and Gaussian basis functions. Since NWChem also supports relativistic effects and features, it is a solid choice for a variety of research applications.

This thesis utilizes the software to conduct geometry optimizations for the protonated and deprotonated dye molecules m-phenylenediamine, phloroglucinol and disperseblue1 dye. Additionally, TD-DFT calculations with NWChem are employed to compute transition frequencies and transition dipole moments for single excited states.

Transition Dipole Moment Calculations with NWChem

To calculate the transition dipole moments of different precursor molecules using NWChem, the following steps have been performed:

Geometry Optimization

The molecular geometry of each molecule was initially created using Avogadro2 (Ref. [55]). The structure data was then exported and saved as an XYZ file, which was later loaded into the NWChem input file for further processing. Following the NWChem documentation, the molecular geometry was optimized using the def2-SVP library and DFT with the B3LYP functional

```
1  echo #Display information or print messages during execution
2  start h2o #Specify the name of the job or calculation
```

```
 3 title "h2o geometry optimization" #Provide a title or description
       for the job
 4 geometry #Define the molecular geometry of the system
 5     load wasser_geometry.xyz #Load molecular coordinates from the
         file
 6 end #End of the geometry block
 7 basis #Specify the basis set for the calculation
 8     * library def2-SVP #Apply the "def2-SVP" basis set to all
         atoms
 9 end #End of the basis block
10 dft #Specify details of the DFT calculation
11     xc b3lyp #Set the exchange-correlation functional to B3LYP
12 end #End of the DFT block
13 DRIVER #Specify details about the driver module
14     XYZ #Optimization in cartesian coordinates
15     MAXITER 200 #Set the maximum number of optimization
         iterations to 200
16 END #End of the DRIVER block
17 task dft optimize #Specify the type of calculation
```

The output is a newly optimized geometry XYZ file for further calculations.

TDDFT Calculations

The optimized geometry file obtained previously is used for TDDFT calculations in NWChem. The input file for this calculation is:

```
 1 echo #Display information or print messages during the execution.
 2 start h2o #Specify the name of the job or calculation
 3 title "h2o TDDFT excited states" #Provide a title or description
     for the job
 4 geometry #Define the molecular geometry of the system
 5     load h2o-geo-opt.xyz #Load molecular coordinates from the
         file "h2o-geo-opt.xyz."
 6 end #End of the geometry block
 7 basis #Specify the basis set for the calculation
 8     * library def2-SVP #Apply the "def2-SVP" basis set to all
         atoms
 9 end #End of the basis block
10 dft #Specify details of the DFT calculation
11     xc b3lyp #Set the exchange-correlation functional to B3LYP
12 end #End of the DFT block
13 tddft #Specify details of the TDDFT calculation
14     nroots 50 #Set the number of roots (excited states) to 50
15 end #End of the TDDFT block
16 task tddft energy #Specify the type of calculation
```

2.9   Precursor Molecules

The Carbon dots we are interested to investigate in this thesis are synthesized according to [4]. Calculations were performed on three distinct precursor molecules: m-phenylenediamine (mPD)(figure 2.11), phloroglucinol (figure 2.12), and disperseblue1 dye (figure 2.13), each in both its deprotonated and protonated forms.
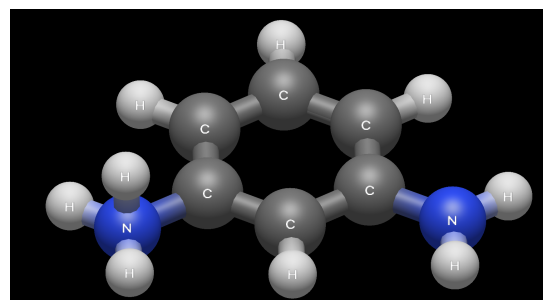
m-phenylenediamine

The chemical molecule known as m-Phenylenediamine, or mPD for short, is also known as 1,3-diaminobenzene, an illustrated in its protonated and deprotonated state in figure 2.11. Its molecular formula is $C_6H_8N_2$. The benzene ring in this molecule has two amine groups ($-NH_2$) linked to it at the meta locations. These amino groups are important because of their ability to donate electrons, which greatly raises the electron density surrounding the benzene ring. The highest energy orbital that has electrons under normal circumstances is referred to as the "highest occupied molecular orbital" (HOMO) in the context of molecular orbital theory. Conversely, the lowest energy orbital that is open to the possibility of accepting electrons is known as the LUMO (Lowest Unoccupied Molecular Orbital). Because it affects how a molecule interacts with light and other molecules, the energy difference between the LUMO and HOMO is important because it affects a molecule's chemical reactivity and characteristics. Because the molecule returns to its ground state more quickly, such a drop may lead to shorter excitation durations. Furthermore, the configuration of the amine groups promotes hydrogen bonding, which affects its chemical reactivity and physical characteristics.

Phloroglucinol

Phloroglucinol is a molecule with the chemical formula $C_6H_6O_3$. It is based on a benzene ring that has three symmetrically linked hydroxyl groups. This symmetrical arrangement increases the electron density around the benzene ring. Because they donate electrons, the hydroxyl groups contribute in the increase in electron density.
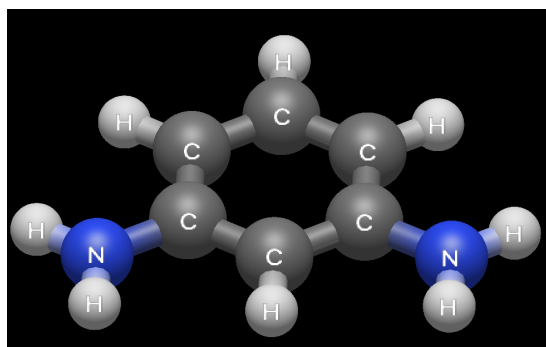
(a) Deprotonated m-phenylenediamine with a total charge of 0.

(b) Protonated m-phenylenediamine with a charge of +1, one H atom was added.

Figure 2.11: Comparison of deprotonated and protonated m-phenylenediamine.
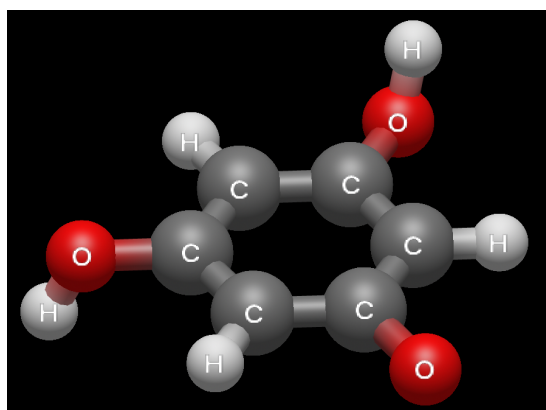
(a) Deprotonated phloroglucinol with a total charge of -1, one H atom was removed.
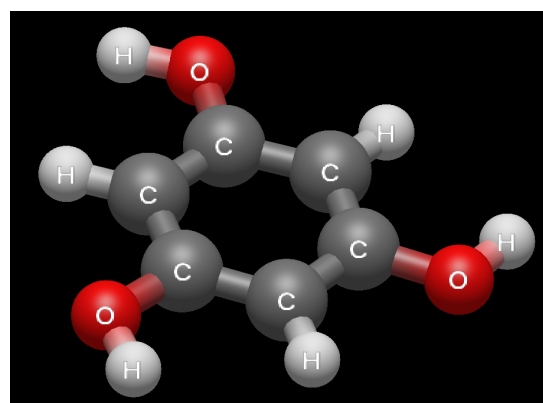
(b) Protonated phloroglucinol with a charge of 0

Figure 2.12: Comparison of deprotonated and protonated phloroglucinol.

Disperse-blue 1 dye

A nitro group ($-NO_2$) and an ethylamino group ($-NH(C_2H_5)$) are added to one benzene ring in Disperse Blue 1, illustrated in figure 2.13, also known chemically as 4-(ethylamino)-4'-nitroazobenzene. The nitro group acts as an electron acceptor and the ethylamino group as an electron donor in this structure, which represents a traditional push-pull situation. The main component in regulating this interaction is the azo group (N=N) connecting the two benzene rings. The molecule's electronic energy levels are significantly influenced by the differential donation and withdrawal of electrons, which affects the dye's colour and light absorption capabilities. Disperse Blue 1 is a useful chemical in textile applications because of the way substituents interact to define its optical and dyeing properties. The electron structure is more related to the

benzene ring, the more double bonds we have connected to it the smaller the bandgap is, the more accessible excitation we have.
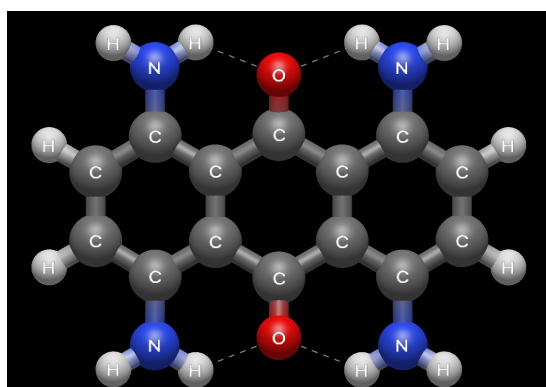
(a) Deprotonated disperse-blue1 with a total charge of 0.
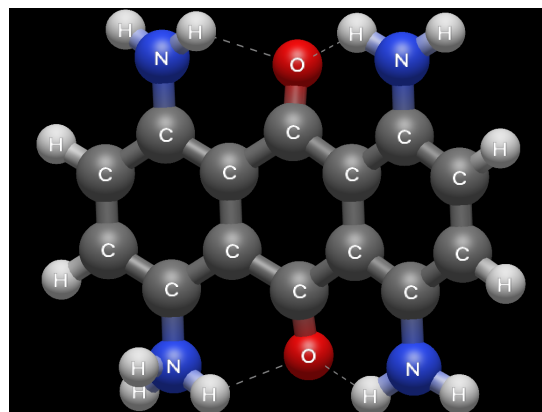
(b) Protonated disperse-blue 1 with a charge of +1, one H atom was added.

Figure 2.13: Comparison of deprotonated and protonated disperse-blue1.

Approach

We'll investigate the excitation lifetimes of the precursor molecules in a protonated and deprotonated state under varying pH in presence of a carbon surface and surrounded by water with our model. In the work of W. Szapoczka [4], five different carbon dots have been synthesized and their fluorescence lifetime has been investigated under varying pH. The results are shown in figure 2.14.

CD01 and CD02 are synthesized using 0.3 g of disperse blue 1 dye and 0.7 g of phloroglucinol, while CD03 consists of 0.3 g of disperse blue 1 dye, 0.4 g of citric acid, and 0.1 g of ammonium fluoride. CD04 is synthesized solely with 1 g of mPD, whereas CD05 is prepared with a combination of 1 g of mPD and 1 g of phloroglucinol [4]. Notably, only CD04 is composed of a single type of dye molecule, mPD, while the other carbon dots are synthesized using mixtures of different precursor molecules. It should be emphasized that this thesis focuses solely on observing the fluorescence lifetime of the pure dye molecules without mixing.
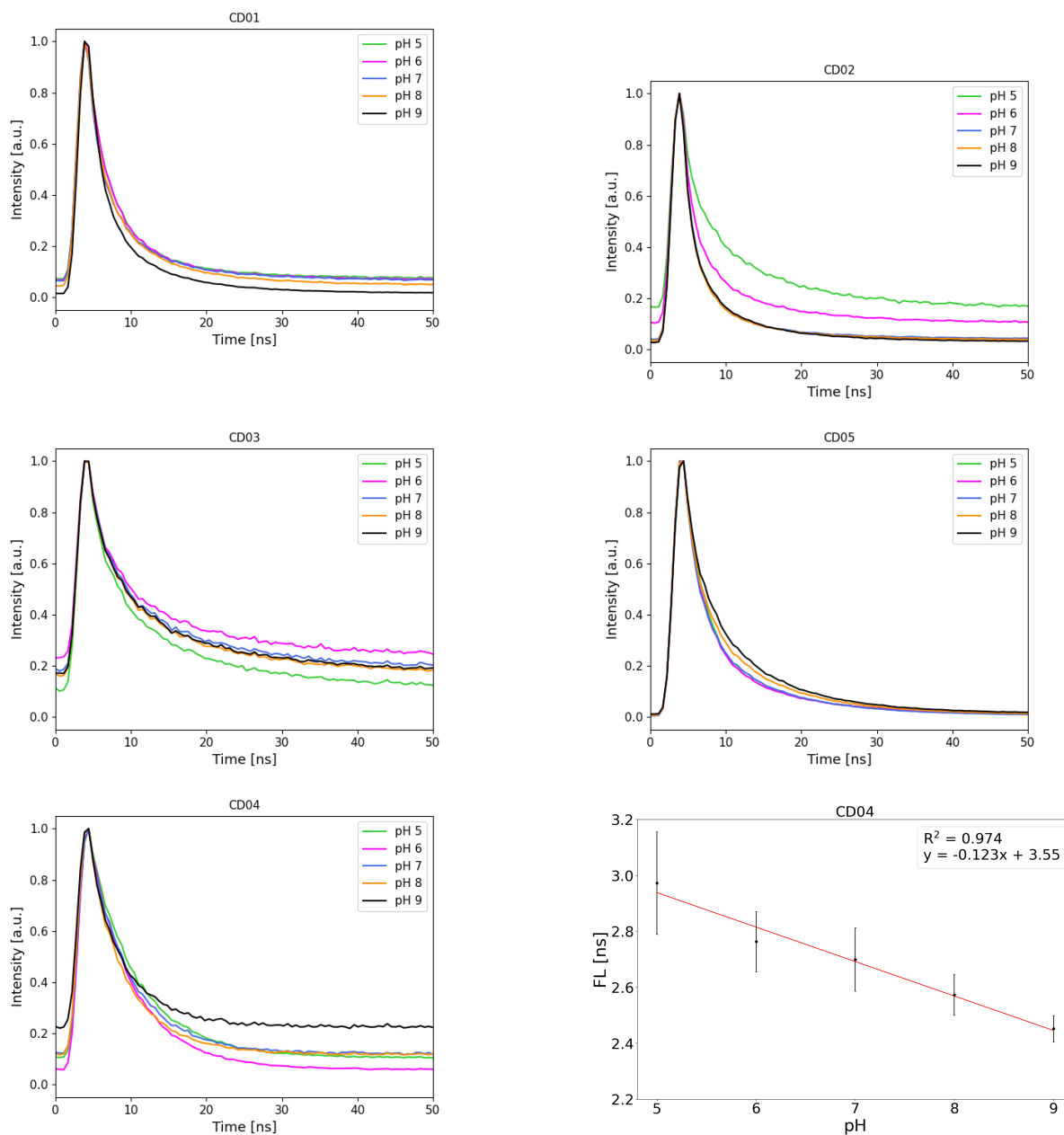
Figure 2.14: The time-resolved fluorescence decay of the five CDs ($0.02 mg\dot{m}L^{-1}$) dissolved in $100 mM$ Carmody buffer solution adjusted to pH $5 - 9$. CD04 is the only sample using only m-phenylenediamine as a surface functional group, the calculated fluorescence lifetime is illustrated as a function of pH in subfigure **(f)**. The standard error of the slope is 0.0116.

2.10   The Overall Model

The model introduced in this thesis is based on fundamentals of macroscopic Quantum Electrodynamics. To calculate the fluorescence lifetime in free-space the transition rate between single excited states is calculated in Section 2.2. An important assumption has been made by evaluating this, the quasi-degenerate states of the atom have been neglected. Quasi-degeneracy means that two ore more energy levels of a system are close in value but not equal. This can result in similar properties and behaviours for states that are quasi-degenerate. In a perfect degenerate system two or more states have exactly the same energy and small perturbations can mix these states, whereas in a quasi-degenerate system they are slightly different but can still interact strongly with each other when perturbed. This is important in physical contexts such as molecular vibrations, electronic states, solid state phyics and quantumchemical calculations. If two states are quasi-degenerate, it is possible for transitions to occur between them more readily due to resonance effects.

This could affect the rates of radiative transitions. In this model to simplify the calculations we introduced non quasi-degeneracy. We might miss significant coupling between states that could affect their transition probabilities as well as this may lead to incorrect predicitons of energy levels and thus transition energies.

Another fact to take into account is that we might miss resonance effects where the transition rate can be greatly enhanced, which can have an impact on the absorption and emission spectra of the atom. With density functionals theory (DFT) and time-dependend DFT, introduced in Section 2.8.1 and 2.8.2 the transition frequencies and transition dipole moments can be calculated for each precursor molecule in vacuum. As we want to observe the pH sensitive fluorescence lifetime of the molecules, the protonated and deprotonated forms of each molecule have been calculated.

To correct the free-space transition rates with respect to impacts of the carbon dot and solvent on the surface functional groups, more approximations have been introduced in Section 2.6.2. A three layer model has been introduced, considering the surface functional group is a point particle attached in a distance z to a planar carbon surface, surrounded by a vacuum bubble in water. A local-field correction has been made with Onsagers' theory to model the CD in a solution and a vacuum layer around the entire CD and the thickness of the layer was included and calculated with the

COSMO solvation model (Ref. [56]) in NWChem. The model considers the carbon dot to be very small. In addition we assume, that the surface functional group is isolated from the carbon surface to simplify the model. With these approximations, we can introduce Γ_{ma} to deduce the transition rate and include effects from carbon and water and calculate a total transition rate.

The pH response of the carbon dot an the transition rate is modeled as a linear combination of the fraction of deprotonated and protonated molecules at certain pH, using Henderson-Hasselbalchs' Equation (2.7.3) between protonated and deprotonated molecules. We assume the rates to be linear, as the volume fractions are small.

The transition dipole moments (d) and transition frequencies (ω) between excited states are calculated using TD-DFT. However, a limitation of TD-DFT is to take coupling with vibrational states into account. For a thorough understanding of the excitation and fluorescence lifetime processes, vibrational relaxations are essential, as explained in Section 2.1 and illustrated in Figure 2.1. Due to this omission, TD-DFT is only able to predict transitions from the first excited state to the ground state, not accounting for energy loss during vibrational relaxation.

Chapter 3

pH-dependent Excitation Lifetimes of Functional Groups

In this chapter, the model is applied to determine the excitation lifetimes of the surface functional groups under pH sensitivity. The results are analysed an discussed at the end of each section.

3.1 Data handling for Fluorescence Lifetime calculation

After performing DFT and TDDFT calculations for each protonated / deptrotonated precursor molecule, the output Data can be used to calculate the lifetime between the different states within the molecule.

NWChem generated output files include a lot of information, but for the fluorescence lifetime calculation, we are only interested in data such as the transition dipole moment d_{nm} and the transition frequency ω_{nm}. The data can be extracted from the output file with the python code B.3. The file with the sorted data can be used to calculate the fluorescence lifetime using Equation (2.38). The equation has been accordingly implemented in the code B.4. The line width Γ as well as the imaginary part of the Greens function are implemented in a separate python code and calculated according to Equation (2.37).

3.2   Analysis of the Dye Molecules

The computational results obtained with NWChem are presented in this chapter to-
gether with theoretical results calculated for the transition rates of protonated and
deprotonated dye molecules in free-space (fs) and medium-assisted (ma) space. In
addition, we investigate the fluorescence lifetime of the first singlet excitation consid-
ering the molecules' sensitivity to pH.

3.2.1   Results of the Quantumchemical Calculations

All DFT and TD-DFT calculations were performed using NWChem software [54] with
the def2-TZVP basis set and the B3LYP functional, targeting the first five singlet ex-
cited states relative to the ground state. Results, including transition frequencies ($\omega_{0n'}$)
and absolute values of transition dipole moments ($|d_{0n'}|$), are detailed in Table 3.1 and
visualized in Figure 3.1 for disperse-blue 1. This visualization aids in comparing pro-
tonated and deprotonated states for each molecule, with protonated results shown in
purple and deprotonated in green. For m-phenylenediamine (Figure 3.1 a), transi-
tion frequencies increase with the energy gap between excited states. Notably, depro-
tonated states generally show lower frequencies than their protonated counterparts.
The dipole moments do not follow a clear trend, exhibiting variations across different
transitions and protonation states.

Phloroglucinol shows a similar trend in increasing transition frequencies (Figure
3.1 b). Protonated states again exhibit higher frequencies, reflecting changes in elec-
tronic structures due to protonation, which influences electron density and energy
levels.

For disperse-blue 1 (Figure 3.1 c), both protonated and deprotonated forms show
increased frequencies with higher excited states, a pattern expected from larger en-
ergy separations from the ground state. The transition dipole moments, however, do
not display a consistent pattern, suggesting complex interactions within the electronic
states.

These observations highlight the impact of protonation on molecular electronic
structure, significantly altering transition frequencies and affecting the transition dipole
moments. The dipole moment variety throughout states and molecules highlights the

intricate dynamics at work, which are impacted by orbital interactions and molecular symmetry. These details frequently highlight TD-DFT's problems, particularly when it comes to accurately modelling electronic transitions in complicated molecular systems.
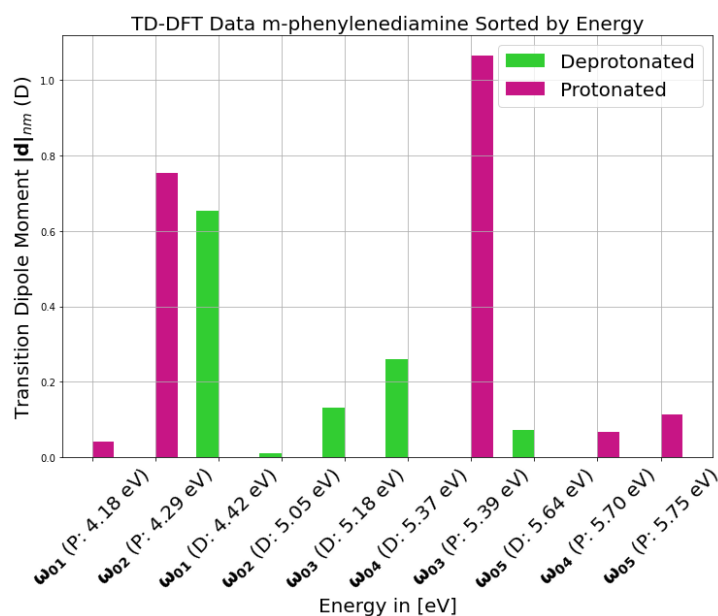
(a) Protonated and deprotonated m-phenylenediamine
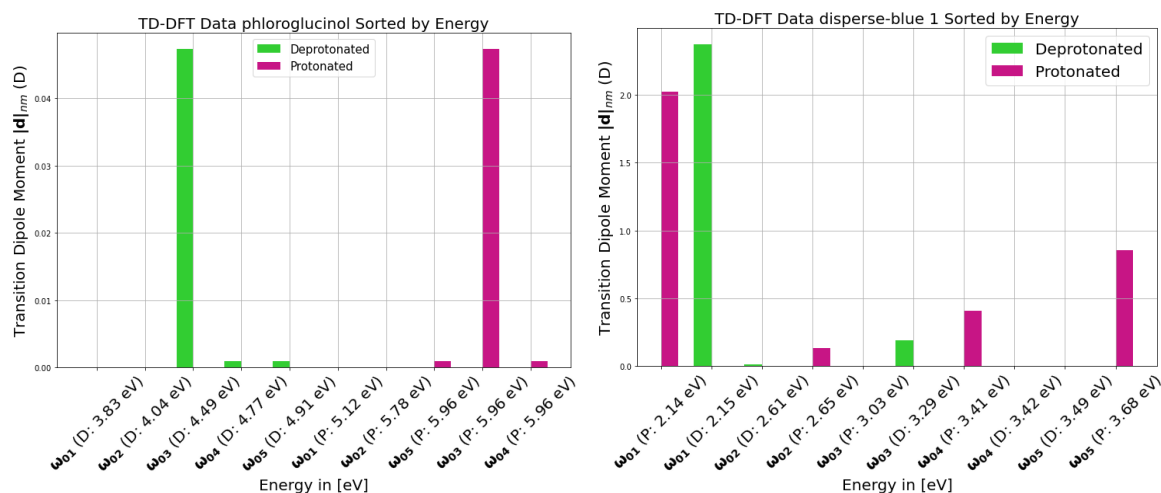
(b) Protonated and deprotonated phloroglucinol

(c) Protonated and deprotonated disperse-blue 1

Figure 3.1: Bar plots of the transition energies in eV and the absolute value of the transition dipole moment $|\mathbf{d}_{0n'}|$ for (a) m-phenylenediamine, (b) phloroglucinol, and (c) disperse-blue 1. The data was obtained with TD-DFT calculations performed with NWChem.

Table 3.1: Calculated transition frequencies ω and absolute value of transition dipole moments $|d|$ for mPD, phloroglucinol and disperse-blue 1 in their protonated and deprotonated states.

Molecule	n'	$\omega_{0n'}$ in (eV)	$|d|_{0n'}$ in (D)	Type
m-Phenylenediamine	1	4.416	0.65251	
	2	5.0473	0.01175	
	3	5.1784	0.13248	deprotonated
	4	5.3685	0.26094	
	5	5.6393	0.07140	
	1	4.1791	0.04085	
	2	4.2900	0.75491	
	3	5.3910	1.06484	protonated
	4	5.7031	0.06621	
	5	5.7491	0.11304	
phloroglucinol	1	3.8324	0.000036	
	2	4.0417	0.00004123	
	3	4.4930	0.04734	deprotonated
	4	4.7727	0.00089	
	5	4.9132	0.00098	
	1	5.1221	0.000036	
	2	5.7793	0.00004123	
	3	5.9586	0.04734	protonated
	4	5.9591	0.00089	
	5	5.9591	0.00098	
disperse-blue1	1	2.1527	2.37268	
	2	2.6107	0.01354	
	3	3.2875	0.18941	deprotonated
	4	3.4232	0	
	5	3.4902	0.00001	
	1	2.1360	2.02205	
	2	2.6493	0.13549	
	3	3.0264	0.00127	protonated
	4	3.4079	0.41043	
	5	3.6808	0.85421	

3.2.2   Resulting Transition Rates and Excitation Lifetimes

Using Equations (2.84) and (2.85), we determined the transition rates for each molecule in both protonated and deprotonated states, in free-space (fs) and medium-assisted space (ma). The cavity volumes, obtained via the COSMO solvation model (Ref.[56]) in NWChem, allowed us to approximate the vacuum layer thickness around each molecule by assuming a spherical shape and calculating the diameter as $l = \sqrt[3]{6V/\pi}$. The computed transition rates and excitation lifetimes are detailed in Tables 3.3 and

	Molecule	Cavity volume V (Å^3)	Cavity diameter l (Å)
depr.	mPD	92.672	5.61
	phloroglucinol	94.771	5.66
	disperse-blue1	175.831	6.95
prot.	mPD	90.611	5.57
	phloroglucinol	91.894	5.60
	disperse-blue1	175.230	6.94

Table 3.2: Molecular occupation volume V of in water dissolved protonated and deprotonated precursor molecules (m-phenylenediamine, phloroglucinol, and disperse-blue 1) and the corresponding spherical cavity diameters l.

3.4. For m-phenylenediamine, rates in free-space are generally lower compared to medium-assisted space, with protonated states displaying higher rates than deprotonated states across both environments. Notably, the rate for the transition from $S_2 \mapsto S_0$ in the protonated state reached $1.110 \times 10^7 s^{-1}$, significantly higher than in the deprotonated state.

Phloroglucinol and disperse-blue 1 exhibited similar behaviors, with medium-assisted transition rates consistently exceeding those in free-space. Interestingly, phloroglucinol showed zero transition rates for the second and third excited state transitions in its deprotonated form, suggesting possible forbidden transitions or inaccessible states under the study conditions.

Table 3.3: Calculated free-space (fs) and medium assisted (ma) transition rates for the first five excited states for m-phenylenediamine, phloroglucinol, and disperse-blue 1 using Equations 2.84 and 2.85.

Molecule	n'	Γ_{fs} in s^{-1}	Γ_{ma} in s^{-1}	Type
m-phenylenediamine	1	1.032×10^7	9.238×10^{11}	deprotonated
	2	4.378×10^3	1.014×10^9	
	3	6.010×10^5	7.609×10^{10}	
	4	2.598×10^6	6.924×10^{11}	
	5	2.255×10^5	3.120×10^{10}	
	1	3.003×10^4	6.132×10^9	protonated
	2	1.110×10^7	1.090×10^{12}	
	3	4.381×10^7	5.980×10^{12}	
	4	2.005×10^5	5.768×10^{10}	
	5	5.988×10^5	1.733×10^{11}	
phloroglucinol	1	1.253×10^5	1.5123×10^{10}	deprotonated
	2	0.0	0.0	
	3	9.200×10^6	8.132×10^{11}	
	4	7.379×10^6	6.560×10^{11}	
	5	0.0	0.0	
	1	4.308×10^{-2}	5.291×10^3	protonated
	2	8.092×10^{-2}	1.192×10^4	
	3	1.169×10^5	3.683×10^{10}	
	4	4.134×10^1	1.302×10^7	
	5	5.012×10^1	1.579×10^7	
disperse-blue 1	1	1.253×10^5	4.160×10^{12}	deprotonated
	2	8.045×10^2	2.818×10^8	
	3	3.143×10^5	2.980×10^{10}	
	4	0.0	0.0	
	5	1.048×10^{-3}	8.544×10^1	
	1	9.826×10^6	3.028×10^{12}	protonated
	2	8.418×10^4	1.415×10^{10}	
	3	1.103×10^1	3.110×10^6	
	4	1.644×10^6	1.422×10^{11}	
	5	8.973×10^6	6.430×10^{11}	

Molecule	$\Gamma_{tot,D}$ in (s^{-1})	τ_D in (s)	$\Gamma_{tot,HD}$ in (s^{-1})	τ_{HD} in (s)
m-phenylenediamine	9.238×10^{20}	0.00108	6.132×10^{18}	0.1631
phloroglucinol	1.512×10^{19}	0.0661	5.291×10^{12}	1.890×10^6
disperse-blue 1	4.160×10^{21}	0.00024	3.028×10^{21}	0.0033

Table 3.4: The resulting transition rates and excitation lifetimes for the three dye-molecules in their protonated (HD) and deprotonated (D) states calculated with Equation (2.83).

The observed variability in transition rates and the non-monotonic behavior of these rates across different states suggest complex interactions within the molecules' electronic structures. Protonation significantly alters these structures, affecting transition dynamics by shifting energy levels and altering electron densities.

For disperse-blue 1, the medium-assisted rates were notably higher than free-space rates, with the protonated form showing greater rates across transitions. This aligns with the expected influence of environmental interactions on transition dynamics.

Table 3.4 presents the corrected transition states and corresponding lifetimes for the first excited state, calculated using Equation (2.83). Lifetimes varied significantly, with phloroglucinol exhibiting the longest lifetimes due to its lower transition rates, particularly in its protonated form, which displayed lifetimes on the order of 10^6 ns.

The analysis confirms that environmental factors and protonation have effects on the electronic properties and transition dynamics of these molecules. The absence of consistent trends in transition rates and dipole moments underscores the complexity of molecular interactions and the impact of molecular symmetry and spatial overlap. Future work should continue to explore these dynamics, potentially incorporating more advanced computational methods or experimental validations to deepen our understanding of these phenomena.

3.2.3 pH Sensitivity of the Functional Groups

We are going to take into consideration the pH sensitivity of the protonated and deprotonated functional groups after calculating their transition rates in both free-space and medium. Table 3.5 displays the equilibrium pK_a constants for the first protonation (or first deprotonation, in the case of phloroglucinol).

Molecule	pK_a
m-phenylenediamine	4.96 (Ref.[57, 58])
phloroglucinol	8.9 (Ref.[59])
disperse blue 1 (tethered)	5 (Ref.[60])

Table 3.5: Equilibrium constant pK_a (first acid constants) for the investigated molecules.

Using the equilibrium constants we can now finally consider the pH sensitivity of each molecule using Equation (2.76). Using this Equation and comparing it with the experimentally obtained data in reference [4] for CD04, as this is based on only one dye molecule, mPD, and shows linear behaviour.
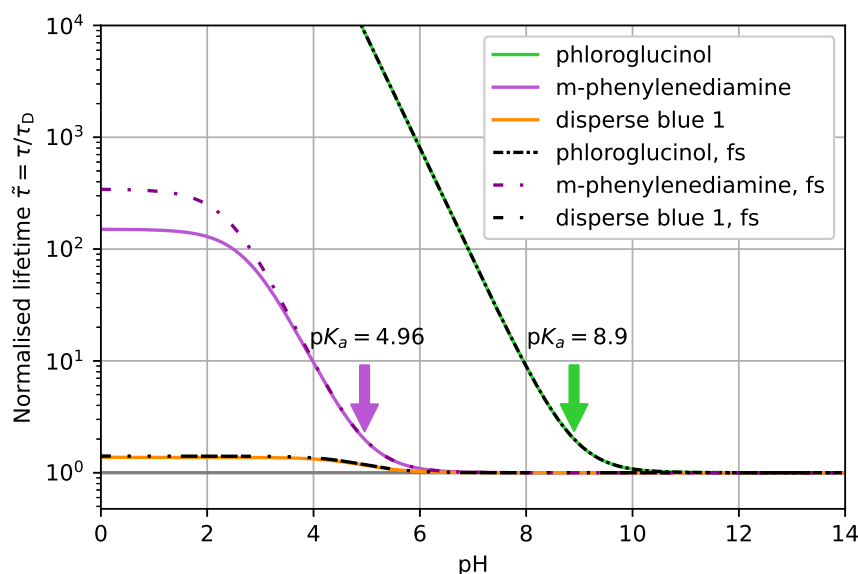

Figure 3.2: Change of excitation lifetimes at different pH rescaled to the deprotonated lifetime τ_D for m-phenylenediamine (red line), phloroglucinol (green line) and disperse blue 1 (blue line). The dashed-dotted lines illustrate the corresponding sensors without the impact of the carbon dots, adapted from [61].

By altering the pH of the surrounding solvent, Figure 3.2 shows how the excitation lifetimes of the functionalized carbon dots—functionalized with dye molecules such as m-phenylenediamine, phloroglucinol, and disperse-blue 1—change in relation to the excitation lifetimes of the deprotonated molecules by varying pH. Given that Γ_D and Γ_{HD} differ most (Table 3.4), phloroglucinol exhibits sensitivity over the widest pH range. The calculated rates for protonated phloroglucinol come from a

nearly non-existent transition dipole moment, suggesting the observation of a prohibited transition. Lifetimes are seen to increase when pH decreases, which is consistent with the experimental finding (Ref. [4]). According to Szapoczka (2023), fluorescence distinct from experimental observations, the effects of the functional groups m-phenylenediamine and phloroglucinol are overestimated, while disperse-blue 1 has a negligible pH dependency. This mismatch is explained by the electronic transition that was chosen from the TDDFT simulation. The electronic excitation under consideration, $S_1 \mapsto S_0$, decays quickly and enters the ground state directly, whereas luminscence is not a direct process, see section 2.1.

3.3   Summary

This section summarizes the uncertainties, presents an overview of the model used, and discusses potential sources of error. The TD-DFT calculations for each protonated/deprotonated form of the three surface-functional groups show a increasing trend with higher energy level gap for the transition frequencies $\omega_{0n'}$, which is expected as the higher the excited state the larger the energy gap to the ground state. The protonated form for each molecule yielded higher transition frequencies than the deprotonated form, as the additional proton alters the electronic structure, leading to a shift in energy levels. The transition dipole moments, $\mathbf{d}_{0n'}$ calculated with NWCHem do not show a trend, suggesting complex interactions within the molecules electronic states, that could not be captured.

Finally, the model to calculate the free-space as well as medium-assisted transition rates could be applied by inserting the transition frequencies and transition dipole moments obtained previously. It can be seen that the transitions for medium-assisted processes are much faster than for the free-space, indicating a faster excitation lifetime. For the deprotonated form of phloroglucinol and dipserse-blue 1 for some states a zero rate was obtained. This could mean that transitions for these states are not allowed or unlikely. This could be due to the choice of basis set and functional used for the TD-DFT calculations, which could affect the rates and predictions of energy levels, as mentioned in 2.8.3. In addition, TD-DFT calculations calculate excited states referring to the ground state, therefore it is not possible to calculate the total decay,

as illustrated for hydrogen atom, see Section 2.3, and required for luminescence (see Section 2.1). After having applied Equation (2.83), the direct decay for the transition $S_1 \mapsto S_0$, Γ_{01} as well as the excitation lifetime τ for this process was calculated for each protonated/deprotonated molecule. The rates as well as the resulting excitation lifetime are very fast, as expected, as we are not looking at the whole fluorescence lifetime process.

In the work of Szapoczka *et al.*[4], the transition rates for the carbon dot CD04, using m-phenylenediamine as a precursor, was at $\Gamma_D = 0.353 ns^{-1}$ and $\Gamma_{HD} = 0.328 ns^{-1}$ whereas the with the model calculated rates are at $\Gamma_D = 9.238 \times 10^{20} s^{-1}$ and $\Gamma_{HD} = 6.132 \times 10^{18} s^{-1}$, see Table 3.4. This significant difference can be explained by having a look at the approximation we made, see section 2.10 for a summary. First of all, the negligence of quasi-degeneracy can affect the rates of radiative transitions and leave out couplings between the states. The predictions for energy levels and transition frequencies could be affected by the choice of basis set and functional for the TD-DFT calculations.

The impact of pH changes on the excitation lifetimes of carbon dots functionalized with the specific dye molecules (m-phenylenediamine, phloroglucinol, and disperse-blue 1) showed, that phloroglucinol is particularly sensitive across a broad pH range due to notable differences in its decay rates when protonated and deprotonated, as shown in figure 3.2. The increase in lifetimes with decreasing pH aligns with experimental findings. However, the effects of m-phenylenediamine and phloroglucinol on fluorescence are reported to be overestimated, while disperse-blue 1 shows minimal pH sensitivity, a discrepancy attributed to the electronic transitions selected in TDDFT simulations. These transitions decay rapidly directly to the ground state.

Chapter 4

Conclusion

Fluorescence lifetime-based pH sensors have received a lot of interest in recent years due to their high long-term stability, low cost, and low power consumption. In many scientific and industrial domains, pH measurement is essential because even small changes in pH can have a big impact on chemical, biological, and physical processes. Accurate pH monitoring is crucial in fields including fish farming, aquaculture, climate studies, and medicine. In order to do this, Szapoczka *et al.* suggested using carbon dots (CDs), which are renowned for their outstanding photostability, strong fluorescence, and tunable size, to create a unique pH sensor. With a carbon core functionalized by a dye molecule, these small, spherical particles have intriguing properties for pH-sensitive applications.

To study the pH-dependent FL properties of CDs, W. Szapoczka et al. synthesised CDs with a variety of surface-functional groups, including as m-phenylenediamine (mPD), phloroglucinol, and disperse-blue 1. However, these CDs' early FL reactions to pH changes were low, suggesting that they weren't appropriate for sensitive pH sensing.

This thesis presents a theoretical model, with an emphasis on carbon dots especially, that describes the pH-dependence of excitation lifetimes in dissolved particles. Equations (2.72) to (2.75) outline our model, which offers a solid foundation for understanding the excitation lifetimes of isolated carbon dots at low-volume fractions. Most importantly, this theoretical framework makes it possible to interpolate the excitation lifetime across a range of pH values by using data from completely protonated and deprotonated species that can be obtained theoretically or practically at different

areas of the pH scale. Trends in experimental behaviours are explained by taking into consideration the protonation and deprotonation states of functional groups on the carbon dots, while also qualitatively addressing dependencies on the material characteristics. The applicability of the model to arbitrary solvent media can be enhanced by introducing mole fractions in mixed multi-component liquids.

Applying well-established local-field correction models allows us to further simplify our model by minimising the computational cost by concentrating just on the functionalizing dye molecules. This separation relies on the idea that the dye molecule can be thought of as existing independently of the aqueous environment and the carbon core. However, for small quantum dots (less than 10 nm in diameter), where electron confinement within the carbon lattice becomes important, this assumption might not be true. If the complete quantum dot is taken into account using TD-DFT, our model (2.75) nevertheless characterises such systems.

To fully replicate the experimental results for such systems, a thorough computation including the entire range of transitions between excited states and the phonon coupling permitting singlet-triplet transitions would be necessary.

Furthermore, the observed photophysical properties are significantly influenced by the chemical structure of the carbon dot, which includes both the carbon core and the functional groups. Further improvements of the model could determine the dielectric function of the carbon core using an atomic-level description, or it might take into account the distribution of carbon phases to provide a more thorough description of the carbon core. Additionally, taking into account the functional groups' higher protonation and deprotonation states might provide a more thorough and comprehensive description of the pH dependence.

In addition to providing a theoretical framework for understanding the behaviour of carbon dots under different pH levels, this thesis sets the way for additional experimental validation and theoretical improvement with the goal of improving the performance and utility of carbon dot-based sensors in a variety of scientific and technological areas.

Appendix A

Detailed calculations spectrum of hydrogen atom

The detailed calculations for the angular and radial part of the hydrogen dipoleoperator.

A.1 Angular part

$$f_x = \int_0^{2\pi} \mathrm{d}\varphi \int_0^{\pi} \mathrm{d}\vartheta \sin^2 \vartheta \cos \varphi \, (Y_l^m(\vartheta, \varphi))^{\star} Y_{l'}^{m'}(\vartheta, \varphi) \tag{A.1}$$

$$= \varepsilon^2 \sqrt{\frac{(2l+1)(l-m)!(2l'+1)(l'-m')!}{16\pi^2(l+m)!(l'+m')!}} \int_0^{2\pi} \mathrm{d}\varphi \int_0^{\pi} \mathrm{d}\vartheta \sin^2 \vartheta \cos \varphi$$

$$\times \exp(i\varphi(m-m')) P_l^m(\cos \vartheta) P_{l'}^{m'}(\cos \vartheta) \tag{A.2}$$

$$= \varepsilon^2 \sqrt{\frac{(2l+1)(l-m)!(2l'+1)(l'-m')!}{16\pi^2(l+m)!(l'+m')!}} \pi \int_0^{\pi} \mathrm{d}\vartheta \sin^2 \vartheta P_l^m(\cos \vartheta) P_{l'}^{m'}(\cos \vartheta) \tag{A.3}$$

$$= -\varepsilon^2 \sqrt{\frac{(2l+1)(l-m)!(2l'+1)(l'-m')!}{16\pi^2(l+m)!(l'+m')!}} \pi \int_{-1}^{1} \mathrm{d}x \sqrt{1-x^2} P_l^m(x) P_{l'}^{m'}(x) \tag{A.4}$$

$$= -\varepsilon^2 \sqrt{\frac{(2l+1)(l-m)!(2l'+1)(l'-m')!}{16\pi^2(l+m)!(l'+m')!}} \pi$$

$$\times \begin{cases} -\frac{1}{2l+1}\left[\delta_{m,m'+1}\delta_{l,l'+1} - \delta_{m,m'+1}\delta_{l,l'-1}\right] & \text{if } m = m+1, \\[2ex] \left[\frac{(l-m+1)(l-m+2)}{2l+1}\delta_{m,m'+1}\delta_{l,l'+1}\right. \\[2ex] \left. -\frac{(l+m-1)(l+m)}{2l+1}\delta_{m,m'-1}\delta_{l,l'-1}\right] & \text{if } m = m-1. \end{cases} \tag{A.5}$$

$$f_y = \int_0^{2\pi} d\varphi \int_0^{\pi} d\vartheta \sin^2 \vartheta \sin \varphi \left(Y_l^m(\vartheta, \varphi)\right)^\star Y_{l'}^{m'}(\vartheta, \varphi) \tag{A.6}$$

$$= \varepsilon^2 \sqrt{\frac{(2l+1)(l-m)!(2l'+1)(l'-m')!}{16\pi^2(l+m)!(l'+m')!}} \int_0^{2\pi} d\varphi \int_0^{\pi} d\vartheta \sin^2 \vartheta \sin \varphi \exp(i\varphi(m-m'))$$

$$\times P_l^m(\cos \vartheta) P_{l'}^{m'}(\cos \vartheta) \tag{A.7}$$

$$= \varepsilon^2 \sqrt{\frac{(2l+1)(l-m)!(2l'+1)(l'-m')!}{16\pi^2(l+m)!(l'+m')!}} \pi i \int_{-1}^{1} dx \sqrt{1-x^2} P_l^m(x) P_{l'}^{m'}(x) \tag{A.8}$$

$$= -\varepsilon^2 \sqrt{\frac{(2l+1)(l-m)!(2l'+1)(l'-m')!}{16\pi^2(l+m)!(l'+m')!}} \pi i$$

$$\times \begin{cases} \frac{1}{2l+1}\left[\delta_{m,m'+1}\delta_{l,l'+1} - \delta_{m,m'+1}\delta_{l,l'-1}\right] & \text{if } m = m'+1, \\[2mm] \left[\frac{(l-m+1)(l-m+2)}{2l+1}\delta_{m,m'+1}\delta_{l,l'+1}\right. \\[2mm] \left.- \frac{(l+m-1)(l+m)}{2l+1}\delta_{m,m'-1}\delta_{l,l'-1}\right] & \text{if } m = m'-1. \end{cases} \tag{A.9}$$

$$f_z = \int_0^{2\pi} d\varphi \int_0^{\pi} d\vartheta \sin \vartheta \cos \vartheta \left(Y_l^m(\vartheta, \varphi)\right)^\star Y_{l'}^{m'}(\vartheta, \varphi) \tag{A.10}$$

$$= \varepsilon^2 \sqrt{\frac{(2l+1)(l-m)!(2l'+1)(l'-m')!}{16\pi^2(l+m)!(l'+m')!}} \int_0^{2\pi} d\varphi \int_0^{\pi} d\vartheta \sin^2 \vartheta \exp(i\varphi(m-m'))$$

$$\times P_l^m(\cos \vartheta) P_{l'}^{m'}(\cos \vartheta) \tag{A.11}$$

$$= \varepsilon^2 \sqrt{\frac{(2l+1)(l-m)!(2l'+1)(l'-m')!}{16\pi^2(l+m)!(l'+m')!}} \int_{-1}^{1} dx\, x P_l^m(x) P_{l'}^{m'}(x) \tag{A.12}$$

$$= \varepsilon^2 \sqrt{\frac{(2l+1)(l-m)!(2l'+1)(l'-m')!}{16\pi^2(l+m)!(l'+m')!}} \pi \delta_{m,m'} \left[\sqrt{\frac{(l+1)^2 - m^2}{4(l+1)^2}}\delta_{l,l'+1}\right.$$

$$\left. + \sqrt{\frac{(l+m)^2}{4(l+1)^2}}\delta_{l,l'-1}\right]. \tag{A.13}$$

A.2 Radial part

$$R = \int_0^\infty r^3 R_{nl}(r) R_{n'l'}(r)\, dr \tag{A.14}$$

$$= f_{nl} f_{n'l'} \int_0^\infty r^3 e^{-r/(na_0)} \left(\frac{2r}{na_0}\right)^l L_{n-l-1}^{2l+1}\left(\frac{2r}{na_0}\right) e^{-r/(n'a_0)} \left(\frac{2r}{n'a_0}\right)^{l'} L_{n'-l'-1}^{2l'+1}\left(\frac{2r}{n'a_0}\right)\, dr \tag{A.15}$$

$$= f_{nl} f_{n'l'} \frac{2^{l+l'}}{n^l n'^{l'} a_0^{l+l'}} \int_0^\infty r^{3+l+l'} e^{-\frac{n+n'}{nn'a_0}r} L_{n-l-1}^{2l+1}\left(\frac{2r}{na_0}\right) L_{n'-l'-1}^{2l'+1}\left(\frac{2r}{n'a_0}\right)\, dr \tag{A.16}$$

$$= f_{nl} f_{n'l'} \frac{n^{4+l'} a_0^4}{16 n'^{l'}} \int_0^\infty x^{3+l+l'} e^{-\frac{n+n'}{2n'}x} L_{n-l-1}^{2l+1}(x) L_{n'-l'-1}^{2l'+1}\left(\frac{n}{n'}x\right)\, dx \tag{A.17}$$

substituted with $x = 2r/(na)$ to

$$f_{nl} f_{n'l'} \left(\frac{2}{na}\right)^l \left(\frac{2}{n'a}\right)^{l'} \left(\frac{na}{2}\right)^{4+l+l'} \int_0^\infty dx\, e^{-bx} x^{3+l+l'} L_{n-l-1}^{2l+1}(x)\, L_{n'-l'-1}^{2l'+1}(\mu x) \tag{A.18}$$

$$R = \begin{cases} f_{nl} f_{n',l+1} \left(\frac{2}{na}\right)^l \left(\frac{2}{n'a}\right)^{l+1} \left(\frac{na}{2}\right)^{2l+5} \times \\ \quad \int_0^\infty dx\, e^{-bx} x^{2l+4} L_{n-l-1}^{2l+1}(x) L_{n'-l-2}^{2l+3}(\mu x) & \text{if } l' = l+1, \\ f_{nl} f_{n',l-1} \left(\frac{2}{na}\right)^l \left(\frac{2}{n'a}\right)^{l-1} \left(\frac{na}{2}\right)^{2l+3} \times \\ \quad \int_0^\infty dx\, e^{-bx} x^{2l+2} L_{n-l-1}^{2l+1}(x) L_{n'-l}^{2l-1}(\mu x) & \text{if } l' = l-1. \end{cases} \tag{A.19}$$

The 3-point Rule

$$L_n^{(\alpha)}(x) = L_n^{(\alpha+1)}(x) - L_{n-1}^{(\alpha+1)}(x), \tag{A.20}$$

$$xL_{n-1}^{(\alpha+1)}(x) = (n+\alpha)L_{n-1}^{(\alpha)}(x) - nL_n^{(\alpha)}(x). \tag{A.21}$$

$$\int_0^\infty e^{-bx} x^\alpha L_n^\alpha(\lambda x) L_m^\alpha(\mu x)\, dx = \frac{\Gamma(m+n+\alpha+1)}{m!n!}(b-\lambda)^n \frac{(b-\mu)^m}{b^{m+n+\alpha+1}}$$
$$\times\, {}_2F_1\left[-m,-n;-m-n-\alpha; \frac{b(b-\lambda-\mu)}{(b-\lambda)(b-\mu)}\right]. \tag{A.22}$$

A.3   Calculation of the Hydrogen Dipole Operator with Python

The analytical calculations in section ... have been tested and compared with a numerical calculation in python. The code for the analytical calculation is as follows

Analytical Codes for Angular part x,y,z-component

```python
def angular_x_plain(m, l, m_prime, l_prime):
    if m_prime == m + 1 and l_prime == l + 1:
        f_x = np.pi * (-1 / (2 * l + 1) * (2 * sp.factorial(l + m
            + 2)) / ((2 * l + 3) * sp.factorial(l - m)))
    elif m_prime == m - 1 and l_prime == l - 1:
        f_x = np.pi * 1 / (2 * l + 1) * (l + m - 1) * (l + m) *
            (2 * sp.factorial(l + m - 2)) / ((2 * l - 1) * sp.
            factorial(l - m))
    elif m_prime == m + 1 and l_prime == l - 1:
        f_x = np.pi * (1 / (2 * l + 1)) * 2 * sp.factorial(l + m)
            / ((2 * l - 1) * sp.factorial(l - m - 2))
    elif m_prime == m - 1 and l_prime == l + 1:
        f_x = np.pi * (1 / (2 * l + 1)) * (l + m - 1) * (l + m) *
            2 * sp.factorial(l + m - 2) / ((2 * l - 1) * sp.
            factorial(l - m))
    else:
        f_x = 0
    return f_x
```

```python
def angular_y_plain(m, l, m_prime, l_prime):
    if m_prime == m + 1 and l_prime == l + 1:
        f_y = 1j*np.pi * (-1 / (2 * l + 1) * (2 * sp.factorial(l
            + m + 2)) / ((2 * l + 3) * sp.factorial(l - m)))
    elif m_prime == m - 1 and l_prime == l - 1:
        f_y = 1j*np.pi * 1 / (2 * l + 1) * (l + m - 1) * (l + m)
            * (2 * sp.factorial(l + m - 2)) / ((2 * l - 1) * sp.
            factorial(l - m))
```

```
6     elif m_prime == m + 1 and l_prime == l - 1:
7         f_y = 1j*np.pi * (1 / (2 * l + 1)) * 2 * sp.factorial(l +
              m) / ((2 * l - 1) * sp.factorial(l - m - 2))
8     elif m_prime == m - 1 and l_prime == l + 1:
9         f_y = 1j*np.pi * (1 / (2 * l + 1)) * (l + m - 1) * (l + m
              ) * 2 * sp.factorial(l + m - 2) / ((2 * l - 1) * sp.
              factorial(l - m))
10    else:
11        f_y = 0
12    return f_y
```

```
1     def ang_ana_z(m, l, m_prime, l_prime):
2     if m == m_prime and l ==l_prime+1:
3         f_z = np.sqrt((l_prime+2)**2-(m_prime)**2/(4*(l_prime+2)
              **2))*np.pi
4     elif m == m_prime and l == l_prime-1:
5         f_z = np.sqrt((l_prime+m_prime-1)**2/(4*(l_prime)**2))*np
              .pi
6     else:
7         f_z = 0
8     return f_z
```

Numerical Codes for Angular part x,y,z-component

Defining first the Laguerre integral with

```
1 def integral_num(b ,n, m, alpha,lam,mu):
2     return gauss_laguerre_integration(alpha, b, n, m, lam, mu)
```

an analytical calculation in python can be done with the final code

```
1   def radial_ana(n, l, n_prime, l_prime):
2     b = n * (1 / n + 1 / n_prime) / 2
3     lambda_val = 1
4     mu = n / n_prime
5     print(n, l, n_prime, l_prime, b, mu)
6     A= a**4*n_prime**4/16
```

```
 7      if l_prime == l+1:
 8          alpha = 2*l+4
 9          hilf = integral(b, mu*n_prime-l-1, n_prime-l-2, alpha,
                lambda_val, mu)
10          print(f"first integral l+1, hilf: {hilf}")
11          hilf += -3*integral(b, mu*n_prime-l-2, n_prime-l-2, alpha
                , lambda_val, mu)
12          print(f"2nd integral l+1, hilf: {hilf}")
13          hilf += 3*integral(b, mu*n_prime-l-3, n_prime-l-2, alpha,
                lambda_val, mu)
14          print(f"3rd integral l+1, hilf: {hilf}")
15          hilf += -integral(b, mu*n_prime-l-4, n_prime-l-2, alpha,
                lambda_val, mu)
16          print(f"4th integral l+1, hilf: {hilf}")
17          hilf += -integral(b, mu*n_prime-l-1, n_prime-l-3, alpha,
                lambda_val, mu)
18          print(f"5th integral l+1, hilf: {hilf}")
19          hilf += 3*integral(b, mu*n_prime-l-2, n_prime-l-3, alpha,
                lambda_val, mu)
20          print(f"6th integral l+1, hilf: {hilf}")
21          hilf += -3*integral(b, mu*n_prime-l-3, n_prime-l-3, alpha
                , lambda_val, mu)
22          print(f"7th integral l+1, hilf: {hilf}")
23          hilf += integral(b, mu*n_prime-l-4, n_prime-l-3, alpha,
                lambda_val, mu)
24          print(f"8th integral l+1, hilf: {hilf}")
25          return hilf*A*mu**(5+l)
26      elif l_prime == l-1:
27          alpha = 2*l+2
28          hilf = integral(b, mu*n_prime-l-1, n_prime-l, alpha,
                lambda_val, mu)
29          print(f"first integral l-1, hilf: {hilf}")
30          hilf += -3*integral(b, mu*n_prime-l-1, n_prime-l-1, alpha
                , lambda_val, mu)
```

```python
31        print(f"second integral l-1, hilf: {hilf}")
32        hilf += 3*integral(b, mu*n_prime-l-1, n_prime-l-2, alpha,
             lambda_val, mu)
33        print(f"third integral l-1, hilf: {hilf}")
34        hilf += -integral(b, mu*n_prime-l-1, n_prime-l-3, alpha,
             lambda_val, mu)
35        print(f"4th integral l-1, hilf: {hilf}")
36        hilf += -integral(b, mu*n_prime-l-2, n_prime-l, alpha,
             lambda_val, mu)
37        print(f"5th integral l-1, hilf: {hilf}")
38        hilf += 3*integral(b, mu*n_prime-l-2, n_prime-l-1, alpha,
             lambda_val, mu)
39        print(f"6th integral l-1, hilf: {hilf}")
40      # hilf += -integral(b, mu*n_prime-l-2, n_prime-l, alpha,
             lambda_val, mu)
41      #print(f"7th integral l-1, hilf: {hilf}")
42        hilf += -3*integral(b, mu*n_prime-l-2, n_prime-l-2, alpha
             , lambda_val, mu)
43        print(f"8th integral l-1, hilf: {hilf}")
44        hilf += integral(b, mu*n_prime-l-2, n_prime-l-3, alpha,
             lambda_val, mu)
45        print(f"9th integral l-1, hilf: {hilf}")
46        return A*mu**(3+l)*hilf
47    else:
48        return np.nan
```

Dipole Operator Code

The angular part and radial part are combined with respect to the selection rules and the final calculation can be obtained with this code:

```python
1    def dipole_hydrogen(n, m, l, n_prime, m_prime, l_prime):
2    if isquantum(n, l, m) and isquantum(n_prime, l_prime, m_prime
         ) and selectionrule2(m, l, m_prime, l_prime) and n_prime
         != n:
```

```
3        f_x = angular_x_plain(m, l, m_prime, l_prime)*Vorfaktor(m,
            l, m_prime, l_prime)
4        f_y = angular_y_plain(m, l, m_prime, l_prime)*Vorfaktor(m,
            l, m_prime, l_prime)
5        f_z = angular_z_plain(m, l, m_prime, l_prime)*Vorfaktor(m,
            l, m_prime, l_prime)
6        return np.array([f_x, f_y, f_z])*radial_ana(n, l, n_prime,
            l_prime)*Vorfaktor(m, l, m_prime, l_prime)*f_nl(n, l)*
            f_nl(n_prime, l_prime)*(-sc.elementary_charge)
7    else:
8        return np.array([0, 0, 0])
```

A.3.1 The Hohenberg-Kohn Theorems

The Hohenberg-Kohn theorems formualte density functional theory as exact theory of many-body systems. The Hamiltonian can be written as

$$\hat{H} = -\frac{\hbar}{2m_e} \sum_i \nabla_i^2 + \sum_i V_{ext}(r_i) + \frac{1}{2} \sum_{i \neq j} \frac{e^2}{|r_i - r_j|} \tag{A.23}$$

Proof Theorem I

The first theorem, as discussed earlier, establishes a fundamental principle: in any many-body quantum system, the particle density of the ground state uniquely determines all properties of the system. If two different external potentials result in the same ground state particle density, these potentials are essentially equivalent when it comes to describing the system's properties. This proof is significant because it enhances the practical utility and conceptual foundation of electronic structure calculations. It simplifies computations by allowing to focus on the particle density, a more manageable quantity, and facilitates the application of density functional theory. The theorem assures that when two potentials lead to the same electron density, they are interchangeable in terms of predicting and understanding the behavior of electrons in complex systems.

We suppose we have two external potentials $V_{ext}^{(1)}$ and $V_{ext}^{(2)}$ differing by a constant and

leading to the same ground state density $n(\boldsymbol{r})$. Each potential has a Hamiltonian, $\hat{H}^{(1)}$ and $\hat{H}^{(2)}$, with different ground state wavefunctions $\psi^{(1)}$ and $\psi^{(2)}$. The wavefunctions are assumed to have the same groundstate energy $n_0(\boldsymbol{r})$. Since the potentials lead to different Hamiltonians and wavefunctions, the expectation value of the energy of potential $V_{\text{ext}}^{(1)}$ is less than for $V_{\text{ext}}^{(2)}$:

$$E^{(1)} = \langle \psi^{(1)} | \hat{H}^{(1)} | \psi^{(1)} \rangle < \langle \psi^{(2)} | \hat{H}^{(1)} | \psi^{(2)} \rangle \tag{A.24}$$

The strict inequality is claimed to follow if the ground state is non-degenerate. Non-degenerate means there is a unique ground state for a given system. We can rewrite the equation and express it as

$$\begin{aligned} \langle \psi^{(2)} | \hat{H}^{(1)} | \psi^{(2)} \rangle &= \langle \psi^{(2)} | \hat{H}^{(2)} | \psi^{(2)} \rangle + \langle \psi^{(2)} | \hat{H}^{(1)} - \hat{H}^{(2)} | \psi^{(2)} \rangle \\ &= E^{(2)} + \int d^3 r [V_{\text{ext}}^{(1)}(\boldsymbol{r}) - V_{\text{ext}}^{(2)}(\boldsymbol{r})] n_0(\boldsymbol{r}) \end{aligned} \tag{A.25}$$

and the expectation value can be written as

$$E^{(1)} < E^{(2)} + \int d^3 r [V_{\text{ext}}^{(1)}(\boldsymbol{r}) - V_{\text{ext}}^{(2)}(\boldsymbol{r})] n_0(\boldsymbol{r}) \tag{A.26}$$

The same rule is valid for the opposite case if we consider the Hamiltonian $\hat{H}^{(2)}$:

$$E^{(2)} < E^{(1)} + \int d^3 r [V_{\text{ext}}^{(2)}(\boldsymbol{r}) - V_{\text{ext}}^{(1)}(\boldsymbol{r})] n_0(\boldsymbol{r}) \tag{A.27}$$

After expressing both expectation values for each potential $V_{\text{ext}}^{(1)}$ and $V_{\text{ext}}^{(2)}$, we can add together equations A.3.1 and A.3.1 and derive

$$E^{(1)} + E^{(2)} < E^{(1)} + E^{(2)} \tag{A.28}$$

this shows a contradictory inequality and it arises from the assumption that there are two different external potentials differing by more than a constant that give rise to the same non-degenerate ground state charge density. This is not possible, and it implies that the density uniquely determines the external potential up to a constant, leading to the conclusion that, in principle, the wave function of any state is determined by solving the Schrödinger equation with the Hamiltonian that is uniquely determined by the ground state density.

Proof Theorem II

As mentioned above, the second theorem states that the total energy of a system can be expressed as a functional of the electron density. The functional takes the form E[n], where E is the total energy and n is the electron density. All properties are now determined uniquely as functionals of $n(\boldsymbol{r})$

$$E_{HK}[n] = T[n] + E_{int}[n] + \int d^3r V_{ext}(\boldsymbol{r}) n(\boldsymbol{r}) + E_{II} \equiv F_{HK}[n] + \int d^3r V_{ext}(\boldsymbol{r}) n(\boldsymbol{r}) + E_{II}$$
(A.29)

E_{II} is the interaction energy of the nuclei, $F_{HK}[n]$ includes the internal energies of the interacting electron system:

$$F_{HK}[n] = T[n] + E_{int}[n]$$
(A.30)

To get to our proof we consider a system with ground state density $n^{(1)}\boldsymbol{r}$ influenced by an external potential $V_{ext}^{(1)}$. The functional has now to be equal to the expectation value of the ground state hamiltonian $\hat{H}^{(1)}$ with wave function $\psi^{(1)}$

$$E^{(1)} = E_{HK}[n^{(1)}] = \langle \psi^{(1)} | | \hat{H}^{(1)} | | \psi^{(1)} \rangle$$
(A.31)

As soon as we consider a different density $n^{(2)}\boldsymbol{r}$ that is corresponding to a different wave function $\psi^{(2)}$, it immediately can be seen that the energy of this state is larger than the one of the ground state

$$E^{(1)} = \langle \psi^{(1)} | | \hat{H}^{(1)} | | \psi^{(1)} \rangle < \langle \psi^{(2)} | | \hat{H}^{(1)} | | \psi^{(2)} \rangle = E^{(2)}$$
(A.32)

In summary, the second theorem of density functional theory establishes a profound connection between the total energy of a quantum system and its electron density. The total energy, expressed as the functional $E[n]$, encapsulates all system properties uniquely in terms of the electron density $n(\boldsymbol{r})$. The Hohenberg–Kohn functional, denoted as $F_{HK}[n]$, plays a crucial role in this formulation, encompassing kinetic, interaction, and external potential energies. The proof involves considering a system with a ground state density $n^{(1)}(\boldsymbol{r})$ influenced by an external potential $V_{ext}^{(1)}(\boldsymbol{r})$. The energy of this state, $E^{(1)}$, is determined by the expectation value of the ground state Hamiltonian $\hat{H}^{(1)}$ with wave function $\psi^{(1)}$. The comparison with a different density

$n^{(2)}(r)$ and corresponding wave function $\psi^{(2)}$ reveals that the energy of the ground state ($E^{(1)}$) is lower than that of any other state ($E^{(2)}$). This foundational result underscores the power of density functional theory in uniquely determining ground state properties, paving the way for a deeper understanding of quantum systems.

Proof Runge-Gross Theorem

We aim to demonstrate that the time evolution of the electron density is exclusively determined by the disparity in external potentials. The time-dependent current density $\mathbf{j}(\mathbf{r}, t)$ is connected to the electron density through the continuity equation:

$$\frac{\partial \Delta j(x)}{\partial t}\bigg|_{t=0} = -i\langle\psi_0|[\hat{\mathbf{j}}(\mathbf{r}), \triangle\hat{H}(t_0)]|\psi_0\rangle = -n_0(\mathbf{r})\nabla\triangle V_{\text{ext}}(\mathbf{r}, 0)$$

In this context, $\Delta j(x)$ signifies the difference in current densities, Ψ_0 is the initial state, $\hat{j}(r)$ represents the current operator, $\Delta\hat{H}(t_0)$ indicates the difference in Hamiltonians at time t_0, $n_0(r)$ is the initial density, and $\nabla\Delta v_{\text{ext}}(r, 0)$ is the gradient of the difference in external potentials. If $\triangle V_{\text{ext}}(\mathbf{r}, t)$ takes a value such that $\frac{\partial n(\mathbf{r},t)}{\partial t} \neq 0$ for any r and t, then there is a direct connection between changes in the external potential and the resulting time evolution of the electron density. This implies that adjustments in the external potential uniquely dictate the behavior of the electron density over time.

We expand this concept by extending the one-to-one mapping between external potential and current densities to electron densities. The continuity equation ($\Delta n'(\mathbf{r}) = -\nabla \cdot \Delta\mathbf{j}(\mathbf{r})$) links the time derivative of the density difference ($\Delta n'(\mathbf{r})$) with the divergence of the current density difference ($\Delta\mathbf{j}(\mathbf{r})$). This equation illustrates that the rate of change of the density difference over time is connected to the divergence of the current density difference. Despite the presence of divergence terms, the theorem affirms that the density difference is uniquely determined by differences in external potentials. This conclusion holds for any physically realistic density, ensuring a robust foundation for the theorem. A comprehensive derivation of this theorem is available in reference [45] chapter 22.

Appendix B

Geometry files of Precursors

This chapter provides the geometry.xyz files of all the precursor molecules generated with the software Avogadro2 as well as the optimized geometry files after performing DFT calculations.

B.1   m-PD

In this section the geometry files for mPD are provided.

B.1.1   Avogadro2 generated .xyz files

For the protonated mPD:

```
 1       17
 2 m-phenylenediamine
 3 C        1.20090     -0.29590     -0.00210
 4 C       -0.00000     -0.99130     -0.00160
 5 C       -1.20090     -0.29590      0.00010
 6 C       -1.19730      1.09380      0.00120
 7 C        0.00000      1.78300      0.00020
 8 C        1.19740      1.09380     -0.00100
 9 N       -2.41180     -0.99190      0.00020
10 N        2.41180     -0.99190      0.00200
11 H       -0.00000     -2.07130     -0.00280
12 H       -2.13160      1.63560      0.00260
13 H        0.00000      2.86300      0.00040
14 H        2.13160      1.63560     -0.00180
15 H       -2.41370     -1.96190     -0.00090
16 H       -3.25090     -0.50530      0.00140
17 H        2.41370     -1.96190      0.00520
18 H        3.25090     -0.50530      0.00160
19 H        2.40736     -1.00383     -0.89794
```

Listing B.1: mPD protonated geometry.xyz file generated with Avogadro2.

Optimized protonated mPD geometry file:

```
 1         17
 2  geometry
 3  C                    -0.21637158      -1.12454695      -0.06817174
 4  C                    -0.97668493       0.04155905      -0.08540044
 5  C                    -0.30906841       1.28810578      -0.01884152
 6  C                     1.11027577       1.27428916       0.06210446
 7  C                     1.82299603       0.08519428       0.07599205
 8  C                     1.16863705      -1.15751405       0.01045550
 9  N                    -0.99590750       2.45928039      -0.03152871
10  N                    -0.94932472      -2.42230257      -0.13955808
11  H                    -2.06817181       0.00771961      -0.14901333
12  H                     1.64646726       2.22531650       0.11448349
13  H                     2.91326768       0.11281516       0.13890191
14  H                     1.73312271      -2.09325654       0.02190559
15  H                    -2.00474967       2.48461784      -0.08943593
16  H                    -0.51034334       3.34515606       0.01587411
17  H                    -1.60053855      -2.54183325       0.65186572
18  H                    -0.29289228      -3.21511374      -0.11856237
19  H                    -1.50343589      -2.50548070      -1.00604350
```

Listing B.2: mPD optimized protonated geometry.xyz file generated with Avogadro2.

Deprotonated mPD geometry:

```
 1       16
 2  m-phenylenediamine
 3  C       1.20090     -0.29590     -0.00210
 4  C      -0.00000     -0.99130     -0.00160
 5  C      -1.20090     -0.29590      0.00010
 6  C      -1.19730      1.09380      0.00120
 7  C       0.00000      1.78300      0.00020
 8  C       1.19740      1.09380     -0.00100
 9  N      -2.41180     -0.99190      0.00020
10  N       2.41180     -0.99190      0.00200
11  H      -0.00000     -2.07130     -0.00280
12  H      -2.13160      1.63560      0.00260
13  H       0.00000      2.86300      0.00040
14  H       2.13160      1.63560     -0.00180
15  H      -2.41370     -1.96190     -0.00090
16  H      -3.25090     -0.50530      0.00140
17  H       2.41370     -1.96190      0.00520
18  H       3.25090     -0.50530      0.00160
```

Listing B.3: mPD deprotonated geometry.xyz file generated with Avogadro2.

optimized:

```
 1         16
 2  geometry
 3  C                    -0.29902895      -1.22416492      -0.05963257
```

```
 4  C                    -0.98787171        0.00016485        0.00016598
 5  C                    -0.29888923        1.22427342        0.05995898
 6  C                     1.11139964        1.21677692        0.05915376
 7  C                     1.79160505       -0.00003892        0.00021317
 8  C                     1.11119550       -1.21684646       -0.05890775
 9  N                    -1.00041241        2.42172560        0.17197486
10  N                    -1.00095079       -2.42137953       -0.17121949
11  H                    -2.08317618       -0.00005093        0.00003031
12  H                     1.66186773        2.16030050        0.11057522
13  H                     2.88590155       -0.00017646        0.00060055
14  H                     1.66159143       -2.16044573       -0.11005924
15  H                    -1.95441096        2.41025943       -0.17161622
16  H                    -0.49650334        3.25339308       -0.11524979
17  H                    -1.95419502       -2.41034854        0.17433720
18  H                    -0.49644641       -3.25337356        0.11385288
```

Listing B.4: mPD optimized protonated geometry.xyz file generated with NWChem.

B.1.2 Phloroglucinol

protonated:

```
 1       16
 2  phloroglucinol
 3  C      -1.38610      -0.03930        0.02050
 4  O      -2.74420      -0.07770        0.04840
 5  C      -0.72710       1.18080        0.00710
 6  C       0.65880       1.22010       -0.02140
 7  O       1.30450       2.41580       -0.03490
 8  C       1.38580       0.03930       -0.03570
 9  C       0.72680      -1.18090       -0.02190
10  O       1.43920      -2.33800       -0.03630
11  C      -0.65900      -1.22010        0.01110
12  H      -3.15540      -0.08870       -0.82680
13  H      -1.29330       2.10050        0.01860
14  H       1.50960       2.76200        0.84440
15  H       2.46510       0.06980       -0.05790
16  H       1.66360      -2.67280        0.84270
17  H      -1.17220      -2.17030        0.02180
18  H      -3.32367      -0.08383        0.97241
```

Listing B.5: Phloroglucinol protonated geometry.xyz file generated with Avogadro2.

Optimized:

```
 1        16
 2   geometry
 3   C                     0.06747757        1.34383322       -0.00385148
 4   O                     0.12666894        2.83073314       -0.11753488
 5   C                     1.29268540        0.71522436        0.04189274
 6   C                     1.24875406       -0.69346762        0.14959353
 7   O                     2.42827227       -1.32161554        0.19547235
 8   C                     0.01293662       -1.35816313        0.20252091
```

```
 9  C                        -1.19683504      -0.64558144        0.15030206
10  O                        -2.40011293      -1.22859420        0.19694795
11  C                        -1.18514997       0.76206382        0.04286857
12  H                        -0.25365535       3.18535957       -0.94930595
13  H                         2.24488299       1.24389509       -0.00045019
14  H                         2.32227255      -2.28150054        0.26870064
15  H                        -0.00895047      -2.44923932        0.28583656
16  H                        -2.32985250      -2.19170581        0.27042973
17  H                        -2.12565820       1.31391223        0.00258337
18  H                        -0.24479024       3.30765410        0.65500809
```

Listing B.6: Phloroglucinol optimized protonated geometry.xyz file generated with NWChem.

deprotonated:

```
 1        14
 2  phloroglucinol
 3  C      -1.38610     -0.03930      0.02050
 4  O      -2.74420     -0.07770      0.04840
 5  C      -0.72710      1.18080      0.00710
 6  C       0.65880      1.22010     -0.02140
 7  O       1.30450      2.41580     -0.03490
 8  C       1.38580      0.03930     -0.03570
 9  C       0.72680     -1.18090     -0.02190
10  O       1.43920     -2.33800     -0.03630
11  C      -0.65900     -1.22010      0.01110
12  H      -3.15540     -0.08870     -0.82680
13  H      -1.29330      2.10050      0.01860
14  H       1.50960      2.76200      0.84440
15  H       2.46510      0.06980     -0.05790
16  H      -1.17220     -2.17030      0.02180
```

Listing B.7: Phloroglucinol deprotonated geometry.xyz file generated with Avogadro2.

optimized:

```
 1         14
 2   geometry
 3   C                        1.22296721      -0.13827696        0.73208407
 4   O                        2.33425739      -0.26390355        1.49793450
 5   C                        0.00000000       0.00000000        1.43439060
 6   C                       -1.22296721       0.13827696        0.73208407
 7   O                       -2.33425739       0.26390355        1.49793450
 8   C                       -1.23817385       0.13913224       -0.65050593
 9   C                        0.00000000       0.00000000       -1.40467046
10   O                        0.00000000       0.00000000       -2.65293030
11   C                        1.23817385      -0.13913224       -0.65050593
12   H                        3.10919893      -0.35151563        0.92634784
13   H                        0.00000000       0.00000000        2.52563182
14   H                       -3.10919893       0.35151563        0.92634784
15   H                       -2.16239917       0.24107109       -1.22551226
16   H                        2.16239917      -0.24107109       -1.22551226
```

Listing B.8: Phloroglucinoloptimized deprotonated geometry.xyz file generated with NWChem.

B.1.3 Disperse-blue1

protonated:

```
 1      33
 2 disperse blue 1
 3 C       3.67020     -0.68760     -0.23330
 4 C       3.67020      0.68750     -0.23360
 5 C      -3.67030     -0.68760     -0.23250
 6 C      -3.67020      0.68750     -0.23370
 7 H       1.66600     -3.27650     -0.25120
 8 H       3.31450     -3.26410      0.07270
 9 H       3.31470      3.26400      0.07280
10 H       1.66600      3.27660     -0.25020
11 H      -3.31440     -3.26410      0.07240
12 H      -1.66590     -3.27640     -0.25140
13 H      -1.66600      3.27660     -0.25070
14 H      -3.31470      3.26400      0.07240
15 C       2.47600     -1.39740     -0.08800
16 C       2.47600      1.39740     -0.08840
17 C      -2.47590     -1.39740     -0.08830
18 C      -2.47600      1.39740     -0.08870
19 O      -0.00000     -2.62650      0.46040
20 O      -0.00000      2.62640      0.46050
21 C       0.00000     -1.43530      0.21070
22 C      -0.00000      1.43530      0.21040
23 C       1.27050     -0.70570      0.05770
24 C       1.27050      0.70570      0.05760
25 C      -1.27040     -0.70570      0.05750
26 C      -1.27050      0.70570      0.05730
27 N       2.48650     -2.78530     -0.08890
28 N       2.48660      2.78530     -0.08860
29 N      -2.48650     -2.78530     -0.08920
30 N      -2.48660      2.78530     -0.08900
31 H       4.60070     -1.22310     -0.35080
32 H       4.60120      1.22310     -0.34660
33 H      -4.60140     -1.22310     -0.34530
34 H      -4.60130      1.22310     -0.34650
35 H      -2.34283     -3.03914      0.89827
```

Listing B.9: Disperseblue1 dye protonated geometry.xyz file generated with Avogadro2.

Optimized:

```
 1        33
 2  geometry
 3  C                 -0.74100059     -3.69875933     -0.07678730
```

```
 4  C                 0.61817804      -3.71879167      -0.10035071
 5  C                -0.60788569       3.71760666       0.01950471
 6  C                 0.77289205       3.71275763      -0.00392584
 7  H                -3.35909006      -1.67575776      -0.00400636
 8  H                -3.27022454      -3.43192830      -0.02943289
 9  H                 3.18298062      -3.53621019      -0.14177187
10  H                 3.28414834      -1.75607610      -0.11833883
11  H                -3.17818758       3.01949440      -0.76821624
12  H                -2.98595697       1.09186193       0.02605507
13  H                 3.35670052       1.65065059      -0.07519772
14  H                 3.33839397       3.42789527      -0.05183977
15  C                -1.47119445      -2.46260409      -0.04729547
16  C                 1.40503689      -2.50982129      -0.09704523
17  C                -1.33359967       2.52012339       0.01608837
18  C                 1.51137577       2.49713729      -0.03254777
19  O                -2.69483178       0.06011252       0.00763947
20  O                 2.75038250      -0.05121024      -0.08661624
21  C                -1.38388451       0.01989591      -0.01560181
22  C                 1.49708995      -0.02562452      -0.06517194
23  C                -0.72156599      -1.23264928      -0.04356951
24  C                 0.72595347      -1.26731968      -0.06863952
25  C                -0.64497255       1.28625259      -0.01175688
26  C                 0.77965532       1.25909784      -0.03634980
27  N                -2.81029735      -2.52929574      -0.02491211
28  N                 2.74473562      -2.62465257      -0.12079111
29  N                -2.78700894       2.52914625       0.04115704
30  N                 2.85622258       2.53895050      -0.05511012
31  H                -1.30225538      -4.63685874      -0.07999909
32  H                 1.14257230      -4.67847317      -0.12229497
33  H                -1.14508482       4.67008745       0.04098604
34  H                 1.31959398       4.65932511      -0.00087317
35  H                -3.14992813       2.99819782       0.87591274
```

Listing B.10: Disperseblue1 dye optimized protonated geometry.xyz file generated with NWChem.

Deprotonated:

```
 1       32
 2  disperse blue 1
 3  C          3.67020       -0.68760       -0.23330
 4  C          3.67020        0.68750       -0.23360
 5  C         -3.67030       -0.68760       -0.23250
 6  C         -3.67020        0.68750       -0.23370
 7  H          1.66600       -3.27650       -0.25120
 8  H          3.31450       -3.26410        0.07270
 9  H          3.31470        3.26400        0.07280
10  H          1.66600        3.27660       -0.25020
11  H         -3.31440       -3.26410        0.07240
12  H         -1.66590       -3.27640       -0.25140
13  H         -1.66600        3.27660       -0.25070
14  H         -3.31470        3.26400        0.07240
15  C          2.47600       -1.39740       -0.08800
16  C          2.47600        1.39740       -0.08840
17  C         -2.47590       -1.39740       -0.08830
```

```
18 C              -2.47600          1.39740         -0.08870
19 O              -0.00000         -2.62650          0.46040
20 O              -0.00000          2.62640          0.46050
21 C               0.00000         -1.43530          0.21070
22 C              -0.00000          1.43530          0.21040
23 C               1.27050         -0.70570          0.05770
24 C               1.27050          0.70570          0.05760
25 C              -1.27040         -0.70570          0.05750
26 C              -1.27050          0.70570          0.05730
27 N               2.48650         -2.78530         -0.08890
28 N               2.48660          2.78530         -0.08860
29 N              -2.48650         -2.78530         -0.08920
30 N              -2.48660          2.78530         -0.08900
31 H               4.60070         -1.22310         -0.35080
32 H               4.60120          1.22310         -0.34660
33 H              -4.60140         -1.22310         -0.34530
34 H              -4.60130          1.22310         -0.34650
```

Listing B.11: Disperseblue1 dye deprotonated geometry.xyz file generated with Avogadro2.

Optimized

```
 1         33
 2  geometry
 3  C                 -0.72608927       -3.70283323       -0.22615785
 4  C                  0.63653307       -3.72839245       -0.20920210
 5  C                 -0.63344021        3.68907733       -0.18936875
 6  C                  0.74721712        3.69290885       -0.24498747
 7  H                 -3.27970365       -1.60456490        0.05400333
 8  H                 -3.29366298       -3.38018180       -0.07227913
 9  H                  3.19673020       -3.56912494       -0.00022165
10  H                  3.29951867       -1.79214204        0.12940255
11  H                 -3.21441040        3.35678966       -0.21554255
12  H                 -3.13673120        1.60039363       -0.23074542
13  H                  3.34036924        1.67067246        0.05778821
14  H                  3.31338788        3.44782895       -0.10515166
15  C                 -1.44998212       -2.47255080       -0.08974916
16  C                  1.42173351       -2.53291226       -0.05565095
17  C                 -1.31643947        2.48752899        0.00024151
18  C                  1.49666933        2.49437939       -0.09051034
19  O                 -2.68364976        0.03015030        0.03103269
20  O                  2.75870821       -0.05544738        0.11301362
21  C                 -1.41270857       -0.01473668        0.04981515
22  C                  1.50361480       -0.04399812        0.06343197
23  C                 -0.70298242       -1.25934920        0.00017244
24  C                  0.74031359       -1.28606824        0.01518871
25  C                 -0.63784451        1.25504156        0.05463037
26  C                  0.77869887        1.24577015        0.02443651
27  N                 -2.79823125       -2.49707451       -0.06034928
28  N                  2.76491582       -2.65330179       -0.00395475
29  N                 -2.77761357        2.51206921        0.17264275
30  N                  2.84105283        2.55251225       -0.07967365
31  H                 -1.28934437       -4.63291509       -0.34046597
32  H                  1.16047747       -4.68285459       -0.31222346
```

```
33  H                        -1.17899392      4.63456361      -0.27233303
34  H                         1.28027110      4.63648444      -0.38297714
35  H                        -3.04944113      2.42483770       1.16464566
```

Listing B.12: Disperseblue1 dye optimized deprotonated geometry.xyz file generated with NWChem.

B.2   NWChem input files

B.2.1   Input files mPD

```
 1  echo
 2  start mPD
 3  title "mPD protonated geometry optimization"
 4  charge 1
 5  geometry
 6      load mPD-pro.xyz
 7  end
 8  basis
 9      * library def2-SVP
10  end
11  dft
12      xc b3lyp
13  end
14  DRIVER
15      XYZ
16      MAXITER 200
17  END
18  task dft optimize
```

Listing B.13: mPD Protonated Geometry Optimization in NWChem

```
 1  echo
 2  start mPD
 3  title "mPD TDDFT excited states"
 4  charge 1
 5  geometry
 6      load mPD-pro-opt.xyz
 7  end
 8  basis
 9      * library def2-SVP
10  end
11  dft
12      xc b3lyp
13      mult 2
14  end
15  tddft
16      nroots 5
17  end
18  task tddft energy
```

Listing B.14: mPD Protonated excited state calculation in NWChem

```
1     echo
2 start mPD
3 title "mPD deprotonated geometry optimization"
4 geometry
5     load mPD-geometry-de.xyz
6 end
7 basis
8     * library def2-SVP
9 end
10 dft
11     xc b3lyp
12 end
13 DRIVER
14     XYZ
15     MAXITER 200
16 END
17 task dft optimize
```

Listing B.15: mPD Protonated excited state calculation in NWChem

```
1     echo
2 start mPD
3 title "mPD TDDFT excited states"
4 geometry
5     load mPD-de-geo-opt.xyz
6 end
7 basis
8     * library def2-SVP
9 end
10 dft
11     xc b3lyp
12     grid nodisk
13     noprint "final vectors analysis"
14 end
15 tddft
16     nroots 5
17 end
18 task tddft energy
```

Listing B.16: mPD deprotonated excited state calculation in NWChem

B.2.2 Phloroglucinol

```
1     echo
2 start phloroglucinol
3 title "phloroglucinol protonated geometry optimization"
4 geometry
5     load phlor-pro.xyz
6 end
```

```
 7  basis
 8      * library def2-SVP
 9  end
10  dft
11      xc b3lyp
12      mult 2
13  end
14  DRIVER
15      XYZ
16      MAXITER 200
17  END
18  task dft optimize
```

Listing B.17: Phloroglucinol Protonated geometry optimization in NWChem

```
 1      echo
 2  start phloroglucinol
 3  title "phloroglucinol TDDFT excited states"
 4  charge 1
 5  geometry
 6      load phlor-pro-geo-opt.xyz
 7  end
 8  basis
 9      * library def2-SVP
10  end
11  dft
12      xc b3lyp
13  end
14  tddft
15      nroots 5
16  end
17  task tddft energy
```

Listing B.18: Phloroglucinol protonated tddft excited states in NWChem

```
 1      echo
 2  start phloroglucinol
 3  title "phloroglucinol protonated geometry optimization"
 4
 5  geometry
 6      load phlor-de-geo.xyz
 7  end
 8  basis
 9      * library def2-SVP
10  end
11  dft
12      xc b3lyp
13      mult 2
14  end
15  DRIVER
16      XYZ
17      MAXITER 200
18  END
19  task dft optimize
```

Listing B.19: Phloroglucinol deprotonated geometry optimization with DFT in NWChem

```
1     echo
2 start phloroglucinol
3 title "phloroglucinol TDDFT excited states"
4
5 charge -1
6 geometry
7     load phlor-de-geo-opt.xyz
8 end
9 basis
10     * library def2-SVP
11 end
12 dft
13     xc b3lyp
14 end
15 tddft
16     nroots 5
17 end
18 task tddft energy
```

Listing B.20: Phloroglucinol deprotonated tddft excited states in NWChem

B.2.3 Disperse-blue1

```
1     echo
2 start disperseblue1dye
3 title "disperseblue1dye protonated geometry optimization"
4
5 charge 1
6
7 geometry
8     load disperse-pro.xyz
9 end
10
11 basis
12     * library def2-SVP
13 end
14
15 dft
16     xc b3lyp
17     grid nodisk
18     noprint "final vectors analysis"
19 end
20
21
22 DRIVER
23     XYZ
24     MAXITER 200
25 END
```

```
26
27 task dft optimize
```

Listing B.21: Disperse Blue1 protonated geometry optimization with DFT in NWChem

```
1      echo
2  start disperseblue1dye
3  title "disperseblue1dye protonated geometry optimization"
4
5  charge 1
6
7  geometry
8      load disperse-pro.xyz
9  end
10
11 basis
12     * library def2-SVP
13 end
14
15 dft
16     xc b3lyp
17     grid nodisk
18     noprint "final vectors analysis"
19 end
20
21
22 DRIVER
23     XYZ
24     MAXITER 200
25 END
26
27 task dft optimize
```

Listing B.22: Disperse Blue1 protonated excited states with TDDFT in NWChem

```
1  echo
2  start disperseblue1dye
3  title "disperseblue1dye deprotonated geometry optimization"
4
5  geometry
6      symmetry c1
7      load "disperseBlue1.xyz"
8  end
9
10 basis
11     * library "def2-SVP"
12 end
13
14 dft
15     xc b3lyp
16     grid nodisk
17     noprint "final vectors analysis"
18 end
19
```

```
20 task dft optimize
```

Listing B.23: Disperse Blue1 deprotonated geometry optimization with DFT in NWChem

```
 1     echo
 2 start disperseblue1
 3 title "disperseblue1 deprotonated TDDFT excited states"
 4
 5 charge -1
 6
 7 geometry
 8     symmetry c1
 9     load disperse-de-geo-opt.xyz
10 end
11
12 basis
13     * library def2-SVP
14 end
15
16 dft
17     xc b3lyp
18 end
19
20 tddft
21     nroots 5
22 end
23
24 task tddft energy
```

Listing B.24: Disperse Blue1 deprotonated tddft excited states in NWChem

B.3   Python Code NWChem output sorting

The following code was generated to extract only necessary information from the NWChem output file data in order to calculate the fluorescence lifetime later on

```
 1     import numpy as np
 2 input_file_path = " "
 3
 4 input_file = input_file_path
 5 output_file = " "
 6
 7 INDEX_MULTIPLICITY = 2
 8 INDEX_ROOT_NUMBER = 1
 9
```

```python
# Open input and output files
with open(input_file, 'r') as f_input:
    # Process each line in the input file
    data = []
    root_line = ''
    entry = []
    for line in f_input:
        line = line.strip()

        if line.startswith('Root'):
            if entry:
                data.append(entry)
                entry = []
            # Exclude keywords in the root line
            words = line.split()
            multiplicity_name = words[INDEX_MULTIPLICITY]
            if multiplicity_name == 'singlet':
                multiplicity = 1
            elif multiplicity_name == 'triplet':
                multiplicity = 3
            else:
                multiplicity = 0
            entry = [int(words[INDEX_ROOT_NUMBER]), # root number
                     multiplicity,
                     #int(words[3].replace('a', '1').replace('b',
                        '2')),
                     float(words[4]),
                     float(words[6])]

        elif 'Transition Moments' in line:

            # Append the transition line to the entry, excluding
               the keywords
            if 'Spin forbidden' in line:
```

```python
42                      entry += [0, 0, 0, 0, 0, 0, 0, 0, 0]
43                  else:
44                      words = line.split()
45                      entry += [float(words[3]),
46                                float(words[5]),
47                                float(words[7])]
48
49
50      # Append the last entry to the data list
51      if entry:
52          data.append(entry)
53
54 header_list = ['Root',
55                'Multiplicity',
56                # 'Spin Orbital Symmetry'
57                'TDM in a.u.',
58                'TDM in eV',
59                'X',
60                'Y',
61                'Z',
62                'XX',
63                'XY',
64                'XZ',
65                'YY',
66                'YZ',
67                'ZZ'
68                ]
69 header = '\t'.join(header_list)
70
71 data_array = np.array(data)
72
73 np.savetxt(output_file, data_array, fmt='%.15g', delimiter='\t',
       header= header)
```

B.4   Python Code Fluorescence Lifetime Calculation with NWChem data output

Using the .txt file generated with the code above the fluorescence lifetime can be evaluated

```python
import scipy.constants as sc
import numpy as np
import ownlibs as ol
#import matplotlib.pyplot as plt


def calculate_function(omega, d):
    d_debeye = d * 1 #convert d to debeye


    lambda_value = 1 / ((sc.mu_0 * omega**3 * d_debeye ** 2) / (3
        * sc.pi * sc.speed_of_light * sc.hbar))
    result_seconds = 1 / lambda_value  # Convert from 1/s to
        seconds (s)
    result_seconds *= 2.418884326505e-17  # Convert atomic units
        of time to seconds
    return result_seconds

# Read input values from file
input_filename = "/Users/denisedilshener/Documents/MasterThesis/
    NWCHEM/aug-ccpVDZ basis set/phlor-de-final-pVDZ.txt"# input
    file path
output_filename = "/Users/denisedilshener/Documents/MasterThesis/
    NWCHEM/aug-ccpVDZ basis set/phlor-de-FL-pVDZ.txt"# Output file
     name

data = np.loadtxt(input_filename)
# store values in array for plot

```

```python
n_values = []
results = []

# calculate by inserting data from each line in a loop
with open(output_filename, "w") as output_file:
    total_sum = 0  # Initialize the sum

    for line in data:
        values = line
        n = values[0]
        omega = values[2] # transition frequency value in a.u.
        a = values[4] # X value transition moment
        b = values[5] # Y value transition moment
        c = values[6] # Z value from transition moment
        d = np.array([a, b, c])
        G_im = ol.Im_G_freespace(omega)
        result = ol.linienbreite(omega, d, G_im)
        output_file.write(f"Result={result}\n")

        total_sum += result  # Add the result to the total_sum


n_values.append(n)
results.append(result)
```

List of Figures

List of Tables

Bibliography

[1] S Tang et al. "Modeling the accumulation of CO2 during high density, re-circulating transport of adult Atlantic salmon, Salmo salar, from observations aboard a sea-going commercial live-haul vessel". In: *Aquaculture* 296.1-2 (2009), pp. 102–109.

[2] Peter J Thomas et al. "The use of novel optode sensor technologies for monitoring dissolved carbon dioxide and ammonia concentrations under live haul conditions". In: *Aquacultural Engineering* 77 (2017), pp. 89–96.

[3] Surajit Das and Neelam Mangwani. "Ocean acidification and marine microorganisms: responses and consequences". In: *Oceanologia* 57.4 (2015), pp. 349–361.

[4] Wiktoria K Szapoczka et al. "Fluorescence intensity and fluorescence lifetime measurements of various carbon dots as a function of pH". In: *Scientific Reports* 13.1 (2023), p. 10660.

[5] Alicja Wiora and Józef Wiora. "Over one-year long-term laboratory tests of pH electrodes in terms of industrial applications checking stabilities of their parameters and their influence on uncertainties of measurements". In: *Sensors* 18.12 (2018), p. 4102.

[6] Christoph Staudinger et al. "Fast and stable optical pH sensor materials for oceanographic applications". In: *Sensors and Actuators B: Chemical* 282 (2019), pp. 204–217.

[7] Christian Totland et al. "9-Acridinemethanamine and Acridine-9-Carboxaldehyde as Potential Fluorescence Lifetime pH Indicators". In: *Journal of Fluorescence* 30 (2020), pp. 901–906.

[8] Mikhail Y Berezin and Samuel Achilefu. "Fluorescence lifetime measurements and biological imaging". In: *Chemical reviews* 110.5 (2010), pp. 2641–2684.

[9] Christian Totland et al. "A broad-range fluorescence lifetime pH sensing material based on a single organic fluorophore". In: *Journal of Fluorescence* 29 (2019), pp. 1125–1131.

[10] Ya Su, Zhigang Xie, and Min Zheng. "Carbon dots with concentration-modulated fluorescence: Aggregation-induced multicolor emission". In: *Journal of colloid and interface science* 573 (2020), pp. 241–249.

[11] Namasivayam Dhenadhayalan, King-Chuen Lin, and Tawfik A Saleh. "Recent advances in functionalized carbon dots toward the design of efficient materials for sensing and catalysis applications". In: *Small* 16.1 (2020), p. 1905767.

[12] Maria Semeniuk et al. "Future perspectives and review on organic carbon dots in electronic applications". In: *ACS nano* 13.6 (2019), pp. 6224–6255.

[13] Junjun Liu, Rui Li, and Bai Yang. "Carbon dots: A new type of carbon-based nanomaterial with wide applications". In: *ACS Central Science* 6.12 (2020), pp. 2179–2195.

[14] Bin Bin Chen et al. "Fluorescent carbon dots functionalization". In: *Advances in colloid and interface science* 270 (2019), pp. 165–190.

[15] Samira Bagheri, Amin TermehYousefi, and Javad Mehrmashhadi. "Carbon dot-based fluorometric optical sensors: an overview". In: *Reviews in Inorganic Chemistry* 39.4 (2019), pp. 179–197.

[16] ZC Wong et al. "Modelling fluorescence lifetimes with TD-DFT: a case study with syn-bimanes". In: *RSC advances* 6.90 (2016), pp. 87237–87245.

[17] Julia Preiss et al. "Ab initio prediction of fluorescence lifetimes involving solvent environments by means of COSMO and vibrational broadening". In: *The Journal of Physical Chemistry A* 122.51 (2018), pp. 9813–9820.

[18] Rengel Cane E Sia et al. "Radiative lifetime of a BODIPY dye as calculated by TDDFT and EOM-CCSD methods: Solvent and vibronic effects". In: *Physical Chemistry Chemical Physics* 23.46 (2021), pp. 26324–26335.

[19] Johannes Fiedler et al. "Effective Polarizability Models". In: *The Journal of Physical Chemistry A* 121.51 (2017). PMID: 29185741, pp. 9742–9751. DOI: 10.1021/acs.jpca.7b10159. eprint: https://doi.org/10.1021/acs.jpca.7b10159. URL: https://doi.org/10.1021/acs.jpca.7b10159.

[20] Joseph R Lakowicz. *Principles of fluorescence spectroscopy*. Springer, 2006.

[21] Stefan Buhmann. *Dispersion Forces II: Many-Body Effects, Excited Atoms, Finite Temperature and Quantum Friction*. Vol. 248. Springer, 2013.

[22] Stefan Scheel and Stefan Yoshi Buhmann. "Macroscopic QED-concepts and applications". In: *arXiv preprint arXiv:0902.3586* (2009).

[23] S. Y. Buhmann. *Dispersion Forces I: Macroscopic quantum electrodynamics and ground-state Casimir, Casimir–Polder and van der Waals forces*. Heidelberg: Springer, 2012.

[24] David J Griffiths and Darrell F Schroeter. *Introduction to quantum mechanics*. Cambridge university press, 2018. Chap. Quantum Mechanics in Three Dimensions.

[25] Izrail Solomonovich Gradshteyn and Iosif Moiseevich Ryzhik. *Table of integrals, series, and products*. Academic press, 2014.

[26] Hermann Haken and Hans Christoph Wolf. *The physics of atoms and quanta: introduction to experiments and theory*. Springer Science & Business Media, 2006.

[27] Francesca Mocci et al. "Carbon nanodots from an in silico perspective". In: *Chemical Reviews* 122.16 (2022), pp. 13709–13799.

[28] Fanyong Yan et al. "The fluorescence mechanism of carbon dots, and methods for tuning their emission color: a review". In: *Microchimica Acta* 186 (2019), pp. 1–37.

[29] Shi Ying Lim, Wei Shen, and Zhiqiang Gao. "Carbon quantum dots and their applications". In: *Chemical Society Reviews* 44.1 (2015), pp. 362–381.

[30] Jingkun Yu et al. "Theoretical understanding of structure–property relationships in luminescence of carbon dots". In: *The Journal of Physical Chemistry Letters* 12.32 (2021), pp. 7671–7687.

[31] Panagiotis Koutsogiannis et al. "Advances in fluorescent carbon dots for biomedical applications". In: *Advances in Physics: X* 5.1 (2020), p. 1758592.

[32] Nikita V Tepliakov et al. "sp2–sp3-Hybridized atomic domains determine optical features of carbon dots". In: *ACS nano* 13.9 (2019), pp. 10737–10744.

[33] Gauri Nigudkar. *63. COVALENT BONDING(9)- SP2 HYBRIDIZATION.* URL: `https://madoverchemistry.com/2018/09/10/63-nature-of-chemical-bonding-10-covalent-bonding9-hybridization4/`. (accessed: 11.10.2023).

[34] Evgeny V Kundelev et al. "Amino functionalization of carbon dots leads to red emission enhancement". In: *The Journal of Physical Chemistry Letters* 10.17 (2019), pp. 5111–5116.

[35] Meng Shao et al. "Continuous synthesis of carbon dots with full spectrum fluorescence and the mechanism of their multiple color emission". In: *Lab on a Chip* 19.23 (2019), pp. 3974–3978.

[36] Katerina Hola et al. "Photoluminescence effects of graphitic core size and surface functional groups in carbon dots: COO- induced red-shift emission". In: *Carbon* 70 (2014), pp. 279–286.

[37] Qi Wang et al. "Pressure-triggered aggregation-induced emission enhancement in red emissive amorphous carbon dots". In: *Nanoscale Horizons* 4.5 (2019), pp. 1227–1231.

[38] Siyu Lu et al. "Piezochromic carbon dots with two-photon fluorescence". In: *Angewandte Chemie* 129.22 (2017), pp. 6283–6287.

[39] Patrik R Callis. "Two-photon–induced fluorescence". In: *Annual Review of Physical Chemistry* 48.1 (1997), pp. 271–297.

[40] Charles E.Mortimer & Ulrich Müller. *Chemie, Das Basiswissen der Chemie*. Georg Thieme Verlag, 2003. Chap. 18. ISBN: 3-13-484308-0.

[41] Hamide Ehtesabi et al. "Carbon dots with pH-responsive fluorescence: a review on synthesis and cell biological applications". In: *Microchimica Acta* 187 (2020), pp. 1–18.

[42] Yaoping Hu et al. "Waste frying oil as a precursor for one-step synthesis of sulfur-doped carbon dots with pH-sensitive photoluminescence". In: *Carbon* 77 (2014), pp. 775–782.

[43] Johannes Fiedler et al. "Impact of effective polarisability models on the near-field interaction of dissolved greenhouse gases at ice and air interfaces". In: *Physical Chemistry Chemical Physics* 21.38 (2019), pp. 21296–21304.

[44] Maylis Orio, Dimitrios A Pantazis, and Frank Neese. "Density functional theory". In: *Photosynthesis research* 102 (2009), pp. 443–453.

[45] Kieron Burke and Friends. *The ABC of DFT*. Irvine, CA 92697: Department of Chemistry, University of California, Apr. 2007.

[46] Johannes Fiedler et al. "Perspectives on weak interactions in complex materials at different length scales". In: *Physical Chemistry Chemical Physics* (2023).

[47] Richard M. Martin. *Electronic Structure: Basic Theory and Practical Methods*. Cambridge University Press, 2004. DOI: 10.1017/CBO9780511805769.

[48] John P Perdew, Matthias Ernzerhof, and Kieron Burke. "Rationale for mixing exact exchange with density functional approximations". In: *The Journal of chemical physics* 105.22 (1996), pp. 9982–9985.

[49] Axel D Beck. "Density-functional thermochemistry. III. The role of exact exchange". In: *J. Chem. Phys* 98.7 (1993), pp. 5648–6.

[50] Narbe Mardirossian and Martin Head-Gordon. "Thirty years of density functional theory in computational chemistry: an overview and extensive assessment of 200 density functionals". In: *Molecular physics* 115.19 (2017), pp. 2315–2372.

[51] Julian Tirado-Rives and William L Jorgensen. "Performance of B3LYP density functional methods for a large set of organic molecules". In: *Journal of chemical theory and computation* 4.2 (2008), pp. 297–306.

[52] Denis Jacquemin et al. "Extensive TD-DFT benchmark: singlet-excited states of organic molecules". In: *Journal of Chemical Theory and Computation* 5.9 (2009), pp. 2420–2435.

[53] Jingjing Zheng, Xuefei Xu, and Donald G Truhlar. "Minimally augmented Karlsruhe basis sets". In: *Theoretical Chemistry Accounts* 128 (2011), pp. 295–305.

[54] E. Aprá et al. "NWChem: Past, present, and future". In: *The Journal of Chemical Physics* 152.18 (2020), p. 184102. DOI: 10.1063/5.0004997.

[55]   Marcus D Hanwell et al. "Avogadro: an advanced semantic chemical editor, visualization, and analysis platform". In: *Journal of cheminformatics* 4 (2012), pp. 1–17.

[56]   Andreas Klamt. "The COSMO and COSMO-RS solvation models". In: *Wiley Interdisciplinary Reviews: Computational Molecular Science* 8.1 (2018), e1338.

[57]   Douglas Dalzell Perrin. *Dissociation Constants of Organic Bases in Aqueous Solution: Hauptbd*. Butterworths, 1965.

[58]   R Manoharan and Sneh Kumar Dogra. "Spectral characteristics of phenylenediamines and their various protonated species". In: *Bulletin of the Chemical Society of Japan* 60.12 (1987), pp. 4409–4415.

[59]   Martin Lohrie and Wilhelm Knoche. "Dissociation and keto-enol tautomerism of phloroglucinol and its anions in aqueous solution". In: *Journal of the American Chemical Society* 115.3 (1993), pp. 919–924.

[60]   Dimitrios V Stergiou et al. "Study of the Electrochemical Behavior of Disperse Blue 1-Modified Graphite Electrodes. Application to the Flow Determination of NADH". In: *Electroanalysis: An International Journal Devoted to Fundamental and Practical Aspects of Electroanalysis* 16.11 (2004), pp. 949–954.

[61]   Drew F. Parsons Denise Dilshener Johannes Fiedler. "pH-sensitive spontaneous decay of functionalised carbon dots in solutions". Manuscript submitted for publication to the Journal of Chemical Physics: Festschrift in Honor of Louis E. Brus. 2024. URL: https://publishing.aip.org/publications/journals/special-topics/jcp/festschrift-in-honor-of-louis-e-brus/?Track=&utm_source=AIP%20Publishing&utm_medium=email&utm_campaign=14060090_JCP_Festschrift%20in%20honor%20of%20Louis%20E.%20Brus_CFP_Aug_2023&dm_i=1XPS,8DCU2,7T25EV,YIB2D,1.

Acknowledgements

I want to start by thanking everyone who helped me on my journey to finishing my master's.

First, I need to thank Bodil Holst for suggesting this project and giving me the chance to work on something so special. She motivated me to write my thesis in the area of theoretical physics, and I'm so grateful for that.

Next, I want to thank Johannes Fiedler for always finding time to motivate me, to show me the right way—not just with the master's thesis but also when we were lost at night in Sardinia—and for never getting tired of my endless questions. Thank you for always trying to get the best out of me and keeping me motivated. Your support, whether it was sharing a beer while we worked on calculations or setting up breakfast with a company's CTO to help me find job opportunities, has meant so much to me.

I also want to thank Drew Parsons, who welcomed me with open arms at the University of Cagliari in Sardinia and patiently introduced me to the secrets of quantum chemical calculations. Thanks for all your support and time.

Thank you to SFI Smart Ocean for the financial support and the great opportunity to work on this project. Also, a big thanks to Wiktoria, who always made time to explain her data to me.

I'm also really thankful for my study hall gang. You guys made every day better and kept me going when things were tough. A special shout out to Louis for making me smile everyday, Anne-line for the incredible mental support and coaching, and Glenn,

Markus, and Ilya for always being there to chat.

A huge thanks to Alexander, the best boyfriend in the world, for always being by my side, supporting me, and dealing with my moods. Thank you for all the love and for helping me recharge and face each day with new energy. Even though the time was rough and stressful for yourself, I appreciate you always having my back and I loved our little evening ritual together to calm down to start the next day energized and fresh.

I also want to thank my incredible work team, especially Natalie, for letting me leave early and covering my shifts so I could focus on writing my thesis. Your support has been incredible.

Lastly, I'm so grateful to my family for all their support from afar, especially my dad who took the time to read through my whole thesis and helped me make it better.

Thank you all so much for everything. I could not have done this without you.